

PULSED LASER ANNEALING AND RAPID THERMAL ANNEALING OF  
COPPER-INDIUM-GALLIUM-DISELENIDE-BASED THIN-FILM SOLAR CELLS

By

XUEGE WANG

A DISSERTATION PRESENTED TO THE GRADUATE SCHOOL  
OF THE UNIVERSITY OF FLORIDA IN PARTIAL FULFILLMENT  
OF THE REQUIREMENTS FOR THE DEGREE OF  
DOCTOR OF PHILOSOPHY

UNIVERSITY OF FLORIDA

2005

Copyright 2005

By

Xuege Wang

To my parents and my friends

## ACKNOWLEDGMENTS

I would like to express my sincere gratitude to my supervisory committee chair (Professor Sheng S. Li), for his support and encouragement in the past 5 years. Without his patience and guidance, none of this work would have been possible. I would also like to thank Professors Timothy J. Anderson, Oscar D. Crisalle and Gijs Bosman for serving on my supervisory committee.

I extend special thanks to Dr. James C. Keane for his help on device fabrication; Dr. Leon Chen, for supplying of CIGS samples; Professor Omar Manasreh, for his help on thermal annealing; Dr. Valentin Craciun, for his help on laser annealing; Dr. Chia-Hua Huang, for training me on device performance tests; and Dr. Lei Li Kerr, for her valuable discussions.

I would like to extend my sincere appreciation to my colleagues (Jiyon Song, Woo Kyoung Kim, Seokhyun Yoon and Wei Liu), in the laboratories for their assistance. I could not have accomplished this work without their cooperation and help.

Finally I am greatly indebted to my parents in China for their constant love, support, and encouragement. I dedicate this dissertation to them.

## TABLE OF CONTENTS

	<u>page</u>
ACKNOWLEDGMENTS .....	iv
LIST OF TABLES .....	viii
LIST OF FIGURES .....	x
ABSTRACT .....	xv
CHAPTER	
1 INTRODUCTION .....	1
2 LITERATURE REVIEW OF THIN-FILM SOLAR CELLS .....	7
Current Status of Photovoltaic Technologies .....	7
Thin-Film Solar Cells .....	8
Amorphous Silicon (a-Si:H) Thin-Film Solar Cells .....	8
The CdTe Thin-Film Solar Cells .....	9
The Cu(In,Ga)Se <sub>2</sub> (CIGS) Thin-Film Solar Cells .....	9
3 PULSED LASER ANNEALING (PLA) OF FILM PROPERTIES AND DEVICE PERFORMANCE FOR CIGS SOLAR CELLS .....	18
Introduction .....	18
Experimental Details .....	19
Results of PLA Treated CIGS Films .....	20
Results of First Set of PLA Treated CIGS Solar Cells .....	21
Photo- J-V Measurements of PLA CIGS Cells .....	21
The Q-E Measurement of PLA CIGS Cells .....	22
Results of Second Set of PLA Treated CIGS Solar Cells .....	23
Photo- J-V Results .....	23
Dark- J-V Results .....	23
Quantum Efficiency Results .....	25
The C-V and DLTS Characterizations .....	25
Additional PLA Effect Study .....	26
Summary .....	27
4 RAPID THERMAL ANNEALING (RTA) OF FILM PROPERTIES AND DEVICE PERFORMANCE FOR CIGS- BASED SOLAR CELLS .....	48

Progressive RTA Treatment on CIGS Solar Cells .....	48
The RTA Effects of Separated CIGS Films .....	49
The XRD and SEM Results.....	49
Hall-Effect Measurements.....	50
The RTA Effects of Separated CIGS Solar Cell Devices.....	50
Experimental Details .....	50
Photo- J-V Performance .....	51
Dark- J-V Characteristics .....	51
The S-R and Q-E Performance.....	52
Thermal Annealing on CIGS Solar Cells by High Temperature XRD System ..	53
Summary.....	53
5 FABRICATION PROCESS OF CIGS SOLAR CELLS.....	78
Substrate .....	78
Back Contact Layer .....	80
CIGS Absorber Layer.....	80
Chemical Bath Deposition (CBD) of CdS Buffer Layer.....	82
Alternative Cd- Free Buffer Layer .....	86
Transparent Conducting Oxide (TCO) Layer.....	87
Metal Contact.....	90
6 CHARACTERIZATION AND MEASUREMENT SYSTEMS FOR CIGS SOLAR CELLS .....	96
Hall-Effect Measurements .....	96
Introduction .....	96
Measurement Procedure and Apparatus.....	97
Related Studies, Results and Discussion.....	98
The Cd-partial-electrolyte treatment on CIGS films.....	98
Hall-effect data of CIGS films supplied by NREL TFPPP team .....	99
Photo- and Dark- J-V Measurements .....	100
Solar Cell Parameters .....	100
Photo- J-V Measurement System.....	103
Light source.....	104
Temperature control .....	104
Contacts and connections .....	105
Dark- J-V Measurement .....	106
Quantum Efficiency Measurement .....	107
Quantum Efficiency Measurement Instrumentation .....	107
Monochomator and Monochromatic Light Source .....	108
Monochromatic Light Chopper .....	109
Bias Light Source .....	110
Spectral Detector and Synchronous Detection Instrumentation.....	110
Spectral Response Measurement Procedures .....	111
Deep Level Transient Spectroscopy (DLTS) Measurement.....	112

	Features and Principles.....	112
	Related Results and Discussions .....	115
7	DEVICE MODELING AND SIMULATION OF CIGS SOLAR CELLS .....	128
	Simulation Model of CIGS Solar Cell Devices.....	128
	Simulation Results of CIGS Solar Cells.....	130
	Conclusions.....	132
8	RADIATION EFFECTS ON CIGS FILM AND SOLAR CELLS.....	140
	Introduction.....	140
	ELDRS Effects .....	141
	Total Dose Effects .....	141
	Displacement Damage.....	142
	High-K Dielectrics.....	146
	Experimental Details and Discussion .....	146
9	SUMMARY AND FUTURE WORK.....	161
	Summary.....	161
	Future Work.....	163
	LIST OF REFERENCES.....	164
	BIOGRAPHICAL SKETCH .....	169

## LIST OF TABLES

<u>Table</u>	<u>page</u>
3-1. Effective minority carrier lifetime ( $\tau$ ) of CIGS films before and after PLA treatment as measured by DBOM .....	29
3-2. Hall-effect results for CIGS films before and after PLA treatments.....	30
3-3. Effective lifetimes and photo- J-V results of PLA CIGS/CdS samples and devices.....	31
3-4. Photo-J-V performance of control cell and PLA-treated CIGS solar cells.....	32
3-5. Photo- J-V performance and dark- J-V parameters for the control cell and selected PLA-treated CIGS cells.....	33
3-6. Results of the DLTS measurements on the control cell and PLA treated CIGS solar cells.....	34
3-7. Annealing condition of new PLA samples.....	35
4-1. Photo- J-V results of CIGS solar cells before and after progressive RTA.....	54
4-2. CIGS film number and the annealing conditions .....	55
4-3. Hall-effect data of NREL CIGS samples before and after RTA treatments .....	56
4-4. Annealing conditions of RTA treated CIGS devices .....	57
4-5. Photo- J-V results of separated CIGS solar cells before and after RTA .....	58
4-6. Photo- J-V results of CIGS solar cells before and after RTA by using high temperature XRD system .....	59
5-1. Conversion efficiencies of CIGS cells grown by non-vacuum processes (by ISET) on different substrates.....	91
6-1. Hall-effect results for the different Cd-partial-electrolyte treatment times on the CIGS samples.....	116
6-2. Results from Hall-effect measurements for the CIGS samples.....	117

6-3. Hall measurement results for the CIS/CGS samples deposited on different substrates (GaAs/glass) by PMEE method.....	118
6-4. Photo- J-V results for EPV CIGS device before and after DLTS scan.....	119
7-1. Performance parameters of the CIGS ( $E_g=1.2$ eV) solar cells versus the defect density in the CIGS absorber layer. ....	133
7-2. Photo- J-V data of cell#1 before and after progressive RTA treatment (From experiment and AMPS 1D simulation results).....	134
8-1. Dose rate and total dose of the tested CIGS samples and devices .....	150
8-2. Dose conditions and Photo- J-V results of CIGS devices before and after radiation.....	151

## LIST OF FIGURES

<u>Figure</u>	<u>page</u>
2-1. Best performance of various thin-film solar cells. ....	11
2-2. Sketch of the layer structure for (a) a-Si p-i-n (superstrate), and (b) a-Si n-i-p (substrate) solar cells. ....	12
2-3. Schematic sketch of band diagram for a-Si p-i-n solar cell. ....	13
2-4. Device structure of CdS/CdTe thin-film solar cell. ....	14
2-5. Band gap versus lattice constant diagram of CIGS solar cell. ....	14
2-6. Absorption coefficients of different solar cell materials. ....	15
2-7. Photo- J-V result of 19.2% CIGS solar cell from NREL (under 1000W/m <sup>2</sup> , AM 1.5 global spectrum at 25°C). ....	16
2-8. Device structure of a CdS/CIGS-based solar cell. ....	17
3-1. XRD spectra before and after PLA treatments for (a) a CIGS and (b) a CdS /CIGS sample. ....	36
3-2. Surface morphology of CIGS films (a) without and (b) with PLA treatments at an energy density of 55 mJ/cm <sup>2</sup> (SEM images with magnification of 6000x). ....	37
3-3. Quantum efficiency of CIGS cells with and without PLA treatment. ....	38
3-4. Spectral response of CIGS cells with and without PLA treatment. ....	38
3-5. Photo- J-V parameters versus different PLA condition. ....	39
3-6. Dark- J-V curves comparing the control cell to two PLA treated cells. ....	40
3-7. Dark- J-V curves (semi-log plot) of the control cell and two PLA treated cells. ....	41
3-8. Quantum efficiency (Q-E) versus wavelength comparing the control cell to the two PLA-treated cells. ....	42
3-9. The DLTS scans of the control- and PLA- CIGS cell. ....	43

3-10. Surface morphology of CdS/CIGS films (a) before and after PLA treatment with energy densities at (b) 30 mJ/cm <sup>2</sup> , (c) 50 mJ/cm <sup>2</sup> , (d) 70 mJ/cm <sup>2</sup> , (e) 90 mJ/cm <sup>2</sup> , (f) 110 mJ/cm <sup>2</sup> . (SEM images with magnification of 4000x).....	44
3-11. Surface morphology of CdS/CIGS films (a) before and after PLA treatment with energy densities at (b) 30 mJ/cm <sup>2</sup> , (c) 50 mJ/cm <sup>2</sup> , (d) 70 mJ/cm <sup>2</sup> , (e) 90 mJ/cm <sup>2</sup> , (f) 110 mJ/cm <sup>2</sup> . (SEM images with magnification of 40000x).....	44
3-12. Theta-2 theta (symmetrical geometry) diffraction patterns of PLA samples and control sample. ....	45
3-13. Grazing incidence XRD analysis (GIXD) of PLA samples and the control sample (omega=3deg.) .....	46
3-14. Grazing incidence XRD analysis (GIXD) of PLA samples and the control sample (omega=1deg.) .....	47
4-1. Cycle time for Rapid Thermal Annealing (one run). ....	60
4-2. XRD results of RTA treated CIGS films and the control sample. ....	61
4-3. Surface morphology of RTA treated CIGS films and the control sample. (SEM images with magnification of 3000x).....	62
4-4. Surface morphology of RTA treated CIGS films and the control sample. (SEM images with magnification of 10000x).....	63
4-5. Surface morphology of RTA treated CIGS films and the control sample. (SEM images with magnification of 30000x).....	64
4-6. Dark- J-V curves of tested CIGS solar cell (#D-R1) before and after RTA (300°C, 1-min) treatment.....	65
4-7. Dark- J-V curves of tested CIGS solar cell (#D-R2) before and after RTA (300°C, 2-min) treatment.....	66
4-8. Dark- J-V curves of tested CIGS solar cell (#D-R3) before and after RTA (350°C, 1-min) treatment.....	67
4-9. Dark- J-V curves of tested CIGS solar cell (#D-R4) before and after RTA (350°C, 2-min) treatment.....	68
4-10. Dark- J-V curves (semi-log plot) of tested CIGS solar cell (#D-R1) before and after RTA (300°C, 1-min) treatment. ....	69
4-11. Dark- J-V curves (semi-log plot) of tested CIGS solar cell (#D-R2) before and after RTA (300°C, 2-min) treatment. ....	70
4-12. Dark- J-V curves (semi-log plot) of tested CIGS solar cell (#D-R3) before and	

after RTA (350°C, 1-min) treatment. ....	71
4-13. Dark- J-V curves (semi-log plot) of tested CIGS solar cell (#D-R4) before and after RTA (350°C, 2-min) treatment. ....	72
4-14. Quantum efficiency (Q-E) versus wavelength of tested CIGS solar cell (#D-R1) before and after RTA (300°C, 1-min). ....	73
4-15. Quantum efficiency (Q-E) versus wavelength of tested CIGS solar cell (#D-R2) before and after RTA (300°C, 2-min). ....	74
4-16. Quantum efficiency (Q-E) versus wavelength of tested CIGS solar cell (#D-R3) before and after RTA (350°C, 1-min). ....	75
4-17. Quantum efficiency (Q-E) versus wavelength of tested CIGS solar cell (#D-R4) before and after RTA (350°C, 2-min). ....	76
4-18. Photo- J-V curves of tested CIGS solar cells before and after (a) 100°C, 30 seconds and (b) 150°C, 30 seconds RTA treatments by using high temperature XRD system. ....	77
5-1. Layer structure of CIS/CIGS based solar cells.....	92
5-2. Schematic profile of the NREL ‘three-stage physical evaporation process for the fabrication of CIGS solar cells’.....	93
5-3. Simple CBD experimental set-up.....	94
5-4. The E-Beam evaporation technique for depositing metal contact films on solar cells.....	95
6-1. Schematic representation of the Hall effect sample. ....	120
6-2. Typical four-point van der Pauw and Hall effect measurements. ....	120
6-3. The equivalent circuit diagram of a CIGS PN junction solar cell.....	121
6-4. The I-V characteristics under dark and illumination conditions of a PN junction solar cell. ....	121
6-5. Apparatus and block diagram of I-V measurement system for the CIS-based cells.....	122
6-6. The photo- J-V measurement and analysis for solar cells using the <i>LabVIEW</i> program. (The tested CIGS solar cell is fabricated by EPV.) ....	122
6-7. The dark-J-V measurement and analysis for solar cells using the <i>LabVIEW</i> program. (The tested CIGS solar cell is fabricated by NREL.) ....	123

6-8.	The block diagram of a spectral response measurement system for the CIS-based solar cells.....	124
6-9.	The spectral response and quantum efficiency measurements for solar cells using <i>LabVIEW</i> program. (The tested CIGS solar cell is fabricated by UF.) .....	124
6-10.	The DLTS scans for (a) EPV device at $V_R = -0.1V$ , $V_H = 0.3V$ , and $W = 10ms$ . And (b) An Arrhenius plot obtained from the DLTS scans shown in (a). .....	125
6-11.	The DLTS scans for (a) EPV device at $V_R = 0.5V$ , $V_H = 0.7V$ , and $W = 10ms$ . And (b) An Arrhenius plot obtained from the DLTS scans shown in (a). .....	126
6-12.	Dark- J-V curves of tested EPV CIGS device before and after DLTS measurement.....	127
6-13.	Photo- J-V curves of tested EPV CIGS device before and after DLTS measurements. ....	127
7-1.	The schematic energy band diagram of a typical ZnO/CdS/CIGS solar cell under equilibrium condition. ....	135
7-2.	Performance parameters of CIGS ( $E_g = 1.2eV$ ) solar cells versus the defect density of CIGS absorber layer. ....	136
7-3.	Photo- J-V curves of cell#1 before and after progressive RTA treatment (From AMPS 1D simulation results). ....	137
7-4.	Dark- J-V curves of cell#1 before and after progressive RTA treatment (From AMPS 1D simulation results). ....	138
7-5.	Quantum efficiency of cell#1 before and after progressive RTA treatment (From AMPS 1D simulation results). ....	139
8-1.	Five basic effects of a defect energy level ( $E_t$ ) on the electrical performance of a device. ....	152
8-2.	Gamma absorption cross-section versus photon energy. ....	153
8-3.	Photon interaction probabilities versus photon energy. ....	154
8-4.	Photograph of irradiated CIGS films and the control film.....	155
8-5.	The XRD results of irradiated CIGS samples (#1-4) and the control sample (#5).156	
8-6.	Photo- J-V results of CIGS device #1 (cell#1) before and after total dose of 2.12 Mrads (Si) radiation (Device from GSE). ....	157
8-7.	Photo- J-V results of CIGS device #1 (cell#2) before and after total dose of 2.12 Mrads (Si) radiation (Device from GSE). ....	158

8-8. Photo- J-V results of CIGS device #2 (cell#1) before and after total dose of 6.5 Mrads (Si) radiation (Device from SSI).....	159
8-9. Photo- J-V results of CIGS device #2 (cell#2) before and after total dose of 6.5 Mrads (Si) radiation (Device from SSI).....	160

Abstract of Dissertation Presented to the Graduate School  
of the University of Florida in Partial Fulfillment of the  
Requirements for the Degree of Doctor of Philosophy

PULSED LASER ANNEALING AND RAPID THERMAL ANNEALING OF  
COPPER-INDIUM-GALLIUM-DISELENIDE-BASED THIN-FILM SOLAR CELLS

By

Xuege Wang

August 2005

Chair: Sheng S. Li

Major Department: Electrical and Computer Engineering

Effects of Pulsed Laser Annealing (PLA) treatment on the film properties and the performance of CIGS solar cells have been studied under various annealing conditions. This technique has been used for the first time to modify near-surface defects and related junction properties in Cu(In,Ga)Se<sub>2</sub> (CIGS) solar cells.

CIGS films deposited on Mo/glass substrates were annealed using a 25 ns pulsed laser beam (248 nm wavelength) and a 250 ns pulsed laser beam (308 nm wavelength) with a larger beam size at selected laser energy densities in the range of 20 to 110 mJ/cm<sup>2</sup> and pulse number in the range of 5 to 20 pulses. The narrowing of X-Ray Diffraction (XRD) peak, new shoulders of Grazing Incidence X-ray Diffraction (GIXD) and the increase of Scanning Electron Microscopy (SEM) surface feature size suggest near surface structure changes. The Dual-Beam Optical Modulation (DBOM) and Hall- effect measurements indicate PLA treatment increases the effective carrier lifetime and mobility as well as the sheet resistance. In addition, several annealed CdS/CIGS films processed

by PLA were fabricated into solar cells and characterized by Photo- and Dark- J-V and Quantum Efficiency (Q-E) measurements. Significant improvement was observed in the overall cell performance, diode quality, and spectral response when compared to pre-annealed cells. Deep- Level Transient Spectroscopy (DLTS) results showed a 50% reduction of the density of shallow defect trap after low-power PLA treatments. The energy density of the laser beam and the pulse number were found to play key roles in modifying the optical and electrical properties of the CIGS films and hence the cell performance. Results suggest that the optimal PLA energy density and pulse number are around  $30 \text{ mJ/cm}^2$  and 5 pulses, respectively.

A comprehensive study of the effects of Rapid Thermal Annealing (RTA) on the film properties and the performance of CIGS solar cells has been carried out in this dissertation. CIGS samples and devices were characterized by using XRD, GIXD, SEM, Hall effect, Photo- and Dark- J-V and Q-E measurements before and after RTA treatment under various ramp up and down rates, peak temperatures, holding times, and ambient conditions. Results show that progressive RTA treatments could significantly improve the overall uniformity and performance of large-area CIGS solar cells. Under low RTA temperatures, the surface composition and morphology remain unchanged. The simple RTA treatment on CIGS cells shows an increase of quantum efficiency and some improvement of cell performance. The estimated optimal annealing temperature should be between  $200$  and  $300^\circ\text{C}$  with a holding time of 1- minute or less.

Device simulation using one-dimensional (1-D) AMPS program has also been carried in this work for a typical CIGS cell with different defect densities. A well fitting between simulation results and progressive RTA results has been obtained. The results

show that the device performance and spectral response can be positively improved by reducing the defect density of CIGS absorber layer.

In addition, Gamma-Ray radiation tolerance study on several CIGS samples and solar cells were performed under different total dose by varying the sample displacements and exposure times. XRD and Photo- J-V measurements were taken before and after each radiation. The results show that the surface morphology, crystallinity and the device performance of CIGS solar cells change under certain radiation dose condition.

## CHAPTER 1 INTRODUCTION

Solar cells are now the most important and viable power source for satellites and space vehicles. Solar cells have also been used successfully in large-scale terrestrial power generation applications. With world energy consumption growing each year, most of the energy comes from petroleum, natural gas, and fossil fuel, and nuclear power generation. These power systems are polluting, costly, or will be exhausted in the near future. Therefore, a renewable energy source such as solar energy is needed to replace these systems and protecting our natural environment and future use. The sun has been radiating energy for over 500 million years, and is expecting to continue indefinitely. Photovoltaic (solar) energy conversion becomes an excellent candidate because it is clean, inexhaustible, uninterrupted, and nonpolluting. Solar cells use the internal photovoltaic (PV) effect in semiconductors, and are capable of providing electricity directly from the sun for a wide variety of applications with the advantage of long-duration power generation at lower maintenance cost.

Recent interest has increased in research and development of low-cost, flat-panel solar cells, thin-film PV devices, concentrator systems, and many innovative concepts. In 2004, worldwide PV module production has generated 750 MW electric power for terrestrial applications. The PV technology is growing at more than 20% annual growth rate, and is expecting to produce 5 to 10% of electricity used in United States in 10 to 20 years.

As a simple definition, the basic function of a solar cell module is to absorb incident sun light and to create electron-hole pairs and collected at the external contacts of solar cells to produce electricity for a wide variety of applications. A semiconductor p-n junction structure is commonly used in solar cells. The useful spectral range to convert the incident sun light into electricity is usually determined by the bandgap ( $E_g$ ) of the semiconductor. Separation and transport of the photo-generated electron – hole pairs are accomplished by the built-in electric field formed in the depletion region of the p-n junction. A transparent conductive oxide (TCO) or ohmic contact grid is normally used for current collection in the front, and a metal contact is used in the back side of the solar cell.

Since the first silicon solar cell was reported by Chapin, Fuller, and Pearson in 1954, the solar cell has evolved from being a low-efficiency device to being a major power generation source for the spacecraft and many terrestrial power generation systems. Currently, high efficiency single- and multi-junction solar cells based on III-V compound semiconductors such as GaAs- and InP- materials have been developed for space applications, while crystalline silicon solar cells are still the dominant PV technology for terrestrial power generation applications. Commercial silicon solar cells available today are made from solar-grade single crystalline silicon or polycrystalline silicon materials. Although high efficiencies are achieved with single crystalline silicon, the silicon technology is not expected to become a low-cost PV technology. One reason is that silicon is an indirect band gap semiconductor which requires a thick absorber layer (about 250-400  $\mu\text{m}$  thick) to absorb 90% of the useful sun light for electricity generation.

In the past few years, much effort has been devoted to developing various low-cost, high-efficiency, and high-stability solar cells for both terrestrial and space power generation and for applications in consumer electronics. Efficient solar cells can be made by thin-film technology. By using semiconductor material with high absorption, a film thickness of a few micrometers is sufficient to effectively collect the sun light. A wide variety of absorber materials is available for solar cell applications.

Today, the most common thin-film solar cells are made from amorphous silicon materials. The commercial deposition process of a-Si:H using plasma-enhanced chemical vapor deposition (PECVD) technique is compatible with large-area deposition and low temperature processing. This allows the use of a wide variety of inexpensive substrate materials. The a-Si:H films can be easily doped by adding phosphorus or boron containing gases during deposition process for n- and p-type doping. The optical band gap of a-Si is typically around  $E_g \approx 1.7\text{eV}$  and can be tuned. For example, the band gap energy of a-Si:H can be increased by alloying with carbon or oxygen, and decreased with incorporation of germanium to form  $\text{a-Si}_x\text{Ge}_{1-x}$  ( $0 \leq x \leq 1$ ) films. The energy band gap can also be fine tuned by changing the hydrogen content using different deposition parameters and methods. The a-Si:H thin film solar cells have reached an efficiency of 13.1%, while long term stability is a key issue for a-Si:H solar cells. Other thin film PV technologies based on CdTe (with a maximum efficiency of 16.5% [1]), and CdS/CuIn(Ga)Se<sub>2</sub> (CIGS) material systems have shown great promising for large scale terrestrial power systems. CIGS thin film solar cells with efficiency exceeding 19% AM1.5G have been demonstrated recently by NREL research team. Thin-film PV technology benefits from low material consumption and low price as compared to

crystalline silicon solar cells. Scaling the PV technology from single solar cells to large-area PV modules is straightforward since many cells can be interconnected from material deposited on one substrate in the form of stacked film layers. Compared to the crystalline material, thin-film solar cells can be manufactured with less energy input. This shortens the energy payback time (the time needed for photo-generated energy output to equal the energy consumed to produce the device).

Specific advantages of the  $\text{CuIn(Ga)Se}_2$  alloy are its wide compositional tolerance and a direct band gap material high optical absorption in the visible spectrum. One major drawback for large scale production is the limited extraction rate of indium from mining. Cost and conversion efficiency are the two key factors that determine the compatibility of a solar cell. Thin-film solar cells give the best hope for obtaining PV devices with high efficiency and low cost. Copper indium diselenide ( $\text{CuInSe}_2$  or CIS) and copper indium gallium diselenide ( $\text{CuInGaSe}_2$  or CIGS) films are the most promising materials of all thin-film solar cells for achieving these goals. Such material has certain exceptional characteristics particularly suitable for photovoltaic heterojunction applications. CIGS is a direct band gap material, which minimizes absorber layer thickness (1-2  $\mu\text{m}$ ). Thin-films of CIS/CIGS are p-type conductivity, and a surface inversion layer can be formed when deposited with a CdS buffer layer. Therefore, an n-p heterojunction structure can be formed solar cell application. CIGS material with 30% of gallium content has a band-gap energy of around 1.3 eV at 300 K, which is nearly ideal for a photovoltaic device operating in the solar spectrum. There is no reported photon degradation of CIGS solar cells because of good thermal stability. It can absorb the solar spectrum within a few micrometers (1-2  $\mu\text{m}$ ) with high optical absorption coefficient.

The CIGS thin-film solar cells have recently achieved efficiencies in excess of 19.5% AM1.5G. However, further optimization of the device performance could be substantially accelerated by a better understanding of the processing effects on the interface between the CdS and CIGS layers and the transport properties of CIGS films.

The pulsed laser annealing (PLA) and halogen lamp based rapid thermal annealing (RTA) on silicon-based devices and solar cells have been extensively investigated in recent years [2-9]. Today, PLA technique is widely used to activate boron ion implants in silicon wafers to remove undesirable boron clustering, defect evolution, or damage to the lattice created by implant and to recrystallize thin Si amorphous films. The possibility of using this approach to modify the near surface defects in CIGS thin-film solar cells was motivated by the positive results reported for laser processing of silicon wafers. The basic idea is to promote atom mobility by local heating, on a nanometer-length scale; and thus confine the impact of processing to the near-junction region of the device. Results from characterizing the CIGS films and cells suggest that interfacial recombination near the CdS/CIGS metallurgical junction is a major limitation to optimizing of the device performance. The PLA treatment promises to provide defect annealing in the near-surface region, while preserving the beneficial composition gradients in CIGS films.

Another powerful annealing technique using halogen-based RTA process has been widely used in the semiconductor industry. It offers several advantages such as short cycle time, reduced thermal exposure and lot-size flexibility compared to conventional furnaces. Strong demand for thermal-budget reduction and cycle-time reduction had made RTA treatment a popular thermal-processing method in recent years. This technique has been successfully applied to the fabrication of low-cost,

low-thermal-budget silicon solar cells. Conversion efficiency of more than 17% has been reported for RTA processing time of less than 3 minutes [10].

The main scope of this research is to investigate the effects of the above two techniques (PLA and RTA) on CIGS films properties and solar cell performance. Results show that both of these two techniques can positively improve the CIGS cell's performance. In addition, device modeling and investigation of radiation tolerance of CIGS-based solar cells are well discussed in this dissertation.

## CHAPTER 2 LITERATURE REVIEW OF THIN-FILM SOLAR CELLS

### **Current Status of Photovoltaic Technologies**

The photovoltaic (PV) industry has grown at an annual rate of over 20% since 1990's. Many PV manufacturers have invested in expanding their production facilities during the last few years. New PV companies have also been formed in Japan, USA, and Europe to increase the PV module production. Remarkably, Japan manufactures produce almost half of today's world PV modules for terrestrial power generation use. The worldwide PV module production has reached 750 MW in 2004.

In the past few years, most of the PV systems are built using single-crystalline silicon wafers. The key issue and drawback in silicon based PV technology is the reduction of wafer costs, which is difficult to attain with single crystal silicon wafers. As a result, the PV industry has looked into developing low cost thin film PV technologies using alternative semiconductor materials to replace the silicon-wafer-based PV technology. Thin-film solar-cell production accounted for 13% of all PV production in 1999. Single-crystalline and multi-crystalline silicon solar cells are still accounted for most solar-cell production (~84%). Other crystalline products (such as ribbon growth or thin silicon films) contributed only about 3% of the PV modules. The main difficulties of thin-film technology are its bad image of long term stability from the first-generation amorphous silicon PV modules; its low conversion efficiency as compared to crystalline silicon solar cells; the toxicity of some of the materials in fabrication and disposal; and its

short lifetime. All these problems must be resolved if thin-film technology is to take a major share of the booming PV market in the future [11-14].

### **Thin-Film Solar Cells**

The biggest advantage of thin-film technology is that it greatly reduces the manufacturing cost of solar cells by reducing material and deposition cost on large area low cost foreign substrates [15-19]. Typical thin-film solar-cell materials include a-Si:H alloys, CdTe, Cu(In, Ga)Se<sub>2</sub> (CIGS), poly-Si,  $\mu$ c-Si/poly-Si, and dye/TiO<sub>2</sub>. The most advanced and commonly used thin-film technologies are a-Si-alloys, CdTe, and CIGS. Figure 2-1 shows the best performance of these thin-film solar cells.

#### **Amorphous Silicon (a-Si:H) Thin-Film Solar Cells**

Hydrogenated amorphous silicon (a-Si:H) is distinguished from the crystalline silicon (c-Si) by the lack of long-range order (disorder) in the atomic structure and by its high bonded-hydrogen content (~10% in device quality a-Si:H). Although the overall properties of a-Si:H and c-Si materials are similar, the long range disorder in a-Si:H distorts bond lengths and bond angles, which introduces large densities of broken-bond defects and micro voids. The disorder relaxes the momentum conservation rules associated with crystalline materials, thus leading to higher optical-absorption coefficients than in c-Si for photons with energies ( $h\nu$ ) greater than the bandgap energy ( $E_g$ ). The optical band gap of a-Si:H is 1.7 eV and can be fine-tuned by changing the hydrogen content as a function of specific deposition parameters and methods. In addition, a-Si has a higher optical absorption coefficient than c-Si in the visible range of the spectrum and hence the absorber layer thickness of a-Si can be than 1  $\mu$ m.

Typical a-Si:H-based solar cells have a p-i-n superstrate (Figure 2-2a) or n-i-p substrate (Figure 2-2b) structure, depending on the deposition sequence of doped and

intrinsic layers [24]. For both structures, light enters through the p-layer, which efficiently supports hole collection in the device. Heavily doped wide band gap a-SiC:H and a-SiO:H alloys or microcrystalline Si films are applied as p-doped window layers to reduce absorption losses. Electrons and holes generated in the i-layer are driven to the n- and p- layer, respectively, by the internal built-in electric field (Figure 2-3).

The advantage of its unique material properties also makes thin-film a-Si:H an excellent candidate in sophisticated multi-junction solar cell design. Achieved stable conversion efficiencies in excess of 13% [20-23] have been reported for multi-junction a-Si:H thin-film solar cells.

### **The CdTe Thin-Film Solar Cells**

With a direct band gap of  $E_g = 1.45$  eV [25] and steep optical absorption edge, thin-film CdTe solar cells can absorb 90% of the incident sunlight in 1-2  $\mu\text{m}$  absorber layer thickness, and hence are considered as a promising thin-film PV technology. The world record so far was achieved by NREL with 16.5% conversion efficiency. Theoretical maximum efficiency of CdTe solar cells is over 27% [26, 27].

The depositing sequence can be changed for CdS/CdTe solar cells; the frontwall type and backwall type. The most common device structure of CdTe solar cells is the backwall type (Figure 2-4 [25]). The CdTe layer usually is deposited by close-space vapor transport technique. Acting as a filter for sunlight, and with a cut off wavelength of 514 nm, n-type CdS becomes the ideal partner for p-type CdTe absorber to form n-p heterojunction solar cells.

### **The Cu(In,Ga)Se<sub>2</sub> (CIGS) Thin-Film Solar Cells**

The compounds of CuInSe<sub>2</sub> (CIS) and Cu(In,Ga)Se<sub>2</sub> (CIGS) with their chalcopyrite structure, are among the most promising materials used in thin film solar cells [28, 29].

The main advantages of CIS/CIGS-based solar cells are the high conversion efficiency and low cost of materials. Although some problems still prevent the large-scale commercialization and use of CIGS cells for terrestrial power generation, significant progress has been made in CIS/CIGS-based PV technology, and single cell efficiency of 19% and module efficiency exceeding 10% AM1.5G have been achieved in the last couple years.

The CIGS absorber is direct band gap material with bandgap tunable by adjusting the ratio of In to Ga, to maximize absorption of the solar spectrum. Its bandgap can be varied from 1.02 eV (CIS) to 1.68 eV (CGS) (Figure 2-5). Thin-film CIGS material also has a higher absorption coefficient than any other thin-film ( $\alpha > 10^5 \text{ cm}^{-1}$ ) (Figure 2-6), which allows almost 99% of the incoming light to be absorbed with the first micron of the material according to the solar spectrum. Thus, the highest-efficiency (19.2% from NREL) CIGS solar cell (Figure 2-7) is fast approaching the efficiency of already commercialized multi-crystalline silicon cells (20.4%) and is higher than other thin-film PV technologies (Figure 2-1).

The typical structure of CIGS solar cells is shown in Figure 2-8. The CIGS absorber layer is typically deposited on a Mo-coated soda-lime glass (SLG) substrate (Mo/SLG by using PVD), sputtering, PMEE, or RTP deposition technique. A 500 Å CdS buffer layer is deposited on top of the CIGS absorber layer by CBD technique, followed by deposition of a TCO layer such as sputtered ZnO films. Finally, a 500 Å Ni- film and a 3 µm Al metal contact layer are deposited by using electron-beam evaporation technique. Chapter 5 gives detailed description of each layer and device fabrication processes.

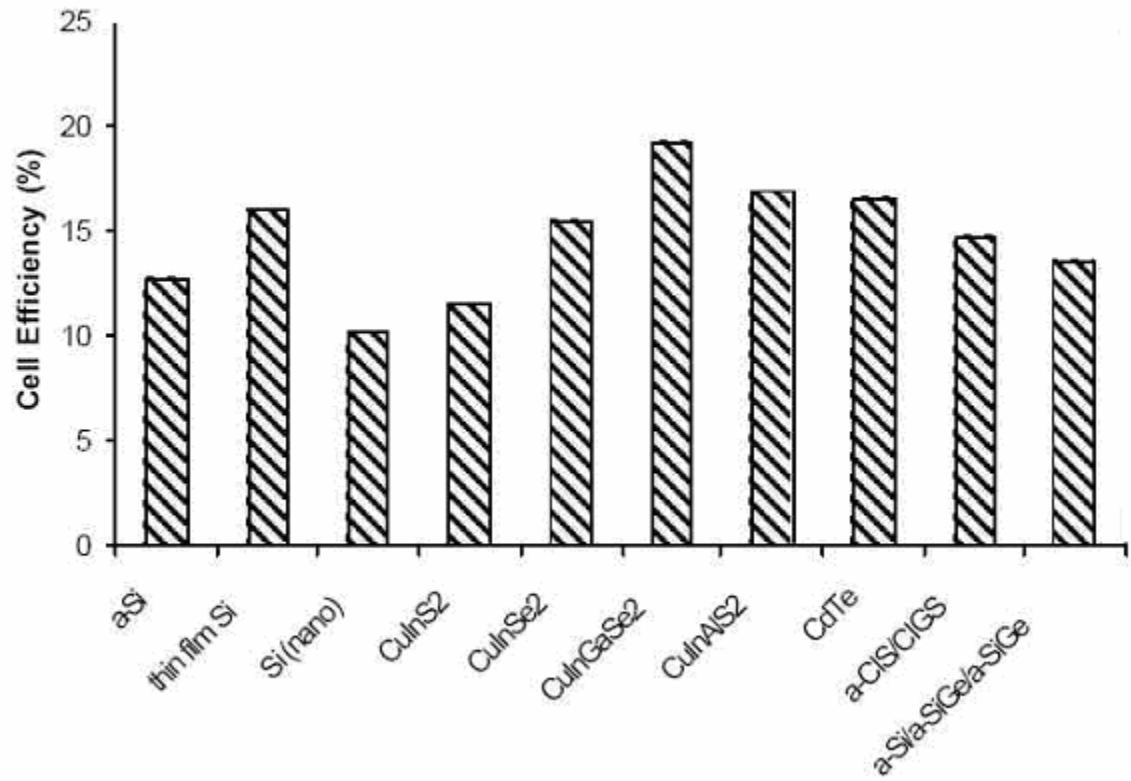
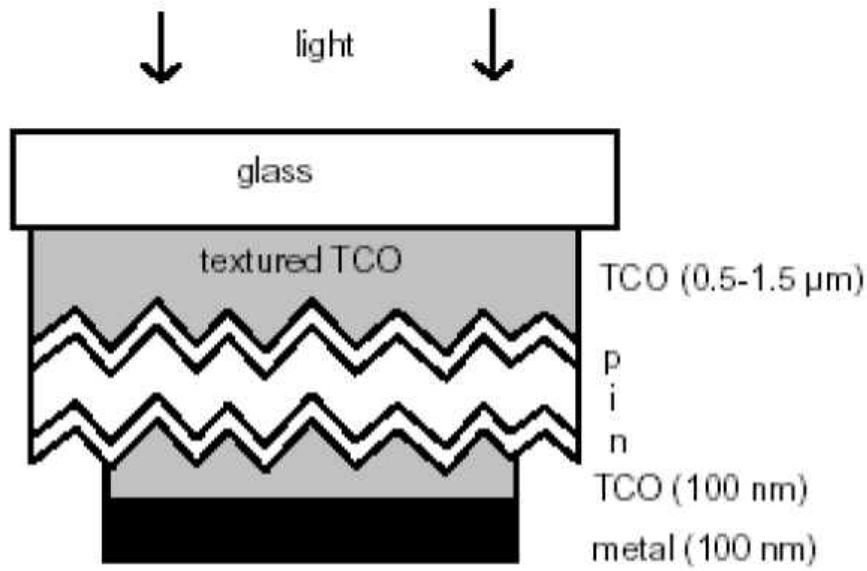
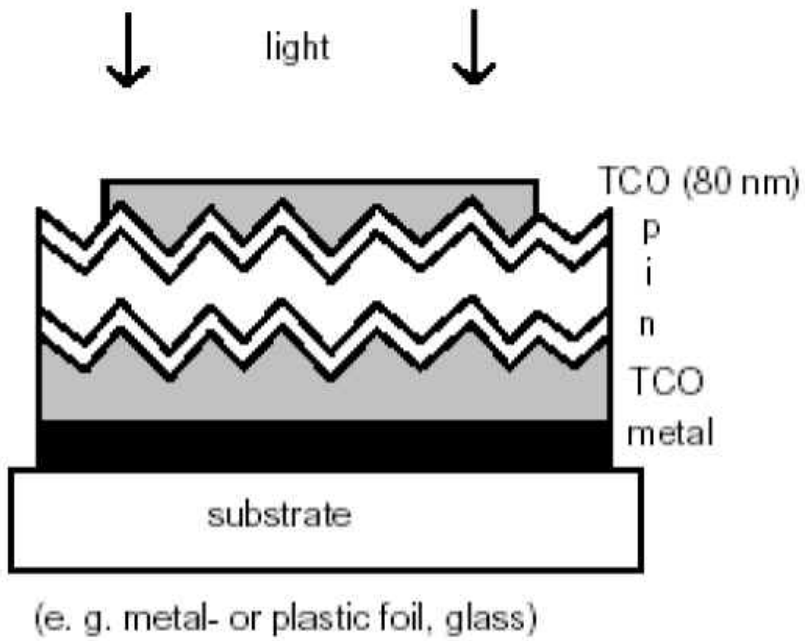


Figure 2-1. Best performance of various thin-film solar cells.



(a)



(b)

Figure 2-2. Sketch of the layer structure for (a) a-Si p-i-n (superstrate), and (b) a-Si n-i-p (substrate) solar cells.



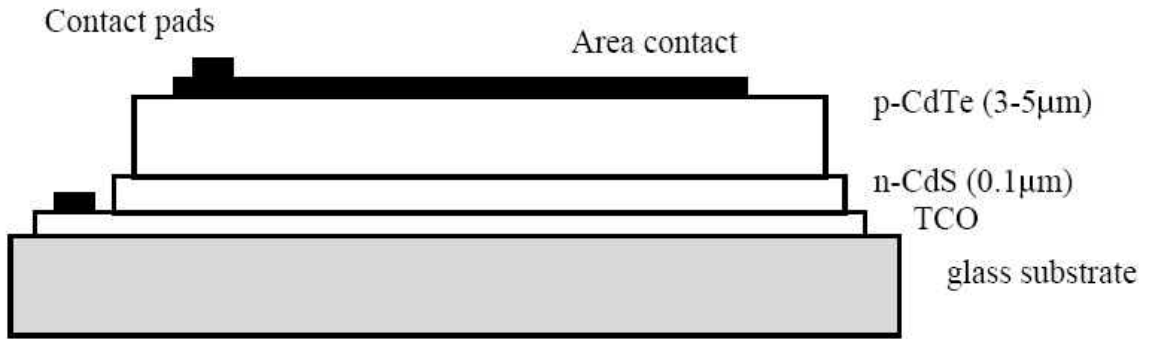


Figure 2-4. Device structure of CdS/CdTe thin-film solar cell.

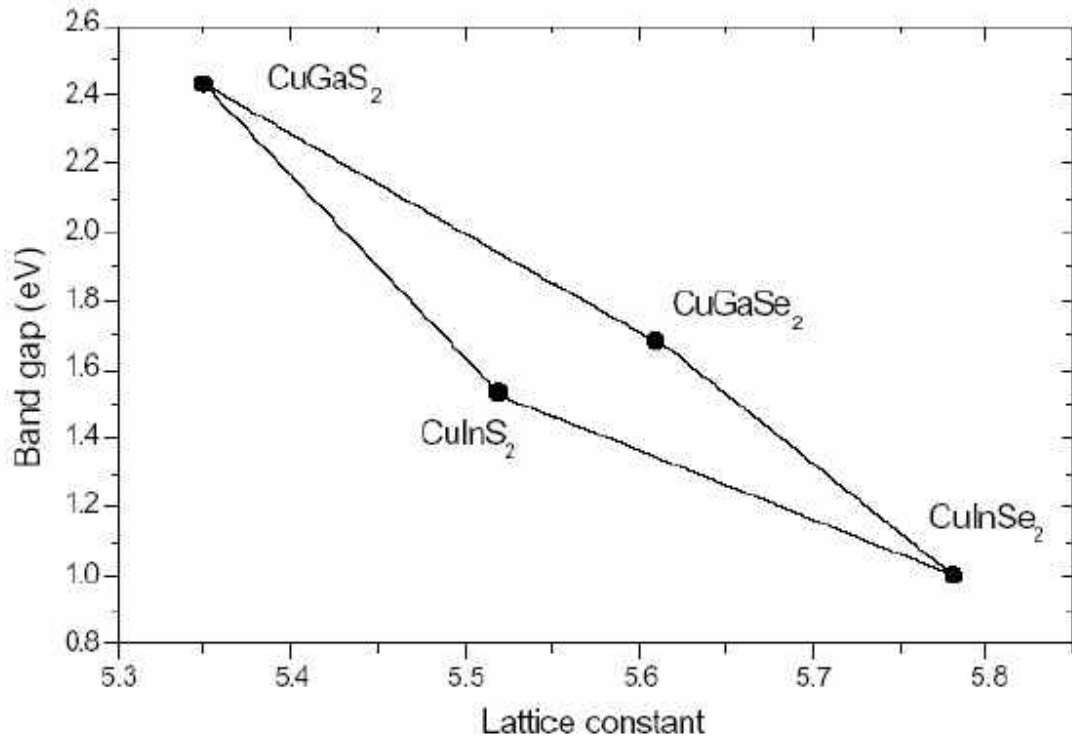


Figure 2-5. Band gap versus lattice constant diagram of CIGS solar cell.

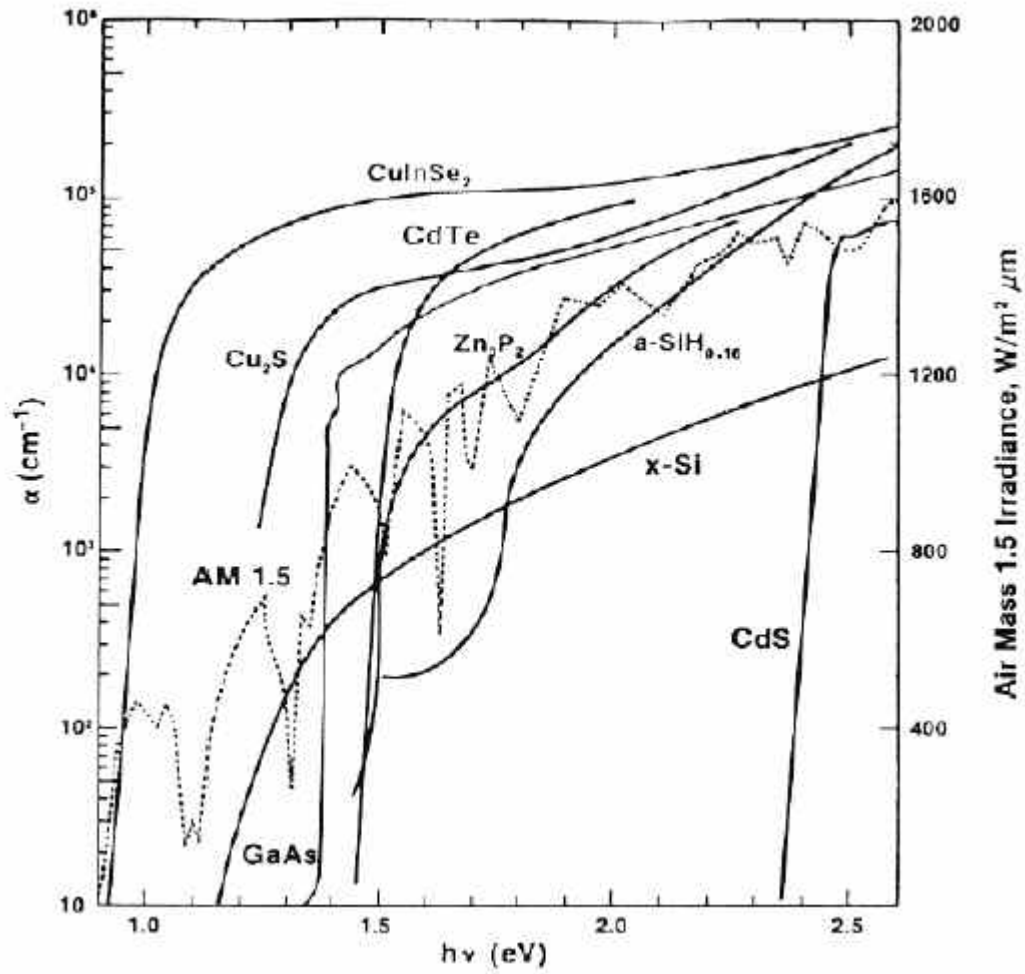


Figure 2-6. Absorption coefficients of different solar cell materials.

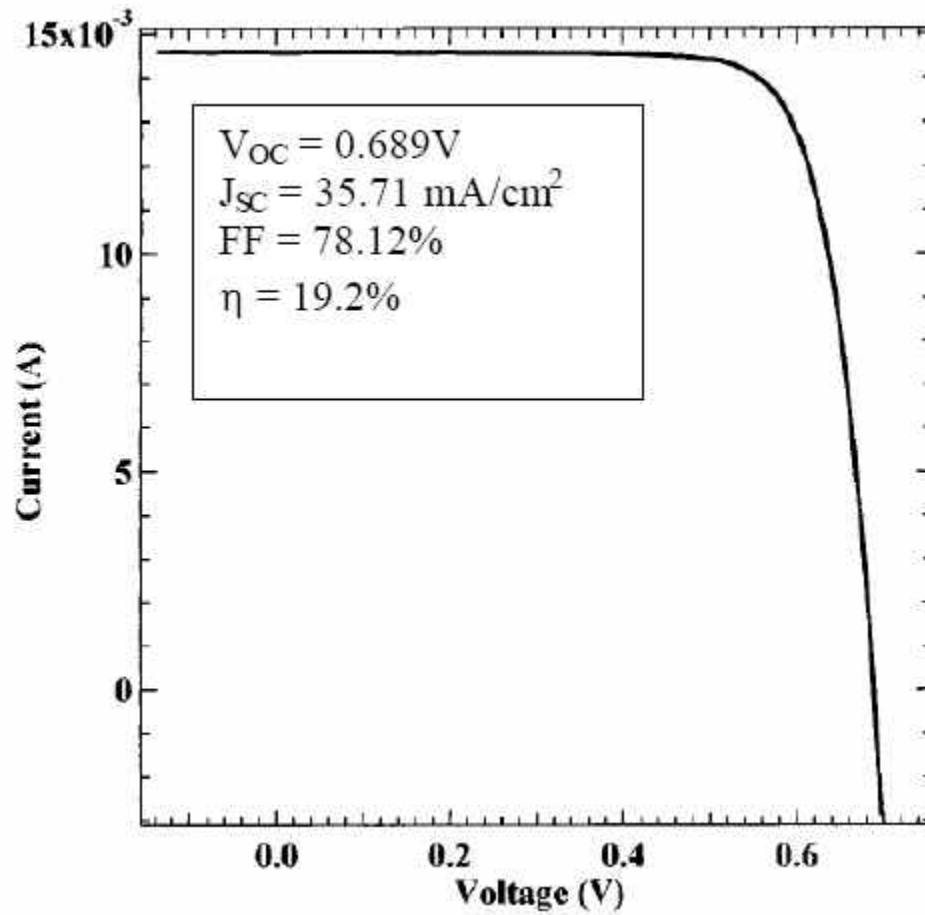


Figure 2-7. Photo- J-V result of 19.2% CIGS solar cell from NREL (under  $1000 \text{ W/m}^2$ , AM 1.5 global spectrum at  $25^\circ\text{C}$ ).

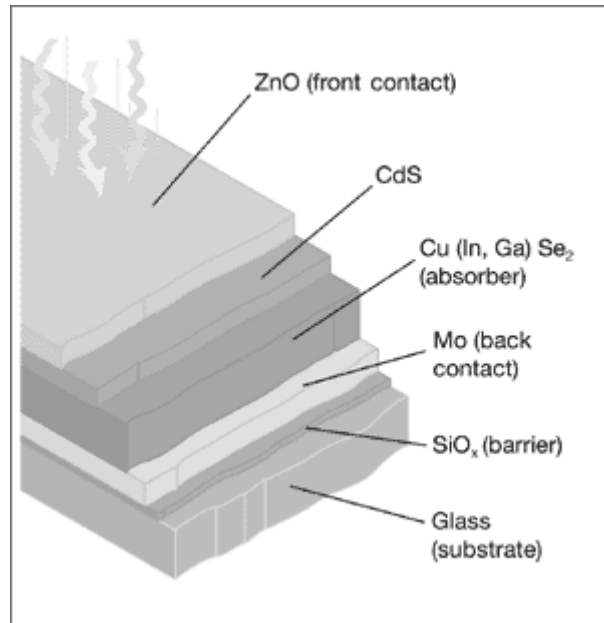


Figure 2-8. Device structure of a CdS/CIGS-based solar cell.

CHAPTER 3  
PULSED LASER ANNEALING (PLA) OF FILM PROPERTIES AND DEVICE  
PERFORMANCE FOR CIGS SOLAR CELLS

Pulsed Laser Annealing (PLA) has been used for the first time to modify near-surface defects and related junction properties in Cu(In,Ga)Se<sub>2</sub> (CIGS) solar cells. Several film surface and device performance characterizations were employed to investigate the effects of PLA on CIGS film and solar cells. In this chapter, the annealing effects, optimal conditions and characterization results are discussed in detail.

**Introduction**

The PLA technique is widely used to activate boron ion implants in silicon wafers and to remove undesirable boron clustering, defect evolution, and damage to the lattice created by the implantation process. Beneficial effects of PLA are derived in part from selective absorption and limiting elevated temperature processing to the near-surface region [30, 31]. The possibility of using this approach to modify the near-surface defects and crystalline structure in Cu(In,Ga)Se<sub>2</sub> (CIGS) thin-film solar cells was motivated by the positive results reported for PLA processing of silicon wafers. The basic idea is to promote atom mobility by local heating on the nanometer length scale and thus confine the impact of processing to the near-junction region of the device. The CIGS cells contain a thin (~ 50 nm) n<sup>+</sup> CdS buffer layer deposited on a thick (~ 1 to 2 μm) p-type CIGS absorber. Although the exact location of the electrical junction relative to the metallurgical one is not known, it does lie near the surface of the absorber. Furthermore, analyses of CIGS film characterization results and cell performance data suggest that

interfacial recombination near the CdS/CIGS metallurgical junction is a major limitation to the device performance. The possibility of repairing damage near this shallow junction, while preserving the composition gradients in the bulk CIGS films motivated exploration of PLA treatment. In this work most of our CIGS absorber films were annealed using a 248 nm pulsed laser beam and the properties of the films and subsequent device performances were compared to those for untreated films. Furthermore, CIGS films were annealed using a 250 ns pulsed 308 nm laser beam with larger beam size at selected laser energy density in the range 30 to 110 mJ/cm<sup>2</sup>. Results of XRD, GIXD and SEM surface characterizations suggested near surface structure changes by PLA.

### **Experimental Details**

The CIGS samples used in this study were provided by the National Renewable Energy Lab (NREL) and Shell Solar Inc. (SSI), and both sample sets were grown on Mo coated soda-lime glass substrates. For the Hall-effect measurements, however, the CIGS films were grown on the insulating soda-lime glass (SLG) substrates. A thin (50 nm) CdS buffer layer was deposited on the CIGS samples using Chemical Bath Deposition (CBD) at 75°C for 30 min. The PLA treatment was carried out using a pulsed 248 nm line derived from a KrF excimer laser system [32]. In the main part of this study the laser pulse width was fixed at 25 ns and the energy density was varied in the range 20 to 60 mJ/cm<sup>2</sup> and the number of pulse cycles in the range 5 to 20. To study the effect of PLA on the CIGS film properties, PLA treatments were performed on the CIGS films with and without CdS buffer layers. After PLA treatments, a ZnO window layer was deposited on the CdS/CIGS/Mo/SLG sample by RF sputtering. Subsequent metallization (Ni-Al front contact grids) was carried out by e-beam evaporation through a shadow-mask. Finally, finished devices were produced by cutting the sample into separate cells with 0.429 cm<sup>2</sup>

active area and attaching wires with Indium bumps on the Mo-coated glass substrates for back contacts. Detailed fabrication process is discussed in Chapter 5. The performance of these cells was then tested as described in the next section.

### **Results of PLA Treated CIGS Films**

The non-destructive Dual Beam Optical Modulation (DBOM) characterization method was used to measure the effective carrier lifetimes in the CIGS absorbers [33, 34], and to evaluate the effect of PLA treatment on the performance of CIGS cells. Within the sensitivity of the DBOM technique, the effective carrier lifetime was found to increase for CIGS films on Mo/SLG annealed using 5 cycles of laser pulse with an energy density in the range 30 to 60 mJ/cm<sup>2</sup>. The results (Table 3-1) show that a low energy PLA treatment can increase the effective carrier lifetime of the annealed samples and improve the performance of CIGS cells.

XRD patterns of CIGS and CdS/CIGS samples before and after PLA treatments show substantial narrowing of the diffraction peaks that belong to CIGS (Figure 3-1). These results can be interpreted as an improvement of the layer's crystallinity after PLA treatment, which is consistent with the observed increase of the grain size (SEM) and the effective carrier lifetime in the CIGS films.

As illustrated by SEM micrographs (Figure 3-2), the surface morphology and apparent grain size increased upon laser annealing. This result suggests that the energy density used was sufficient to cause atomic rearrangement in the near surface region, and thus the potential exists to modify the atomic defects in the near surface region.

Based on the encouraging DBOM results from the initial PLA treated CIGS samples, a second set of experiments were performed in which the energy density and number of the incident laser pulse were varied. Hall-effect measurements were made on

the CIGS samples without a Mo layer prior and after annealing to determine the effects of PLA treatment on the carrier concentration, carrier mobility, and sheet resistivity of CIGS films.

Four CIGS films deposited on the glass substrate underwent pulsed PLA treatments at room temperature. Hall-effect measurements (using an MMR Hall and Van Der Pauw measurement system) were made for all samples before and after the PLA treatments. The results (Table 3-2) show a significant increase in the values of Hall mobility and a decrease in film resistivity following PLA treatment. The carrier mobility in the PLA treated CIGS films were 3 to 4 times greater than the values before annealing. Although the hole concentration decreased slightly after annealing, film resistivities decreased by 72 and 64% for CIGS films (samples H1 and H2) treated at an energy density of 20 mJ/cm<sup>2</sup> with 10 and 20 laser pulses, respectively. At an energy density of 40 mJ/cm<sup>2</sup>, the film resistivity was reduced by more than 95% from that of the non-annealed samples (H3 and H4). Thus, both the energy density and the number of laser pulse play an important role in determining the resistivity of PLA treated CIGS absorber layers.

### **Results of First Set of PLA Treated CIGS Solar Cells**

#### **Photo- J-V Measurements of PLA CIGS Cells**

Four CIGS/CdS samples were annealed by a 50 mJ/cm<sup>2</sup> laser beam with different pulse number. Two samples were followed by a 100 Å extra CdS buffer layer re-growth after PLA treatment on the CIGS samples initially coated with a 400 Å CBD CdS buffer layer, and one control sample without any treatment. These samples were then fabricated into cells for testing. The DBOM and photo- J-V results (Table 3-3) show an increase in the effective carrier lifetimes on the PLA treated samples. No explicit improvements, however, were found in the photo- J-V results of the annealed cells. The

data also show slight decreasing in the fill factor and conversion efficiency of cells annealed with 20 pulses PLA compared with the 10-pulse-annealed cells. Some high energy density (i.e., 80 mJ/cm<sup>2</sup>) PLA treatments were also used on other CIGS samples, and the results show a drastic reduction in the cell efficiency. These results suggest that an optimal PLA energy density should be less than 50 mJ/cm<sup>2</sup>, and no significant influence on the cell performance because of the additional CdS buffer layer re-growth was found in this study.

### **The Q-E Measurement of PLA CIGS Cells**

Two CIGS films with a 500 Å CdS buffer layer were annealed at an energy density of 50 mJ/cm<sup>2</sup>, and then fabricated into cells. To study the effect of pulsed PLA treatment, the spectral response and quantum efficiency (Q-E) were measured on these cells. The results (Figures 3-3, 3-4) indicate that for incident light with wavelengths greater than 650 nm, the Q-E and spectral response of the PLA cells are higher than those of the control cell, indicating that the PLA treatment increases the effective carrier lifetime and diffusion length in the absorber layer and hence increases the short-circuit current density in comparison to the control cell without PLA treatment. In the short wavelength regime ( $\lambda < 0.65 \mu\text{m}$ ), however, the Q-E and spectral response decrease after PLA treatment, which suggest damages near the interface region of CIGS/CdS films by the laser beam. As a result, the surface recombination velocity is increased and the Q-E and spectral response are lower in the shorter wavelength region. It is also noted that the values of Q-E and spectral response for sample annealed with 20 cycles laser pulse were found to be lower than the sample with 10 cycles of annealing pulse with same energy density.

## Results of Second Set of PLA Treated CIGS Solar Cells

### Photo- J-V Results

Since the previous results suggest that an optimal PLA energy density should be less than  $50 \text{ mJ/cm}^2$ , an additional set of CIGS/CdS samples treated by PLA with different energy densities (less than  $50 \text{ mJ/cm}^2$ ) and pulse number were fabricated into finished devices. Six CdS/CIGS samples treated by PLA with selected energy density and pulse number plus one control sample without PLA treatment were fabricated into finished devices. There were five cells on each device and each cell was tested using a photo- J-V system at room temperature. The PLA conditions and averaged photo- J-V results of these devices are summarized in Table 3-4 and Figure 3-5. Note that the data in Table 3-4 were averaged from the measured values of five cells on each device and the standard deviation computed on the 5- cell measurements. In these experiments, improvements were found in the photo- J-V results of the annealed devices under  $30 \text{ mJ/cm}^2$ , using 5 or 10 pulses (CIGS-D1 and CIGS-D2), as compared to results from the control sample (Ctrl-D). The data also show degradation in cell performance parameters such as open circuit voltage ( $V_{oc}$ ), short-circuit current ( $J_{sc}$ ), Fill Factor ( $F.F.$ ), and cell efficiency ( $\eta_c$ ) of the devices laser annealed with energy densities higher than  $30 \text{ mJ/cm}^2$ . It was also found that for devices annealed at the same energy density, the fill factor and conversion efficiency of the 5-cycle annealed devices are higher than those of 10-cycle annealed devices. These results suggest that an optimal PLA energy density and pulse number are approximately  $30 \text{ mJ/cm}^2$  and 5 pulses, respectively.

### Dark- J-V Results

To better understand the specific differences between the control cell and the two  $30 \text{ mJ/cm}^2$  PLA treated cells, dark- J-V and quantum efficiency (Q-E) measurements as

well as theoretical calculations of device parameters were made for selected cells from each of the three devices (Ctrl-D, CIGS-D1 and CIGS-D2).

The J-V characteristics for a p-n junction solar cell under uniform illumination condition [35, 36] are expressed by Equation 3-1.

$$J(V) \cong J_0 \left( \exp \frac{q(V - R_s J)}{nkT} - 1 \right) + \frac{V - R_s J}{R_{sh}} - J_{ph} \quad (3-1)$$

Where  $J_{ph}$ ,  $J_0$ ,  $n$ ,  $R_s$  and  $R_{sh}$  are the photocurrent density, saturation current density, diode ideality factor, series resistance, and shunt resistance, respectively.

To study the effect of pulsed PLA treatment on the diode characteristics, photo- and dark- J-V measurements were performed at room temperature for each the selected cell. The measured parameters and calculated values of  $J_0$ ,  $n$ , and  $R_s$  [37, 38] are summarized in Table 3-5 (note that  $R_{sh}$  is quite high in all tested CIGS cells).

From the dark- J-V curves (Figure 3-6, 3-7), both dark current density and saturation current density,  $J_0$ , of the PLA treated cells are consistently smaller as compared to the control cell. These curves suggest that the recombination current through surface defects dominates the dark- J-V curve under forward bias condition before PLA treatment (with diode ideality factor  $n > 4$ ). After the PLA treatment, a significant reduction in the dark current density was observed apparently because of reduction of surface defect density, and the recombination current was dominated by bulk defects in the junction space charge region at higher bias ( $n \approx 2$ ). These results indicate that defects in the surface region and interface of absorber and buffer layers can be effectively reduced by PLA treatment, thus decreasing the recombination of minority carriers via interface states and defects in the junction space-charge region of CdS/CIGS cells.

Although cells treated by the PLA exhibit higher series resistance ( $R_s$ ), the negative effect

of  $R_s$  increase on the diode characteristic remains relatively small because of the extremely low value of  $J_o$ .

### **Quantum Efficiency Results**

The quantum efficiency (Q-E) was measured on the control and PLA treated cells. The results (Figure 3-8) indicate that for incident light with wavelengths greater than 480 nm, the Q-E of the PLA cells is higher than that of the control cell, indicating that the PLA treatment improves the effective carrier lifetime and diffusion length in the absorber layer and hence increases the short-circuit current density in comparison with the control cell. In the shorter wavelength regime ( $\lambda < 0.48 \mu\text{m}$ ), no improvement of Q-E was observed between the control cell and the PLA treated cells. It is also noted that values of the Q-E for cell annealed with 10 cycles of laser pulse were found to be lower than that of the cell with 5 cycles of laser pulse at same energy density, again suggesting that the optimal laser pulse number is between 5 and 10 cycles.

### **The C-V and DLTS Characterizations**

In order to investigate the defect property change after PLA processing of CIGS cells, the Deep-level transient spectroscopy (DLTS) and C-V measurements were employed on 2 finished CIGS devices with  $30 \text{ mJ/cm}^2$ , 10 pulses and without PLA treatment. The DLTS measurement was performed with a reverse bias ( $V_R$ ) of 0.5 V, a trap-filling pulse amplitude of 0.7 V, and a saturation pulse width of 10 ms. The DLTS spectra were shown in Figure 3-9 and the DLTS measurement results were summarized in Table 3-6. As shown in Table 3-6. A minority carrier trap with an activation energy of  $0.065 \sim 0.069 \text{ eV}$ , which was quite close to the shallow donor energy level ( $\sim 0.06 \text{ eV}$ ) known as the selenium vacancy ( $V_{Se}$ ), was detected, and its density was reduced by about 50% after PLA treatment.

### **Additional PLA Effect Study**

Furthermore, CIGS films were annealed using a new 250 ns pulsed 308 nm laser beam with larger beam size in France at selected laser energy density in the range 30 to 110 mJ/cm<sup>2</sup>. XRD, GIXD and SEM surface characterizations were made which suggest near surface structure changes. The sample number and annealing condition are shown in Table 3-7 below.

To study the laser annealing effect on film surface morphology by this new pulsed laser annealing system, 5 identical CdS/CIGS films were annealed at selected laser energy densities in the range 30 to 110 mJ/cm<sup>2</sup>, 5 pulses. As illustrated by SEM micrographs (Figure 3-10, 3-11), the surface morphology and apparent grain size increased upon laser annealing with energy density of 70 mJ/cm<sup>2</sup> or higher. This result suggests that the selected energy densities were sufficient to cause atomic rearrangement in the near surface region, and thus the potential exists to modify the atomic defects in the near surface region.

From the XRD and GIXD plots (Figure 3-12, 3-13 and 3-14), new CdS peaks and shoulders (at 25, 28.5, and 48.3 degree) were observed as the energy density was increased, suggesting a significant improvement of the crystallinity of the buffer layer after the PLA treatment. For Figure 3-14, by using a smaller grazing incident angle ( $\Omega=1^\circ$ ), the analysis is more sensitive to the sample surface. As one can see, the new CdS peaks become sharper compared to Figure 3-12 and 3-13, indicating a higher crystallinity for the topmost part of the buffer layer. Comparing Figure 3-14 with 3-12 and 3-13, we found that the film surface changes more than bulk. Close look at the new peaks in all figures, we found that the peaks appear only when the energy density is equal or greater than 70 mJ/cm<sup>2</sup>, (sample #3, 4 and 5) which suggest 70 mJ/cm<sup>2</sup> might be a critical

threshold PLA condition. This energy density value could represent the melting threshold for the buffer layer.

### **Summary**

The results of pulsed PLA treatment on the film properties and the performance of CIGS solar cells are very encouraging. Examination of the structural and electrical properties of films from 2 different sources clearly showed the annealing step modified the near surface region. Increased surface feature size evidenced in SEM photos and CIGS diffraction peak narrowing is consistent with increased crystallinity. Furthermore, DBOM measurements of the effective carrier lifetime indicated the lifetime could be increased by as much as a factor of 2.75. Hall measurements of CIGS samples deposited on SLG revealed PLA treatment increased the mobility and resistivity and decreased the net free hole concentration of each sample, consistent with the hypothesis of annealing out electrically active defects in the near surface region. Based on a parametric study, the best PLA result was obtained with a pulsed laser energy density of  $30 \text{ mJ/cm}^2$  and 5 pulse cycles. J-V and Q-E measurements were also made to study the effect of PLA treatment at the best condition on the performance of CIGS cells. The results show that pulsed PLA treatment has a beneficial effect on the cell performance with the cell efficiency increasing from 7.69 to 12.22 and 13.41% after annealing 2 different samples prior to device processing. The energy density of the laser beam and the number of pulse cycle were found to play a key role in changing the optical and electrical properties of the CIGS films and hence the cell performance.

Based on these promising results, future efforts will focus on PLA study using a commercial type of Excimer laser system that offers a large laser beam size with uniform surface energy density and variable pulse widths and scan rates to access a wider range of

PLA treatment conditions. In particular, it is hoped that a variable pulse width and wavelength will allow control of the anneal depth. Given its application to other industrial materials, laser annealing has the potential to be an effective method to improve solar cell performance in an industrial setting.

Table 3-1. Effective minority carrier lifetime ( $\tau$ ) of CIGS films before and after PLA treatment as measured by DBOM

Sample #	$\tau$ before PLA (ns)	$\tau$ after PLA (ns)	PLA condition (mJ/cm <sup>2</sup> , pulses)
CIGS-S1	1.77	4.87	30, 5
CIGS-S2	2.82	3.39	40, 5
CIGS-S3	4.11	5.43	50, 5
CIGS-S4	4.51	6.31	60, 5

Table 3-2. Hall-effect results for CIGS films before and after PLA treatments

Sample #	Hole-concentration* ( $10^{16}/\text{cm}^{-3}$ )	Hall-mobility* ( $\text{cm}^2/\text{V-s}$ )	Resistivity* ( $\Omega\text{-cm}$ )	PLA condition ( $\text{mJ}/\text{cm}^2$ , pulses)
CIGS-H1	<i>0.53 / 0.445</i>	<i>8.89 / 37.6</i>	<i>133 / 37.3</i>	<i>20, 10</i>
CIGS-H2	<i>2.9 / 2.43</i>	<i>0.93 / 2.98</i>	<i>235 / 86.4</i>	<i>20, 20</i>
CIGS-H3	<i>4.3 / 1.8</i>	<i>1.54 / 6.1</i>	<i>94 / 2.67</i>	<i>40, 10</i>
CIGS-H4	<i>7.1 / 3.3</i>	<i>0.60 / 2.8</i>	<i>148 / 4.64</i>	<i>40, 20</i>

\* Data taken before/after PLA treatments

Table 3-3. Effective lifetimes and photo- J-V results of PLA CIGS/CdS samples and devices

Sample #	Lifetime (ns)	Voc (V)	Jsc (mA/cm <sup>2</sup> )	F.F. (%)	Eff. (%)	PLA condition (mJ/cm <sup>2</sup> , pulses)
CIGS/CdS #0	3.76	0.42	27.2	53.11	6.14	N/A
CIGS/CdS #1	4.77	0.45	24.83	54.43	6.17	50, 10
CIGS/CdS #2	4.11	0.44	26.98	51.37	6.15	50, 20
CIGS/CdS #3	5.2	0.45	26.19	54.06	6.27	50, 10 *
CIGS/CdS #4	3.86	0.39	26.43	44.25	4.57	50, 20 *

\* CdS re-growth was performed after PLA treatment.

Table 3-4. Photo-J-V performance of control cell and PLA-treated CIGS solar cells

Device #	$V_{oc}$ (V)	$J_{sc}$ (mA/cm <sup>2</sup> )	F.F. (%)	$\eta_c$ (%)	PLA condition (mJ/cm <sup>2</sup> , pulses)
CIGS-D1	0.576	31.60	66.50	12.07	30, 5
CIGS-D2	0.568	31.25	63.11	11.12	30, 10
CIGS-D3	0.497	26.79	55.29	7.368	40, 5
CIGS-D4	0.493	26.71	53.08	7.040	40, 10
CIGS-D5	0.436	25.56	51.80	5.773	50, 5
CIGS-D6	0.433	25.23	47.77	5.201	50, 10
Ctrl-D	0.543	30.05	55.74	9.064	N/A

Table 3-5. Photo- J-V performance and dark- J-V parameters for the control cell and selected PLA-treated CIGS cells

Cell #	Ctrl-D-C3	CIGS-D1-C3	CIGS-D2-C3
PLA condition	<i>None</i>	<i>30 mJ/cm<sup>2</sup>, 5 pulses</i>	<i>30 mJ/cm<sup>2</sup>, 10 pulses</i>
Cell area (cm <sup>2</sup> )	<i>0.429</i>	<i>0.429</i>	<i>0.429</i>
V <sub>oc</sub> (V)	<i>0.528</i>	<i>0.577</i>	<i>0.572</i>
J <sub>sc</sub> (mA/cm <sup>2</sup> )	<i>29.78</i>	<i>34.24</i>	<i>32.00</i>
F.F. (%)	<i>48.86</i>	<i>67.88</i>	<i>66.78</i>
Efficiency (%)	<i>7.69</i>	<i>13.41</i>	<i>12.22</i>
V <sub>m</sub> (V)	<i>0.365</i>	<i>0.458</i>	<i>0.453</i>
J <sub>m</sub> (mA/cm <sup>2</sup> )	<i>21.37</i>	<i>28.99</i>	<i>26.88</i>
N	<i>~4.13</i>	<i>~1.98</i>	<i>~1.96</i>
J <sub>0</sub> (mA/cm <sup>2</sup> )	<i>~3.22×10<sup>-3</sup></i>	<i>~1.1×10<sup>-3</sup></i>	<i>~1.06×10<sup>-3</sup></i>
R <sub>s</sub> (Ω)	<i>~10.17</i>	<i>~14.06</i>	<i>~15.94</i>

Table 3-6. Results of the DLTS measurements on the control cell and PLA treated CIGS solar cells

Cell #	Control cell	PLA cell (30 mJ/cm <sup>2</sup> , 10 pulses)
Trap type	<i>Minority (electron)</i>	<i>Minority (electron)</i>
Trap activation energy, E <sub>a</sub> (eV)	<i>E<sub>c</sub>- 0.069</i>	<i>E<sub>c</sub>- 0.065</i>
Trap density, N <sub>t</sub> (cm <sup>-3</sup> )	<i>5.6 × 10<sup>13</sup></i>	<i>2.8 × 10<sup>13</sup></i>

Table 3-7. Annealing condition of new PLA samples

Sample #	Energy density (mJ/cm <sup>2</sup> )	Pulse #	Note
1	30	5	<i>PLA sample</i>
2	50	5	<i>PLA sample</i>
3	70	5	<i>PLA sample</i>
4	90	5	<i>PLA sample</i>
5	110	5	<i>PLA sample</i>
Ctrl	<i>N/A</i>	<i>N/A</i>	<i>Control sample</i>

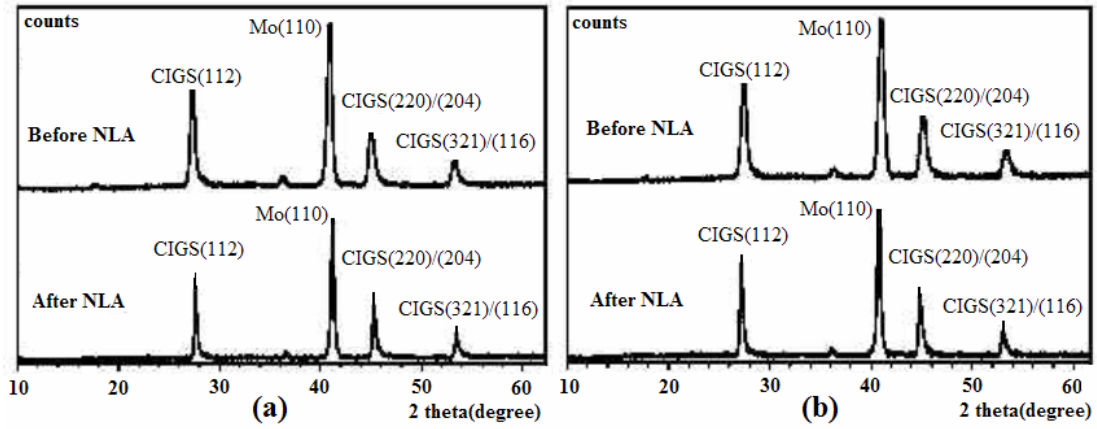


Figure 3-1. XRD spectra before and after PLA treatments for (a) a CIGS and (b) a CdS /CIGS sample.

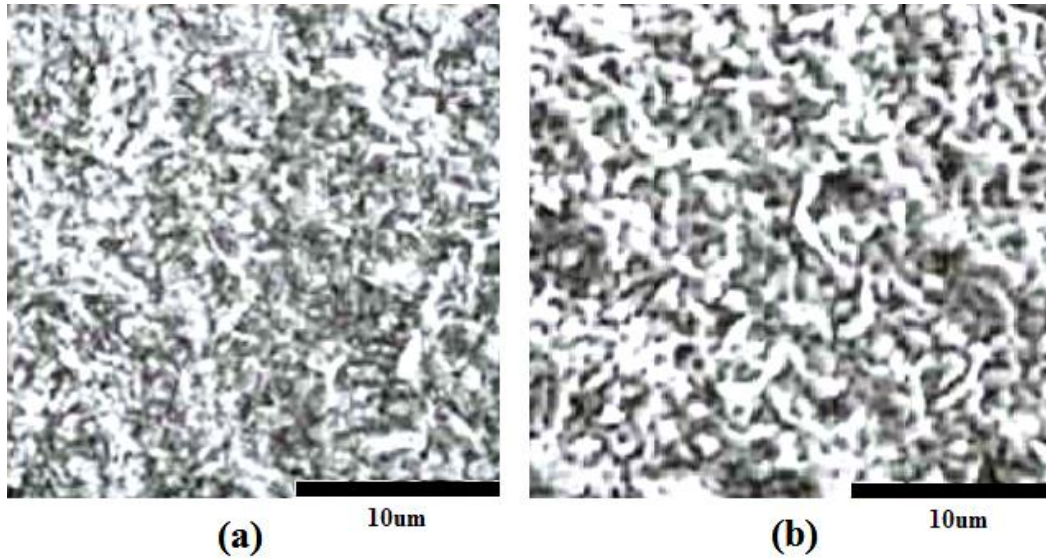


Figure 3-2. Surface morphology of CIGS films (a) without and (b) with PLA treatments at an energy density of  $55 \text{ mJ/cm}^2$  (SEM images with magnification of 6000x).

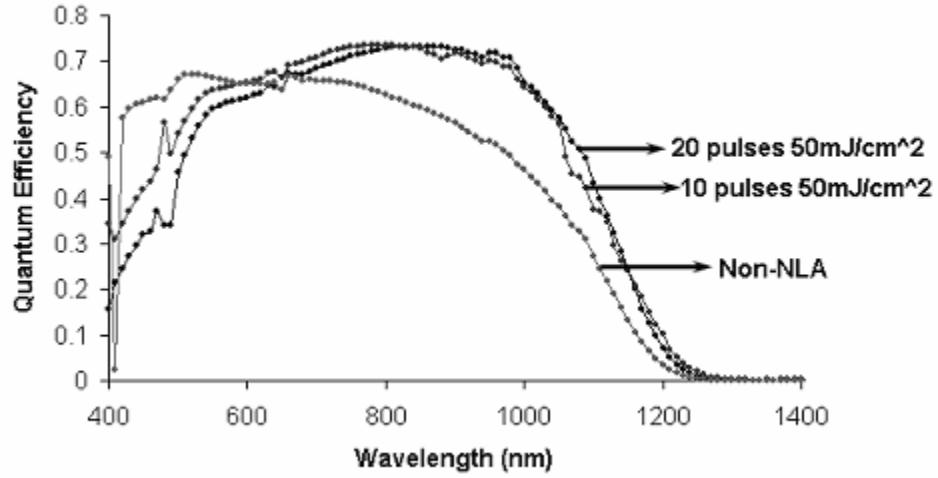


Figure 3-3. Quantum efficiency of CIGS cells with and without PLA treatment.

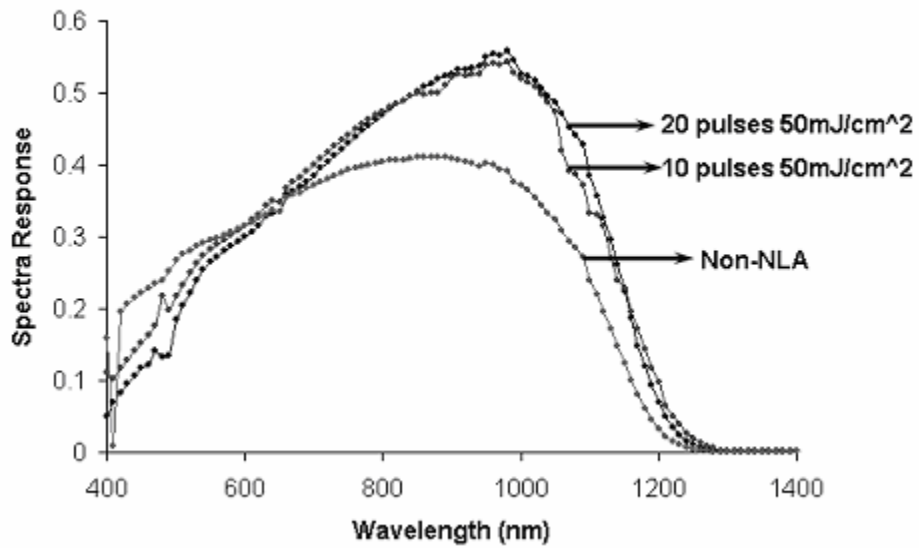


Figure 3-4. Spectral response of CIGS cells with and without PLA treatment.

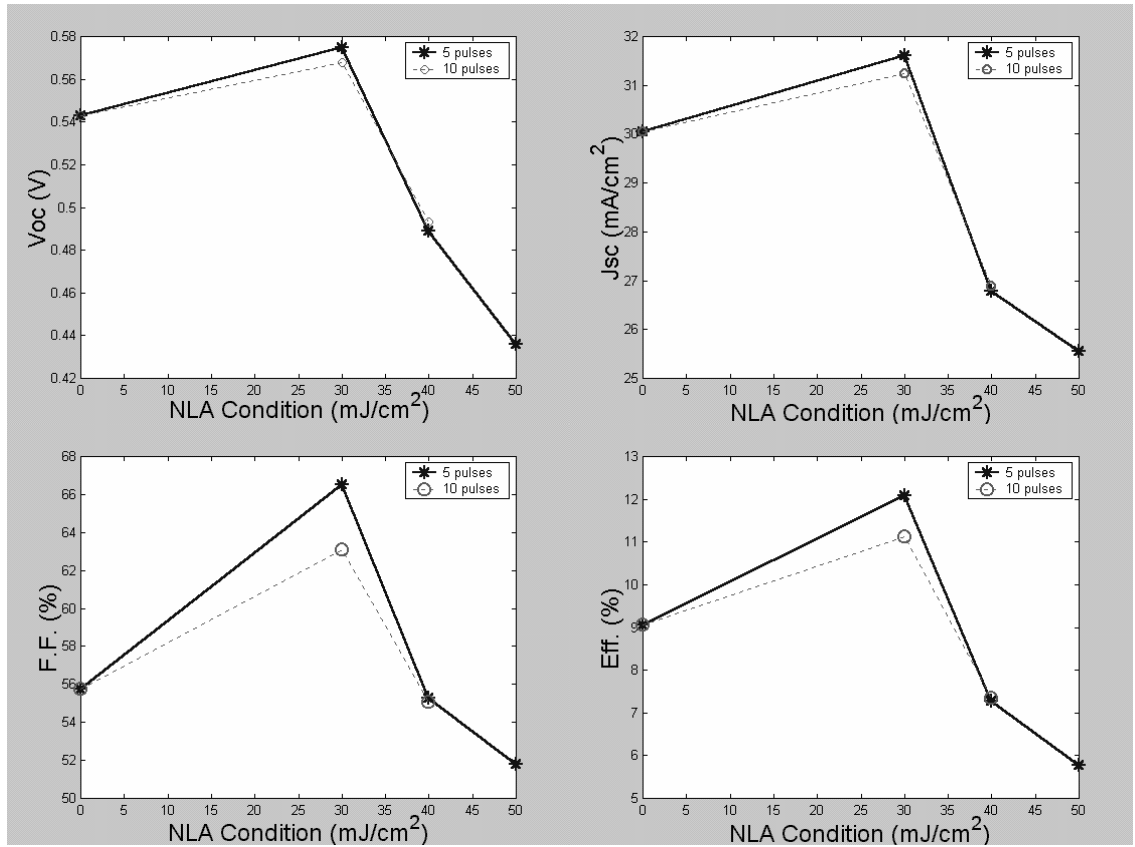


Figure 3-5. Photo- J-V parameters versus different PLA condition.

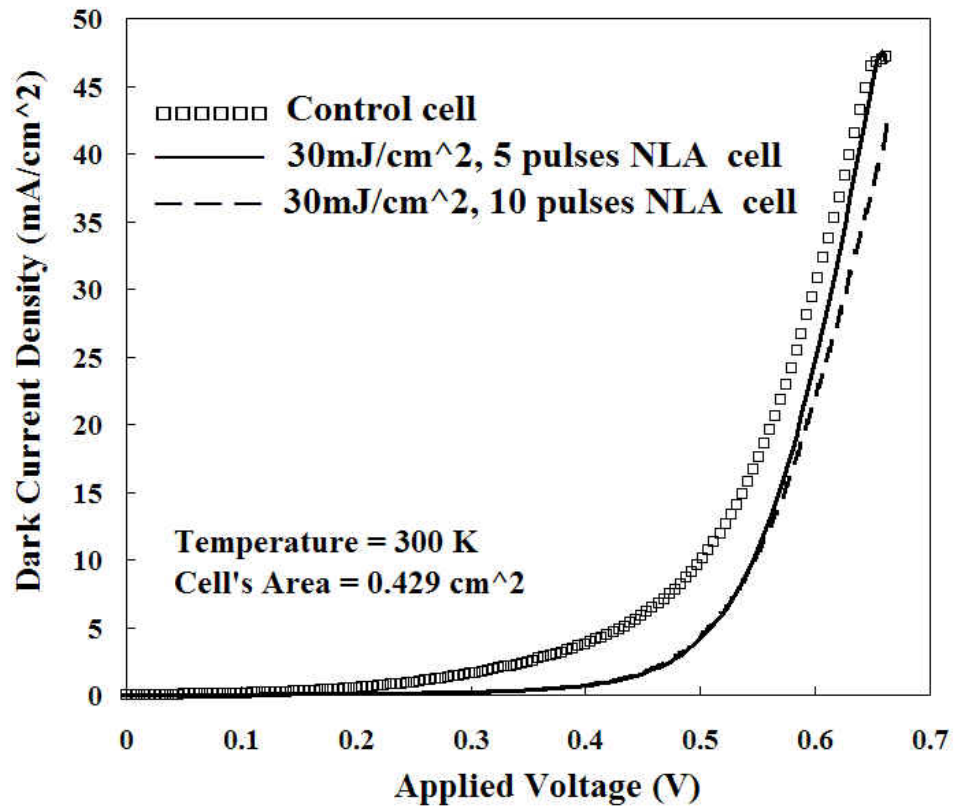


Figure 3-6. Dark- J-V curves comparing the control cell to two PLA treated cells.

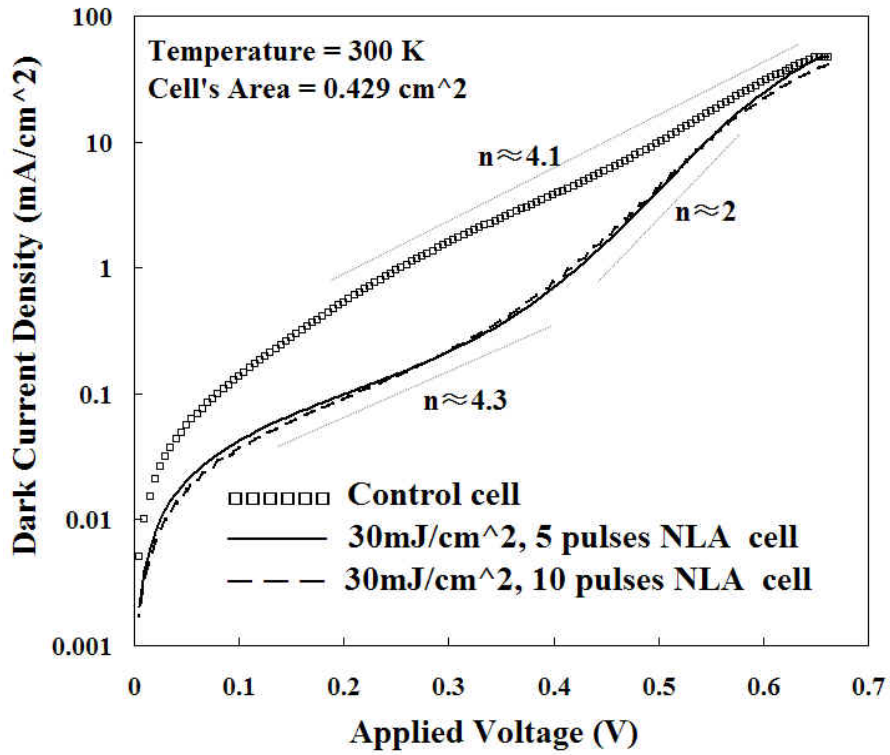


Figure 3-7. Dark- J-V curves (semi-log plot) of the control cell and two PLA treated cells.

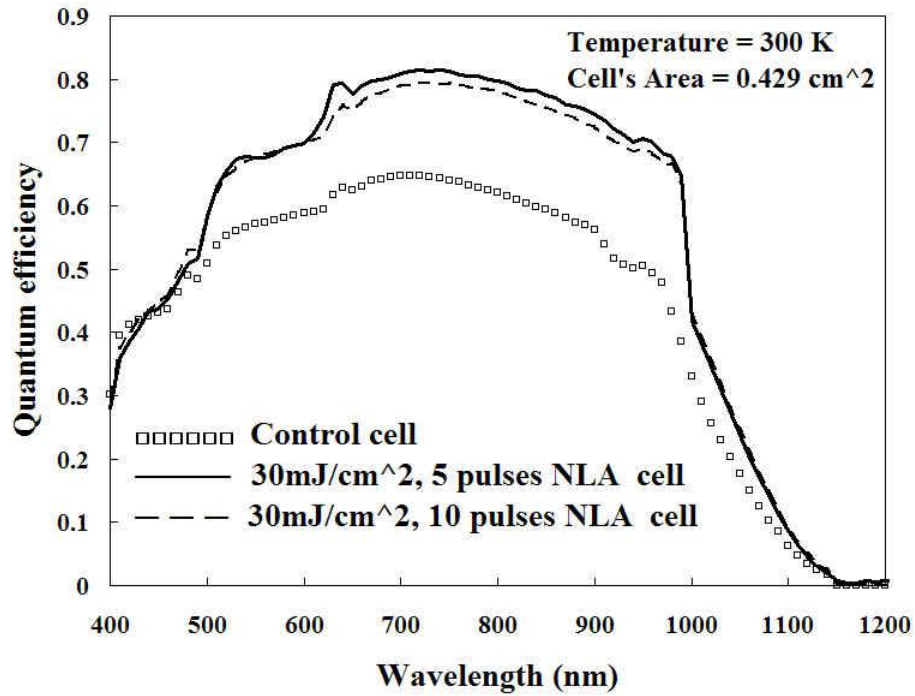


Figure 3-8. Quantum efficiency (Q-E) versus wavelength comparing the control cell to the two PLA-treated cells.

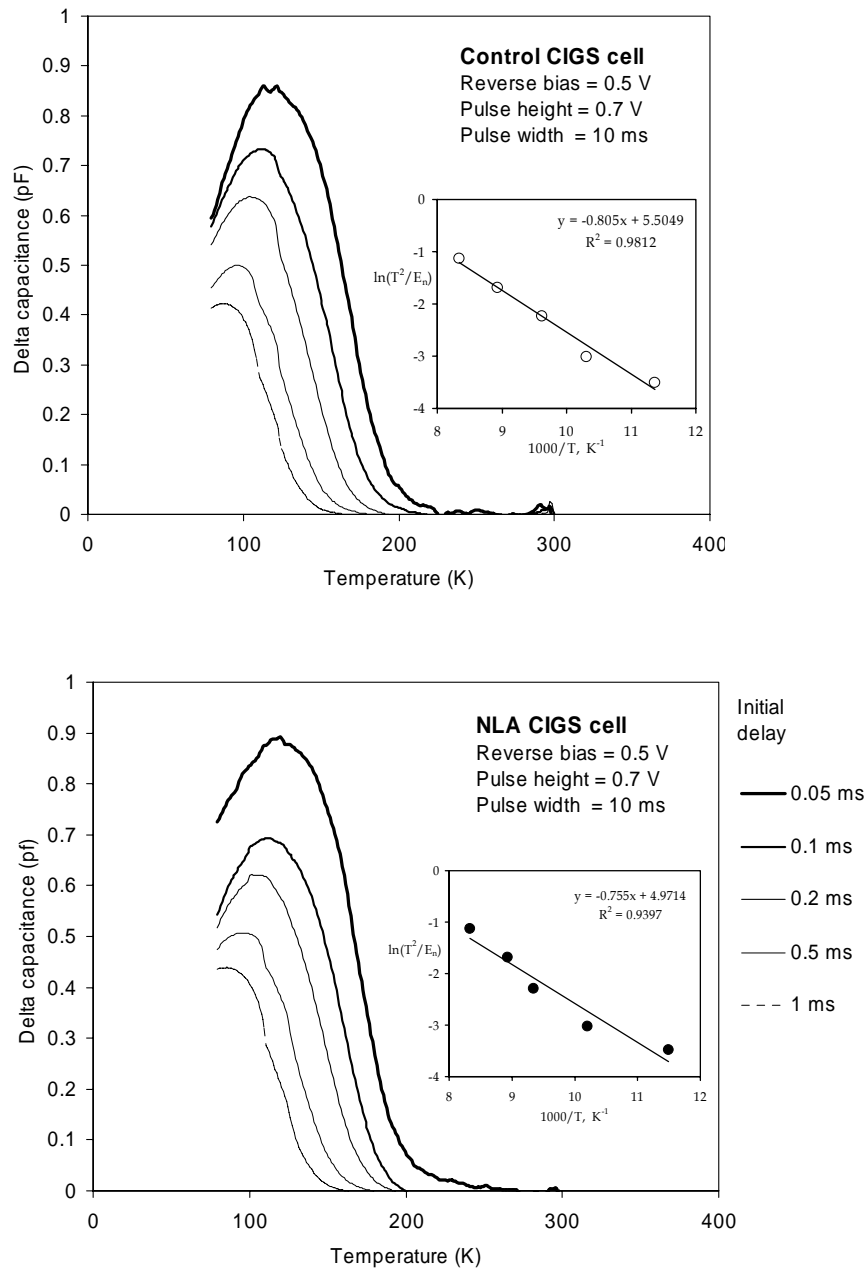


Figure 3-9. The DLTS scans of the control- and PLA- CIGS cell.

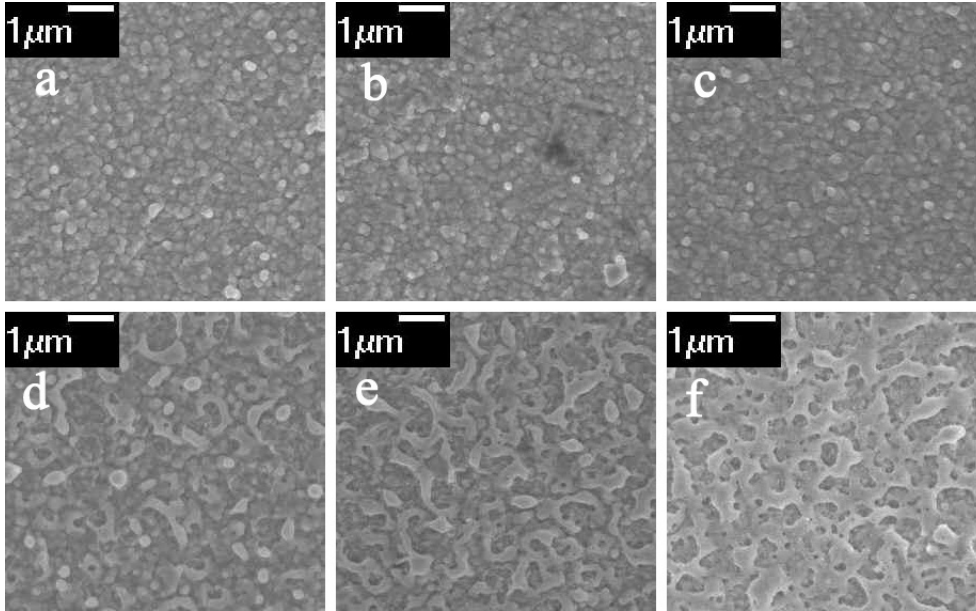


Figure 3-10. Surface morphology of CdS/CIGS films (a) before and after PLA treatment with energy densities at (b) 30 mJ/cm<sup>2</sup>, (c) 50 mJ/cm<sup>2</sup>, (d) 70 mJ/cm<sup>2</sup>, (e) 90 mJ/cm<sup>2</sup>, (f) 110 mJ/cm<sup>2</sup>. (SEM images with magnification of 4000x).

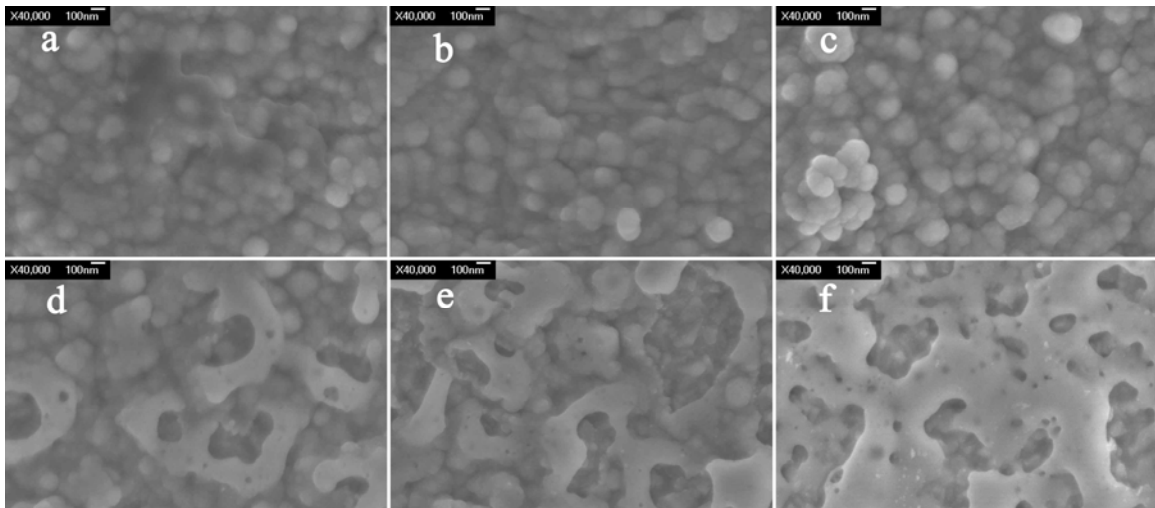


Figure 3-11. Surface morphology of CdS/CIGS films (a) before and after PLA treatment with energy densities at (b) 30 mJ/cm<sup>2</sup>, (c) 50 mJ/cm<sup>2</sup>, (d) 70 mJ/cm<sup>2</sup>, (e) 90 mJ/cm<sup>2</sup>, (f) 110 mJ/cm<sup>2</sup>. (SEM images with magnification of 40000x).

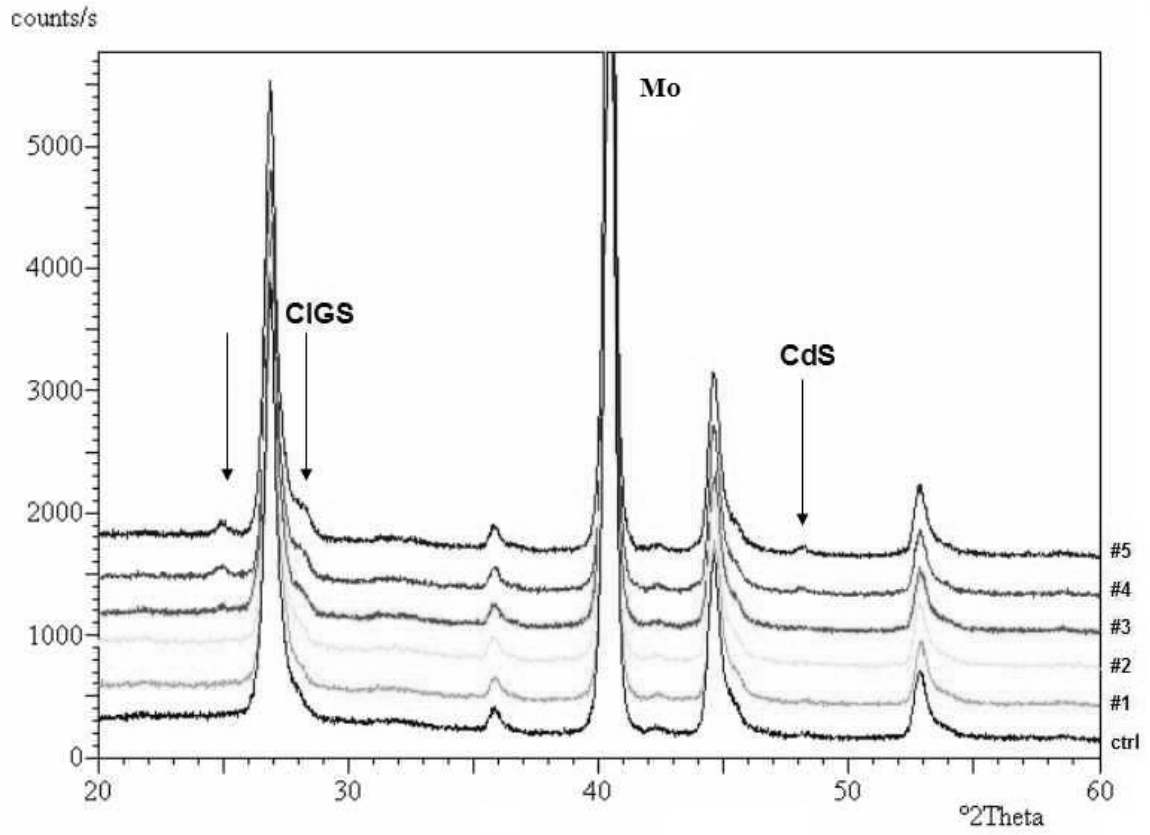


Figure 3-12. Theta-2 theta (symmetrical geometry) diffraction patterns of PLA samples and control sample.

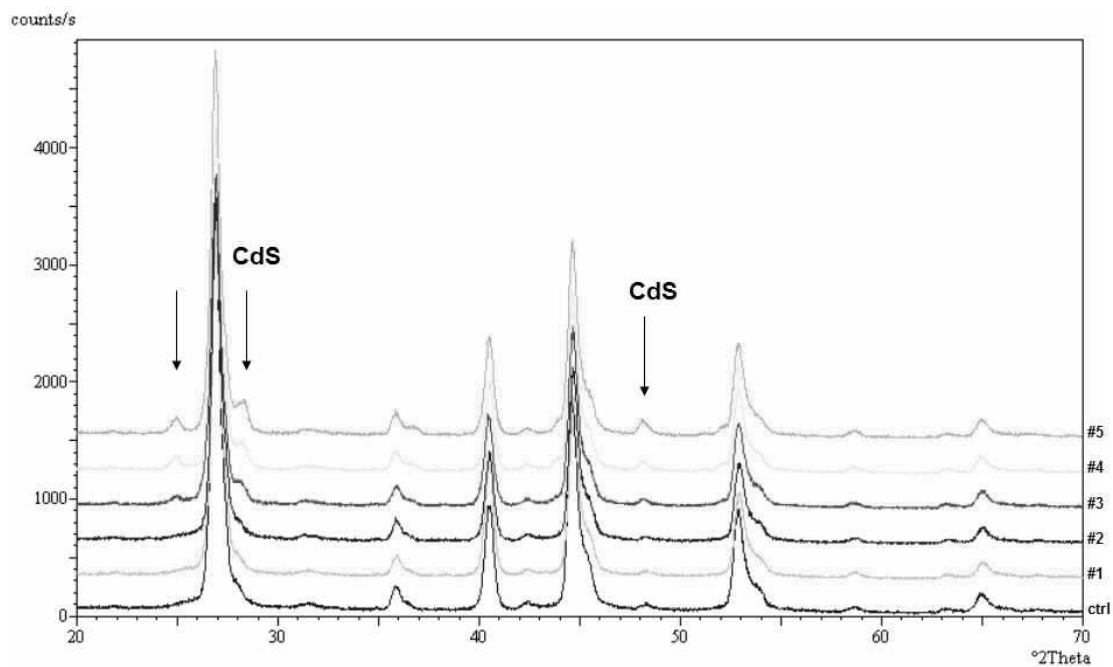


Figure 3-13. Grazing incidence XRD analysis (GIXD) of PLA samples and the control sample ( $\omega=3\text{deg.}$ )

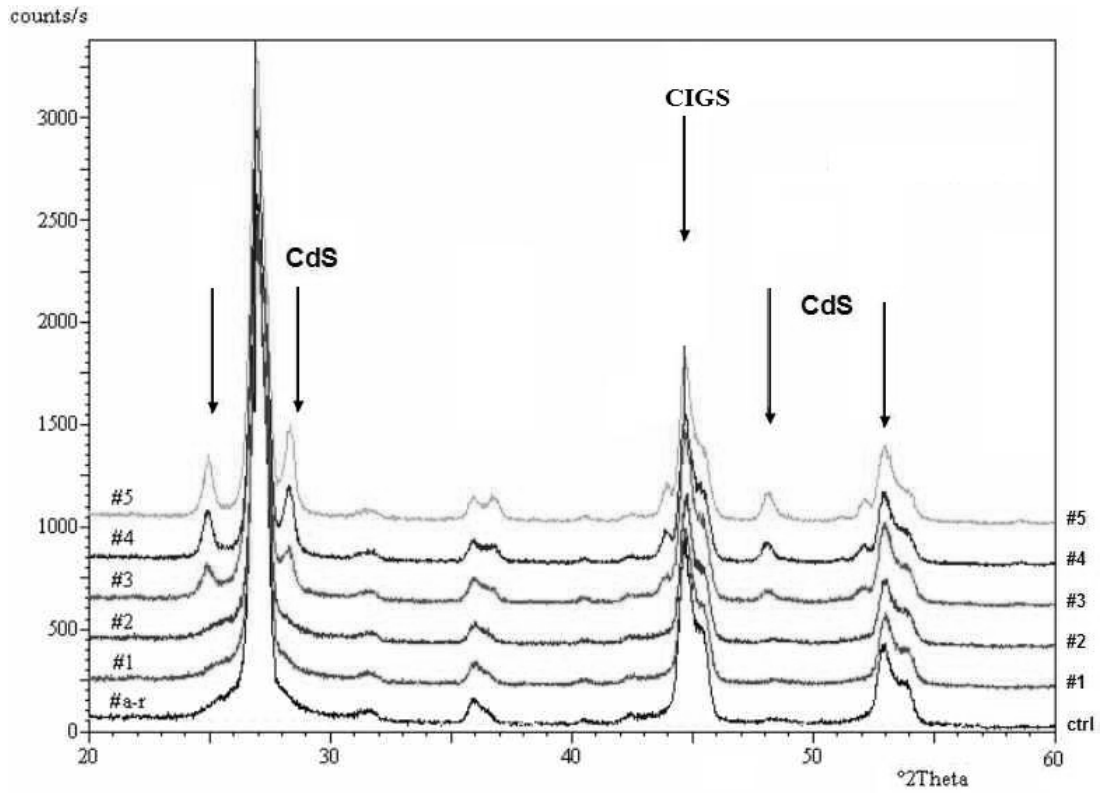


Figure 3-14. Grazing incidence XRD analysis (GIXD) of PLA samples and the control sample ( $\omega=1\text{deg.}$ )

CHAPTER 4  
RAPID THERMAL ANNEALING (RTA) OF FILM PROPERTIES AND DEVICE  
PERFORMANCE FOR CIGS- BASED SOLAR CELLS

Investigation of the halogen-based Rapid Thermal Annealing (RTA) process on CIGS films and solar cells are presented in this chapter. Annealing conditions, RTA procedures and experimental results are well discussed.

**Progressive RTA Treatment on CIGS Solar Cells**

The progressive RTA experiments were performed on one CIGS device, which contains 3 cells (fabricated by NREL), and the results show that progressive RTA treatment (with N<sub>2</sub> ambient) improves cell performance and overall uniformity of large area CIGS solar cells. The RTA procedure is shown in Figure 4-1 and the basic sequence of the progressive RTA is given as follows:

- Prepare a CIGS device
- Test photo- J-V performance before RTA
- Treat device by 100°C - 30 seconds RTA
- Test photo- J-V performance again
- Treat device by 200°C - 30 seconds RTA
- Test photo- J-V performance again.....
- Keep increasing the annealing temperature of each RTA until the cell performance dramatically drops or device is damaged.

From the photo- J-V results (Table 4-1), significant improvement in cell performance was observed in all 3 cells after each progressive RTA treatment at temperatures of 100, 200, and 300°C for 30 seconds. A dramatic increase in the

performance of cell #1 (increase from 9.52 to 15.77%) shows that progressive RTA could be used to enhance the structure uniformity and the performance of large area cells. Since we measured photo- J-V right after each annealing, the light soaking effect might be also a contribution of the performance improvement. For CIGS material photovoltaic modules there are several references reporting the material light induced behavior and the possible reasons (e.g. [39], [40] and [41]). These references all observed the improvement in open circuit voltage ( $V_{oc}$ ) and fill factor (F.F.) because of light soaking and the effect relaxes when kept in dark again. The same effect was observed when keeping the CIGS solar cells in dark with forward bias applied.

We also tried 400°C for 30 seconds; unfortunately the metal grids were severely damaged after the annealing. As a result, no further tests on J-V and Q-E characteristics were performed on these cells.

### **The RTA Effects of Separated CIGS Films**

#### **The XRD and SEM Results**

Five 1x1 inch CIGS samples (from SSI), which were grown on the Mo- coated soda-lime glass (SLG) substrates, were used to investigate the RTA effects under different annealing conditions. XRD, SEM measurements were conducted before and after RTA treatments. The annealing condition (Table 4-2) and results are discussed in the following section.

XRD measurements give information about the preferred film orientation and composition. SEM photos depict the surface morphology and grain size. Results (Figure 4-2 to 4-5) suggest that the overall film composition and surface morphology do not change during the annealing. Only some slightly blurry grain edges were observed in the

SEM images for the 2 samples treated at 350°C (sample #F-R3 and F-R4) as compared to the 300°C RTA treated samples and control sample.

### **Hall-Effect Measurements**

In order to determine the effects of RTA treatment on the carrier concentration, carrier mobility, and sheet resistance of CIGS films, resistivity and Hall- effect measurements were carried out on two CIGS films directly deposited on the SGL substrates before and after the RTA treatments. The annealing conditions and the results of resistivity and Hall- effect measurements (using a MMR Hall- and Van Der Pauw- measurement system) before and after the RTA treatments are summarized in Table 4-3.

The Hall-effect measurements show a significant increase of hole density and a decrease in film resistivity, Hall coefficient, and sheet resistance following the RTA treatment. For sample- #H300-1, which was treated by 300°C RTA, the carrier mobility after RTA was found 2 times larger than the value before annealing, while for sample #H350-1, which was treated by 350°C RTA, the hole mobility was dropped by more than 50% after RTA treatment. The results revealed that 350°C RTA increased the carrier concentration by nearly two orders of magnitude, which also led to the decrease of carrier mobility. The 300°C RTA treated sample showed beneficial results on the film resistivity, carrier mobility and carrier density. Therefore, the peak annealing temperature plays an important role in determining the electrical properties of RTA treated CIGS absorber layers.

### **The RTA Effects of Separated CIGS Solar Cell Devices**

#### **Experimental Details**

Four 1x1 inch CIGS samples (from SSI), which were grown on the Mo- coated soda-lime glass (SLG) substrates were used to investigate the RTA effects under different

annealing conditions. A thin (50 nm) CdS buffer layer was deposited on the CIGS samples using Chemical Bath Deposition (CBD) at 65°C for 13 minutes. A ZnO window layer was then deposited on the CdS/CIGS/Mo/SLG sample by RF sputtering. Subsequent metallization (Ni-Al front contact grids) was carried out by e-beam evaporation through a shadow-mask. Finally, finished devices were produced by cutting the sample into separate cells with 0.429 cm<sup>2</sup> active area and attaching wires with Indium bumps on the Mo-coated glass substrates for back contacts. The performance of these cells was then tested by dark- J-V, photo- J-V and Q-E measurements before and after RTA treatment (with air ambient) under different annealing conditions. To exclude the light soaking effect, the photo- J-V and Q-E re-measurement were conducted two weeks after RTA treatments. The annealing condition (Table 4-4) and results are discussed in the following section.

### **Photo- J-V Performance**

From the photo- J-V results (Table 4-5), for the cell D-R1, D-R2 and D-R3, we found that  $V_{oc}$ ,  $J_{sc}$  and conversion efficiency increased and F.F. decreased after RTA treatments. For cell D-R4 which was annealed at 350°C, 2 min, only  $J_{sc}$  increased after RTA and the overall performance dropped. By taking a close look at the F.F. data, we found that for the cell treated by 2 min, the F.F. dropped more than that of the cell treated by 1 min RTA at the same temperature. This suggests that 1 min is enough for the RTA treatment and too long holding time can cause performance drops.

### **Dark- J-V Characteristics**

To find the reason of Fill Factor loss during the RTA, the dark- J-V measurements were conducted of these the tested devices before and after RTA treatments. From the measured dark- J-V curves (Figure 4-6 to 4-9), we found the overall dark current density

decreased in forward bias region while it increased in reverse bias region after RTA treatment except cell D-R1 has increased dark- J-V when applied voltage below 0.38 V after RTA treatment, and the shapes of all J-V curves after RTA have a trend to become linear, which suggest the resistivity decrease during the RTA and the Fill factor loss. One possible reason is the metal contact on the top of the devices diffused down through the whole device during the annealing and increased the conductivity, made the whole device become more like a conductor rather than a semiconductor. Some other tested cells even showed pure linear J-V curve and zero F.F, which is caused by metal spiking effects. Several recent studies already showed that the spiking effect is more likely to occur during the RTA for the E-beam evaporated Al metal grids than sputtered metal contacts. Another possible reason is because of the low melting point of In ( $156.61^{\circ}\text{C}$ ). Indium diffusion from the back contact might also cause the decrease of F.F. during the RTA treatment. The results suggest that RTA treatment is more suitable for devices with sputtered metal contacts or applying RTA treatments before metal grids and contacts deposition.

From the semi-log plots of the dark- J-V curves (Figure 4-10 to 4-13), cell # D-R1 has deteriorated diode quality factor after the RTA treatment while other cells remain same diode qualities. Though the photo- J-V results of cell # D-R1 is very promising after RTA, the relationship between RTA condition and the afterward dark- J-V result is still unclear for cell # D-R1.

### **The S-R and Q-E Performance**

From the measured Q-E curves (Figure 4-14 to 4-17), improvements on Q-E were observed on entire interested wavelengths after RTA treatments, which suggest that RTA has positive effect on all layers (absorber layer, buffer layer, and window layer) of CIGS

solar cells. These results are consistent with the photo- J-V results shown before; even for cell D-R4 which has overall decreased photo- J-V performance after RTA, the Q-E still showed that photo current density for the interested wavelength region increase after RTA treatment which evidently proved the  $J_{sc}$  improvement of such cell.

### **Thermal Annealing on CIGS Solar Cells by High Temperature XRD System**

Because of the limitation on the minimum temperature of the RTA system, a high temperature XRD system was used to anneal 2 CIGS solar cells at temperature 100°C and 150°C, 30 seconds. The Photo- and Dark- J-V measurements were taken before and after annealing. Dark- J-V curves did not show much difference before and after low temperature RTA treatments. From the photo- J-V results (Table 4-6 and Figure 4-18), the overall performance for tested cells has been improved after low temperature RTA, furthermore. The cell treated by 150°C RTA has more significant improvement on all IV parameters while the cell treated by 100°C RTA only has improvement on F.F. and  $\eta$ . Combined with the previous results (progressive RTA results) shown before, these data suggest that the optimal RTA temperature for CIGS solar cells is in the range of 200°C to 300°C.

### **Summary**

Progressive RTA treatments have shown significant improvement of the overall uniformity and performance of large area CIGS solar cells. Under low RTA temperature, the surface composition and morphology remain unchanged. Our study of the RTA effect on CIGS devices shows increase in the values of  $V_{oc}$ ,  $J_{sc}$ , and conversion efficiency, but some decrease in fill factor (F.F.). The estimated optimal annealing temperatures should be between 200 and 300°C with 1- minute or less holding time.

Table 4-1. Photo- J-V results of CIGS solar cells before and after progressive RTA

Pre-annealing	Cell #1	Cell #2	Cell #3	After 100°C RTA	Cell #1	Cell #2	Cell #3
Voc (V)	0.628	0.652	0.655	Voc (V)	0.633	0.656	0.660
Jsc (mA/cm <sup>2</sup> )	31.66	32.97	33.50	Jsc (mA/cm <sup>2</sup> )	34.30	35.47	34.05
F.F. (%)	47.88	68.52	70.71	F.F. (%)	56.81	71.10	73.03
Eff. (%)	9.52	14.73	15.51	Eff. (%)	12.32	16.55	16.19
After 200°C RTA	Cell #1	Cell #2	Cell #3	After 300°C RTA	Cell #1	Cell #2	Cell #3
Voc (V)	0.652	0.657	0.650	Voc (V)	0.627	0.623	0.630
Jsc (mA/cm <sup>2</sup> )	34.85	35.11	32.34	Jsc (mA/cm <sup>2</sup> )	35.39	36.35	35.08
F.F. (%)	68.43	72.14	76.15	F.F. (%)	71.05	70.48	74.32
Eff. (%)	15.55	16.65	16.01	Eff. (%)	15.77	15.96	16.42

Table 4-2. CIGS film number and the annealing conditions

Sample #	RTA temperature	Holding time	note
F-R1	<i>300°C</i>	<i>1 minute</i>	<i>RTA sample</i>
F-R2	<i>300°C</i>	<i>2 minutes</i>	<i>RTA sample</i>
F-R3	<i>350°C</i>	<i>1 minute</i>	<i>RTA sample</i>
F-R4	<i>350°C</i>	<i>2 minutes</i>	<i>RTA sample</i>
F-Ctrl	<i>N/A</i>	<i>N/A</i>	<i>Control sample</i>

Table 4-3. Hall-effect data of NREL CIGS samples before and after RTA treatments

	Sample #H300-1	Sample #H350-1
RTA condition	<i>300°C, 1-min</i>	<i>350°C, 1-min</i>
Ambient	<i>Ar</i>	<i>Ar</i>
Resistivity (ohm-cm)*	<i>70.58 / 4.21</i>	<i>55.76 / 2.17</i>
Mobility (cm <sup>2</sup> /Vs)*	<i>2.80 / 6.77</i>	<i>4.28 / 1.86</i>
Hole density (cm <sup>-3</sup> )*	<i>3.16×10<sup>16</sup> / 2.19×10<sup>17</sup></i>	<i>2.62×10<sup>16</sup> / 1.55×10<sup>18</sup></i>
Hall coefficient (cm <sup>3</sup> /Coul)*	<i>197.77 / 28.48</i>	<i>238.53 / 4.03</i>
Sheet resistance (ohm/cm <sup>2</sup> )*	<i>470536.4 / 28044.4</i>	<i>371761.8 / 14435.8</i>
Carrier type	<i>holes / holes</i>	<i>holes / holes</i>

\*Data taken before/after RTA treatments

Table 4-4. Annealing conditions of RTA treated CIGS devices

Sample #	RTA Temperature	Holding Time	note
D-R1	$300^{\circ}\text{C}$	<i>1 minute</i>	<i>RTA device</i>
D-R2	$300^{\circ}\text{C}$	<i>2 minutes</i>	<i>RTA device</i>
D-R3	$350^{\circ}\text{C}$	<i>1 minute</i>	<i>RTA device</i>
D-R4	$350^{\circ}\text{C}$	<i>2 minutes</i>	<i>RTA device</i>

Table 4-5. Photo- J-V results of separated CIGS solar cells before and after RTA

Cell #	D-R1	D-R2	D-R3	D-R4
RTA condition	<i>300°C, 1-min</i>	<i>300°C, 2-min</i>	<i>350°C, 1-min</i>	<i>350°C, 2-min</i>
Voc (V)*	<i>0.455 / 0.471</i>	<i>0.471 / 0.487</i>	<i>0.465 / 0.471</i>	<i>0.465 / 0.422</i>
Jsc (mA/cm <sup>2</sup> )*	<i>27.49 / 31.43</i>	<i>26.55 / 30.51</i>	<i>28.75 / 33.94</i>	<i>27.67 / 30.41</i>
F.F. (%)*	<i>52.69 / 49.01</i>	<i>57.48 / 49.96</i>	<i>52.14 / 48.58</i>	<i>48.00 / 39.36</i>
Eff. (%)*	<i>6.591 / 7.259</i>	<i>7.196 / 7.422</i>	<i>6.975 / 7.759</i>	<i>6.177 / 5.051</i>

\* Data taken before/after RTA treatments

Table 4-6. Photo- J-V results of CIGS solar cells before and after RTA by using high temperature XRD system

Device#	RTA	Voc (V)*	Jsc (mA/cm <sup>2</sup> )*	FF (%)	Eff (%)*
1	100°C, 30s	0.50/0.503	24.74 / 24.68	61.45 / 67.60	8.19 / 8.35
2	150°C, 30s	0.43/0.509	25.56 / 28.85	45.91 / 51.9	5.03 / 7.62

\* Data taken before/after RTA treatments

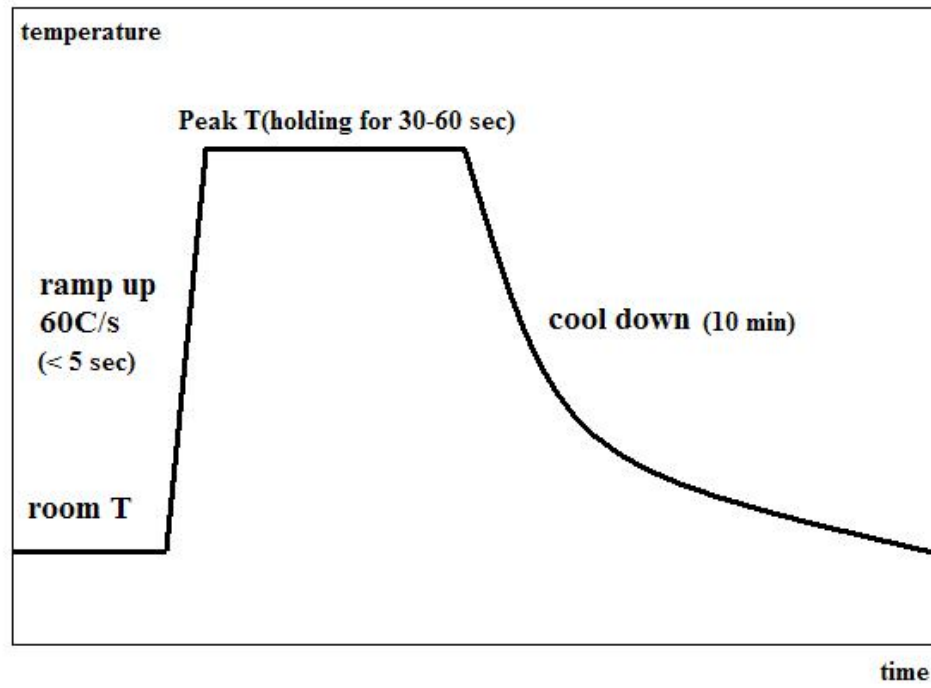


Figure 4-1. Cycle time for Rapid Thermal Annealing (one run).

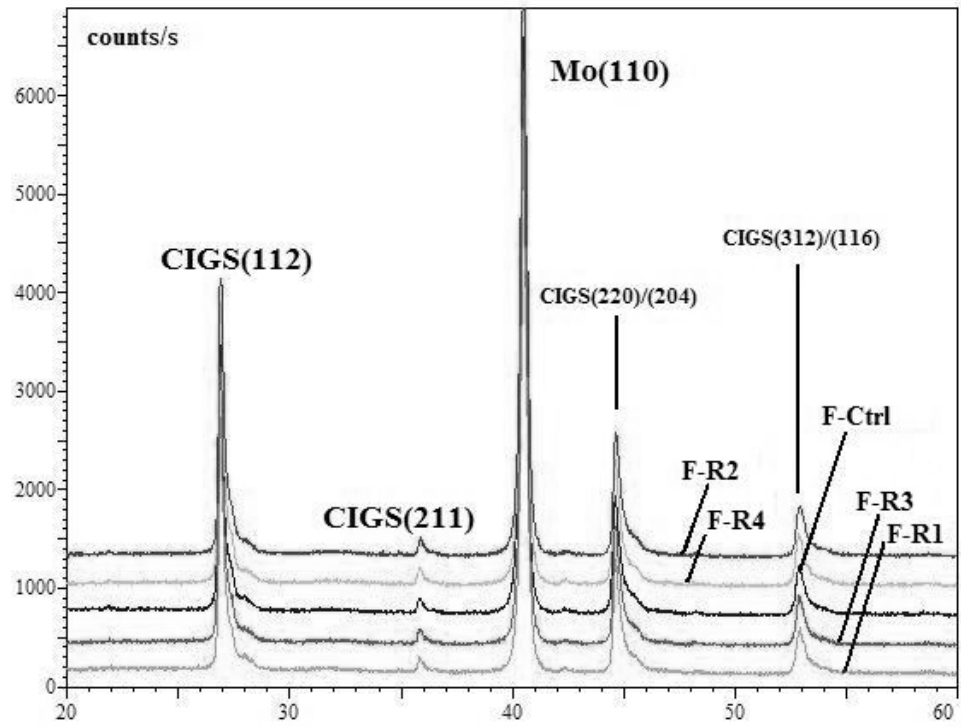


Figure 4-2. XRD results of RTA treated CIGS films and the control sample.

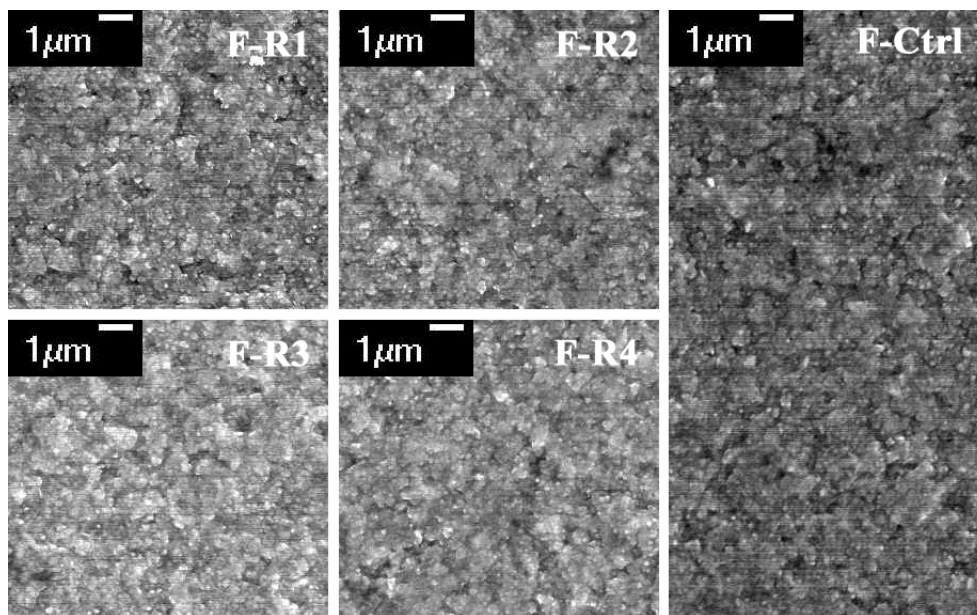


Figure 4-3. Surface morphology of RTA treated CIGS films and the control sample. (SEM images with magnification of 3000x).

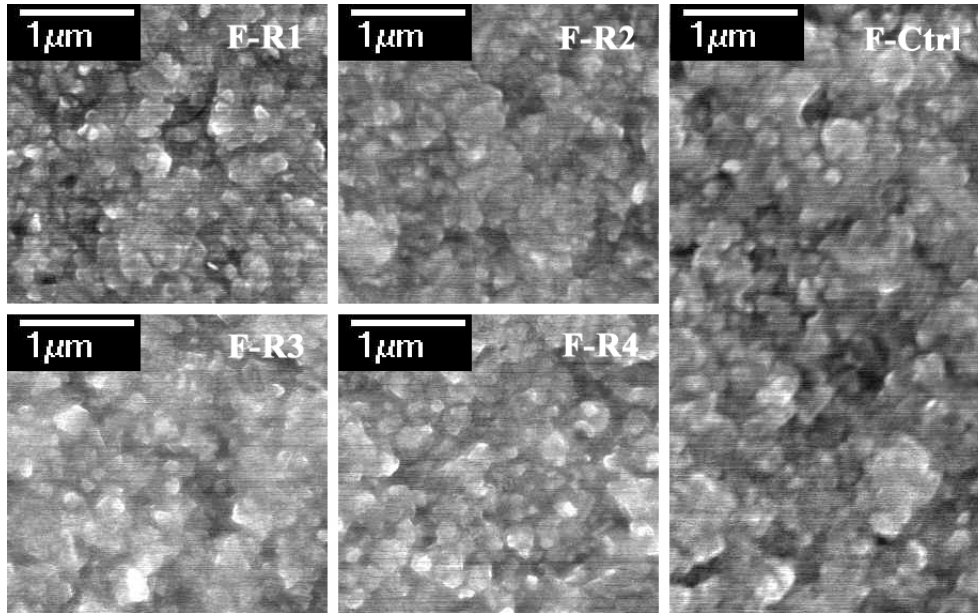


Figure 4-4. Surface morphology of RTA treated CIGS films and the control sample. (SEM images with magnification of 10000x).

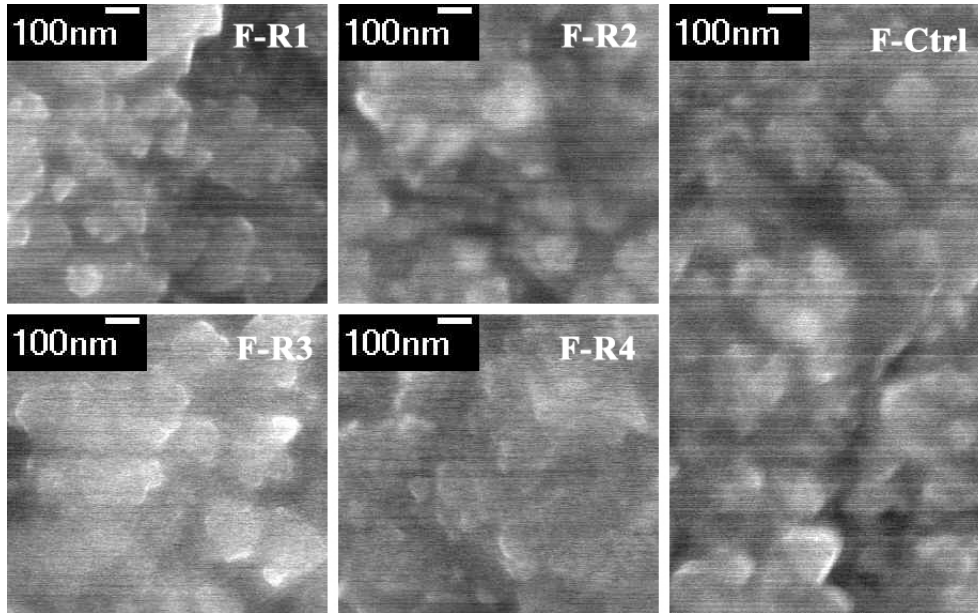


Figure 4-5. Surface morphology of RTA treated CIGS films and the control sample. (SEM images with magnification of 30000x).

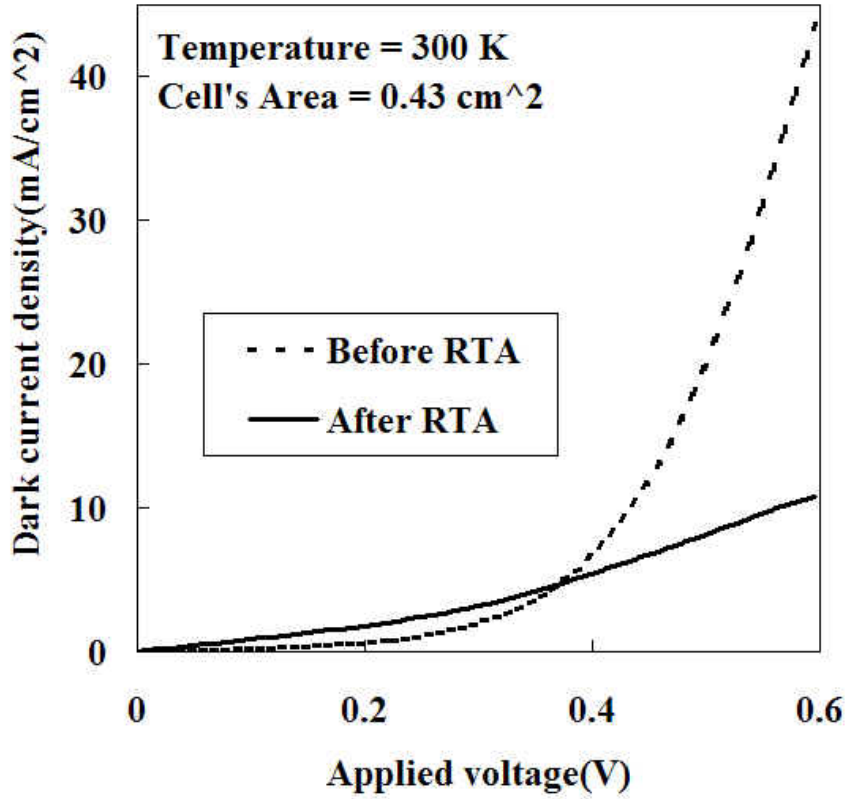


Figure 4-6. Dark- J-V curves of tested CIGS solar cell (#D-R1) before and after RTA (300°C, 1-min) treatment.

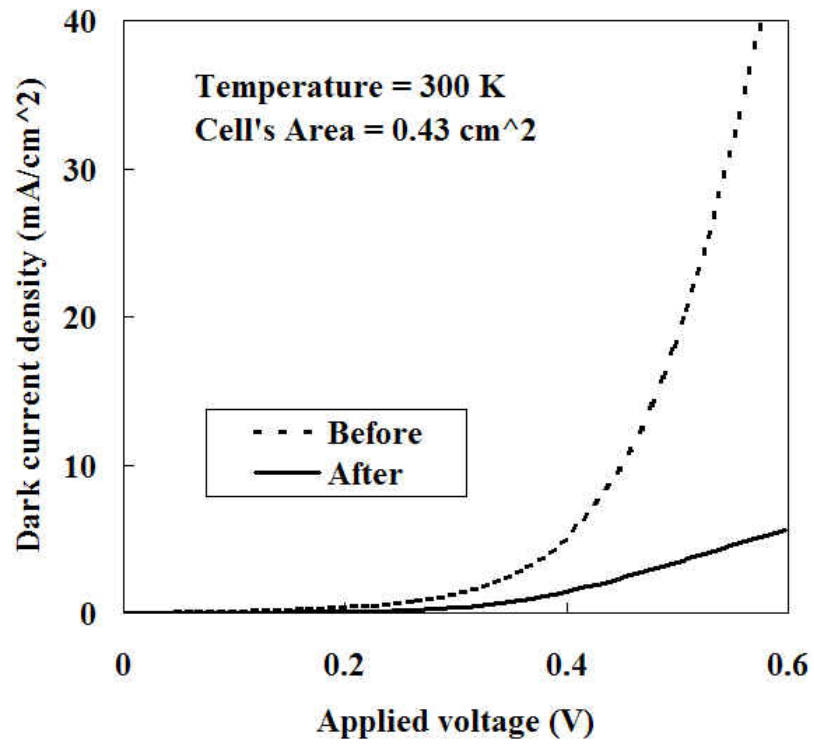


Figure 4-7. Dark- J-V curves of tested CIGS solar cell (#D-R2) before and after RTA (300°C, 2-min) treatment.

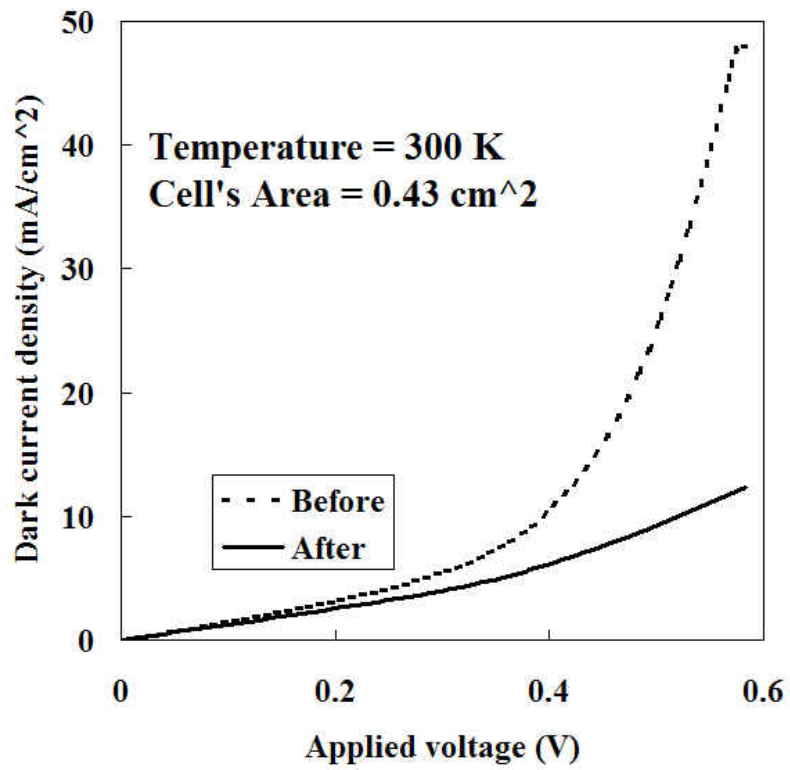


Figure 4-8. Dark- J-V curves of tested CIGS solar cell (#D-R3) before and after RTA (350°C, 1-min) treatment.

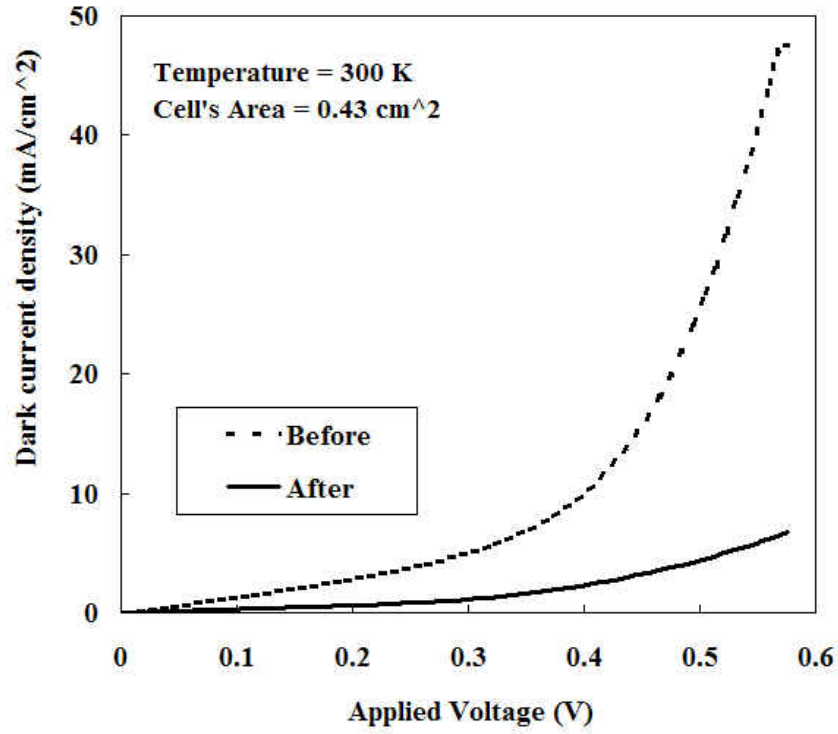


Figure 4-9. Dark- J-V curves of tested CIGS solar cell (#D-R4) before and after RTA (350°C, 2-min) treatment.

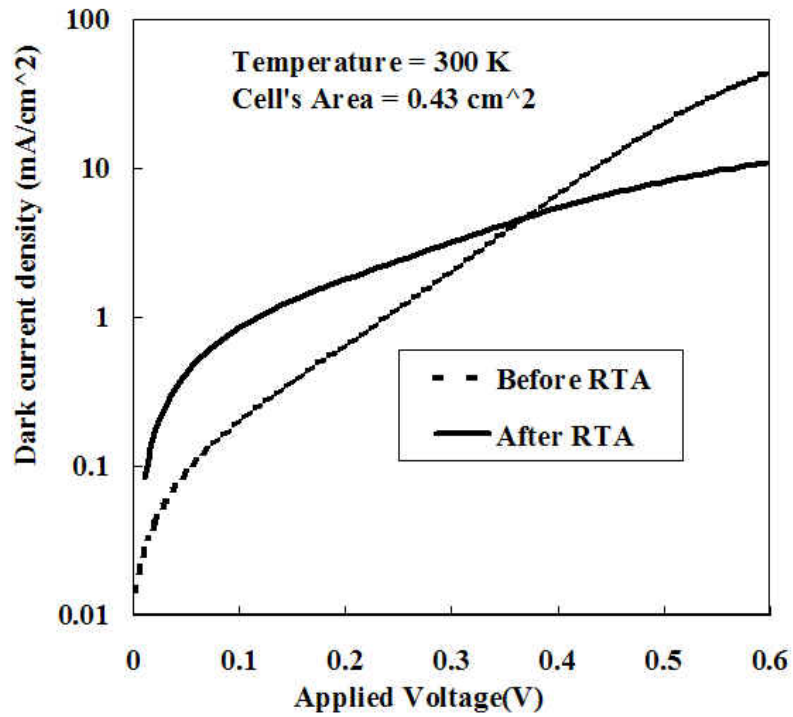


Figure 4-10. Dark- J-V curves (semi-log plot) of tested CIGS solar cell (#D-R1) before and after RTA (300°C, 1-min) treatment.

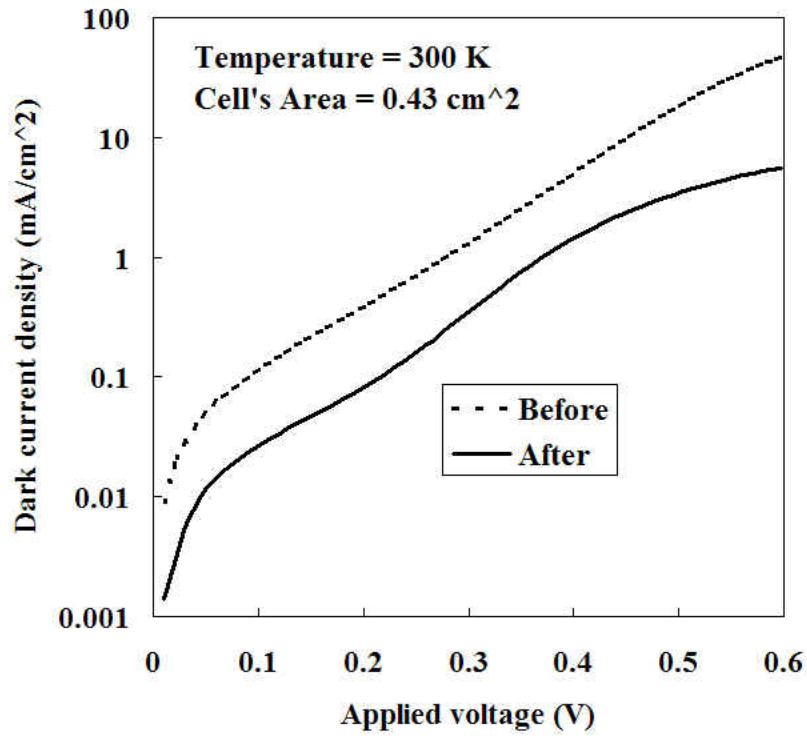


Figure 4-11. Dark- J-V curves (semi-log plot) of tested CIGS solar cell (#D-R2) before and after RTA (300°C, 2-min) treatment.

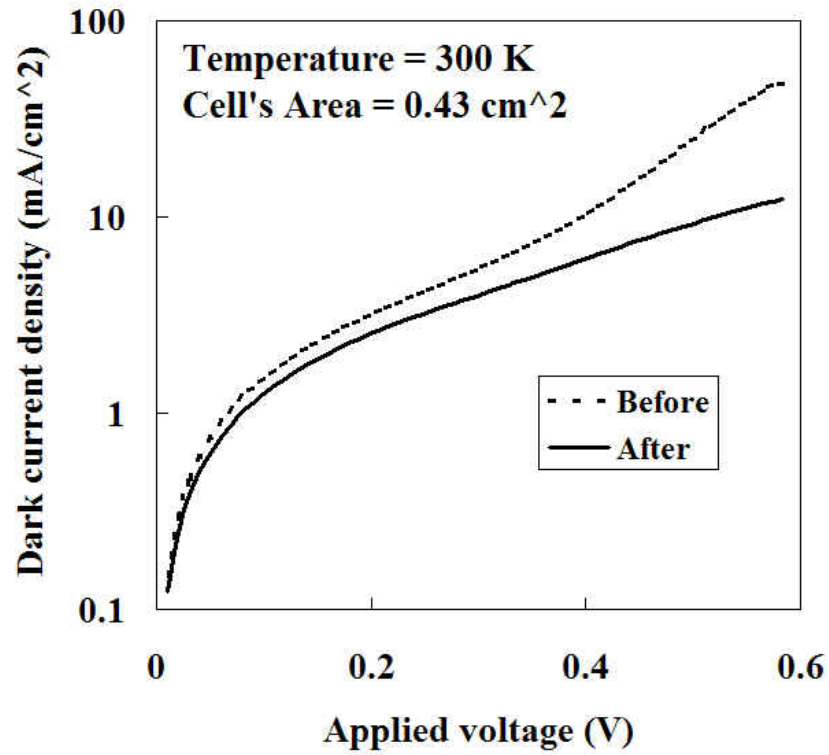


Figure 4-12. Dark- J-V curves (semi-log plot) of tested CIGS solar cell (#D-R3) before and after RTA (350°C, 1-min) treatment.

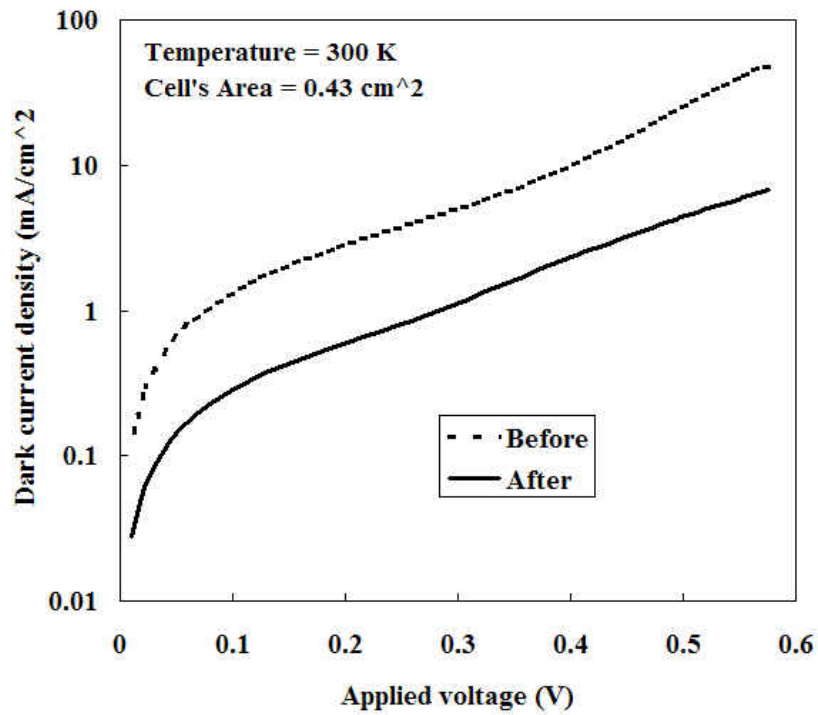


Figure 4-13. Dark- J-V curves (semi-log plot) of tested CIGS solar cell (#D-R4) before and after RTA (350°C, 2-min) treatment.

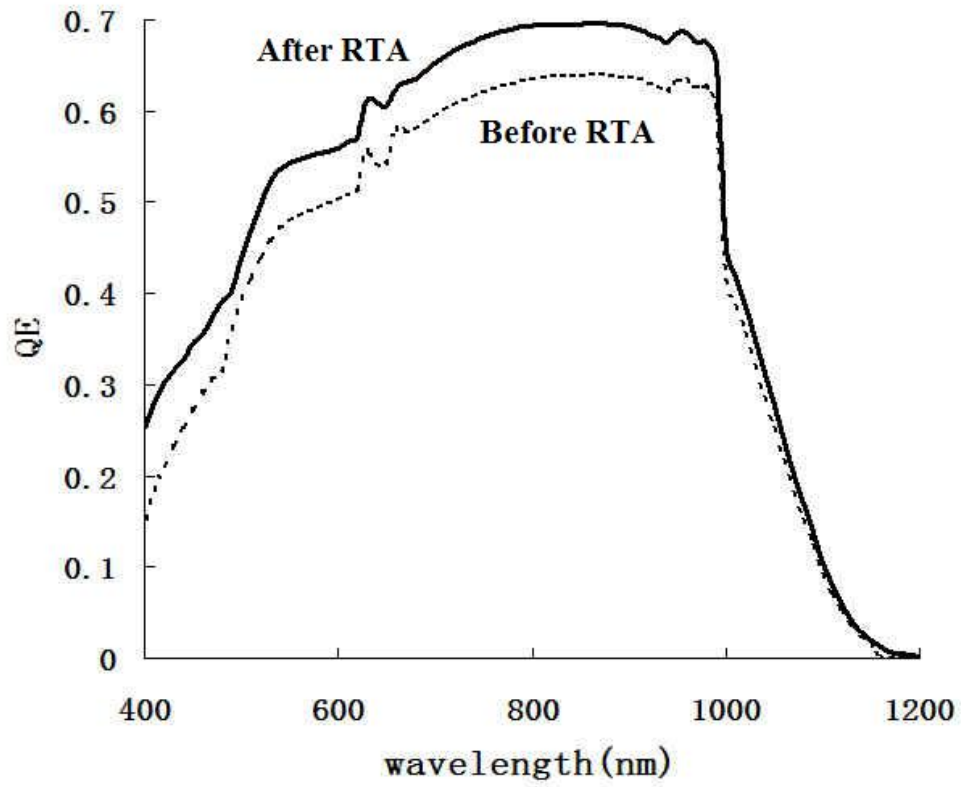


Figure 4-14. Quantum efficiency (Q-E) versus wavelength of tested CIGS solar cell (#D-R1) before and after RTA (300°C, 1-min).

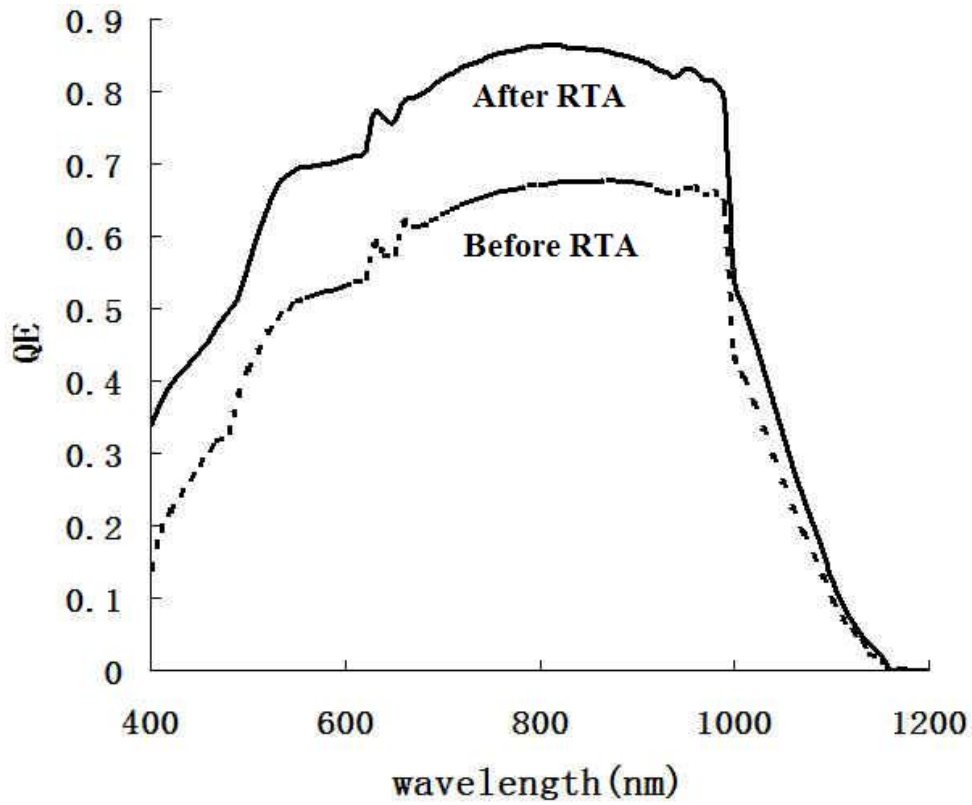


Figure 4-15. Quantum efficiency (Q-E) versus wavelength of tested CIGS solar cell (#D-R2) before and after RTA (300°C, 2-min).

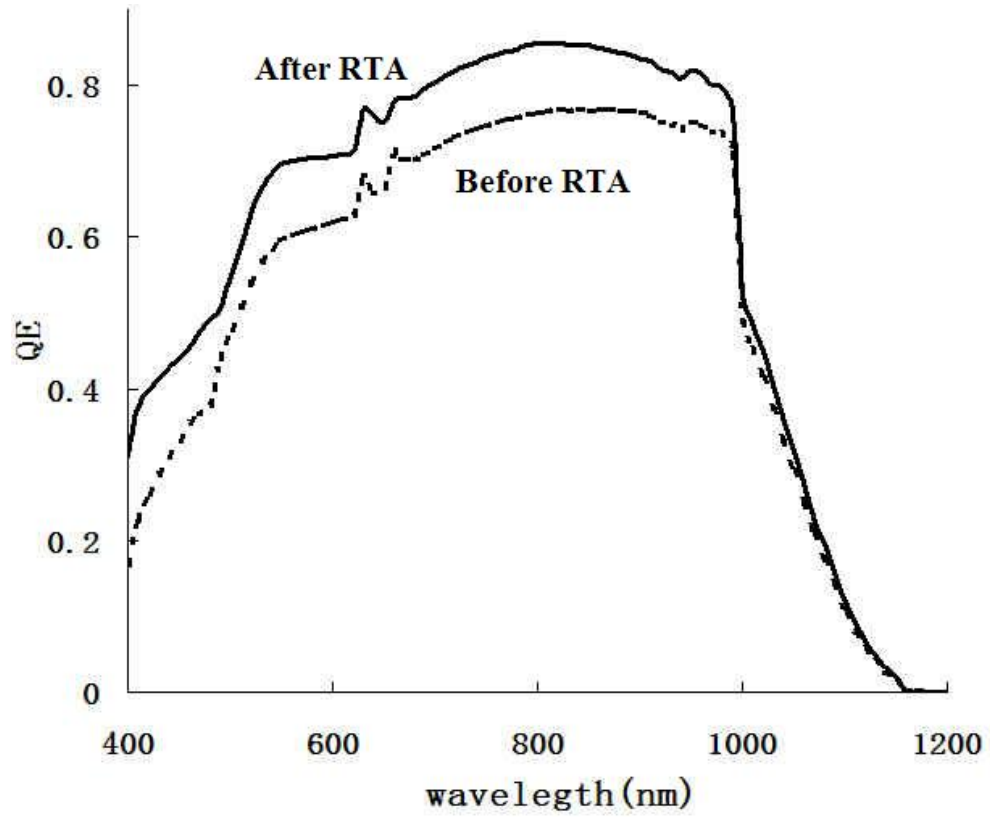


Figure 4-16. Quantum efficiency (Q-E) versus wavelength of tested CIGS solar cell (#D-R3) before and after RTA (350°C, 1-min).

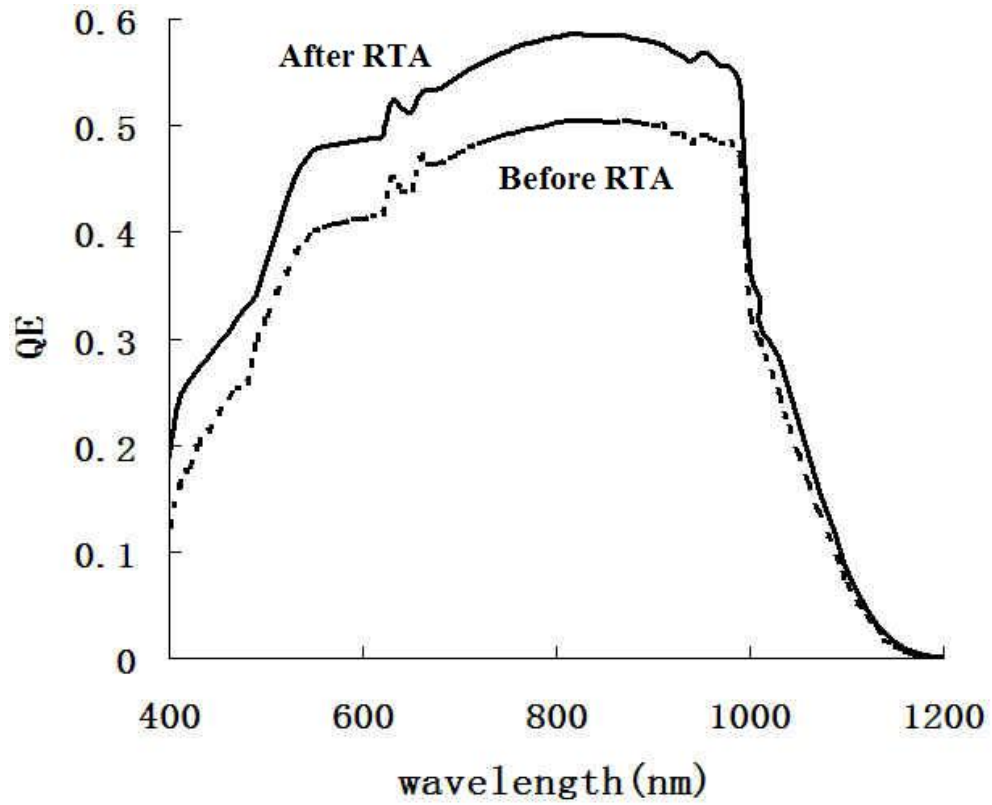
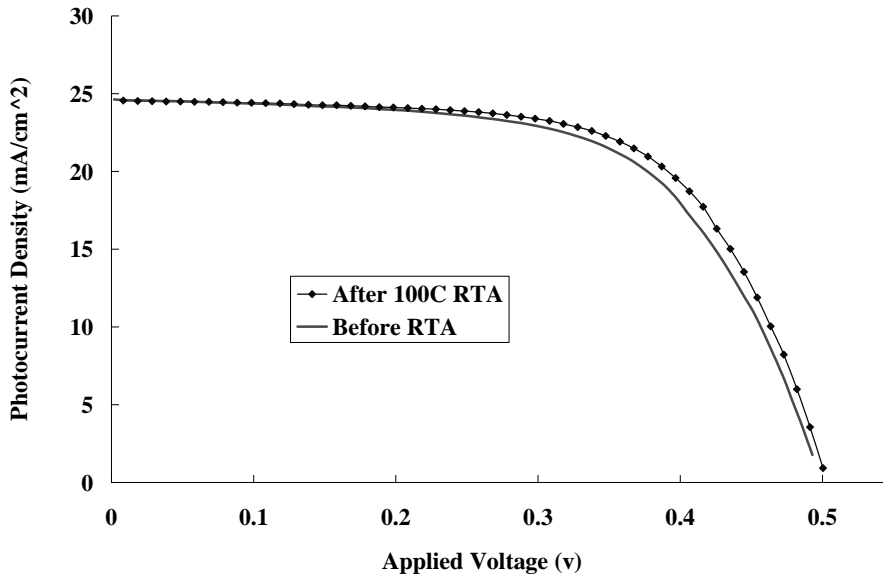
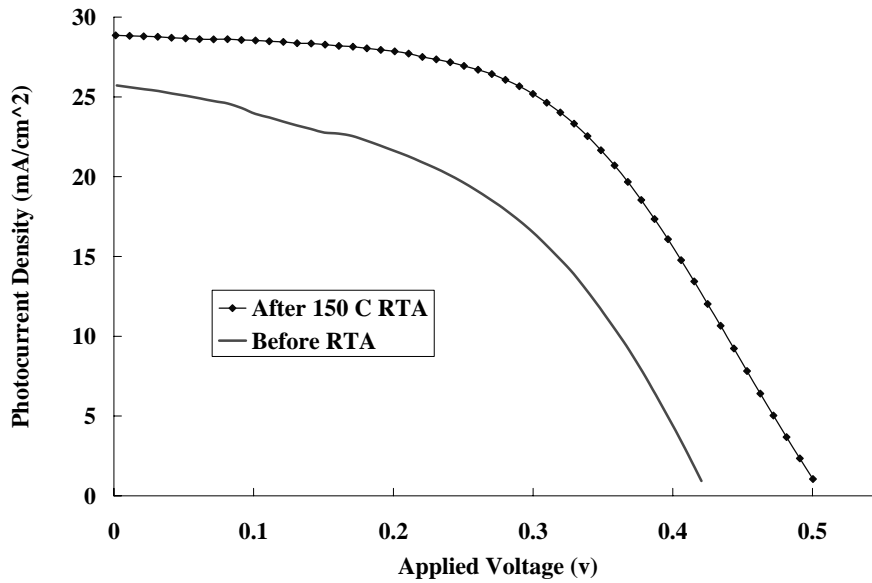


Figure 4-17. Quantum efficiency (Q-E) versus wavelength of tested CIGS solar cell (#D-R4) before and after RTA (350°C, 2-min).



(a)



(b)

Figure 4-18. Photo- J-V curves of tested CIGS solar cells before and after (a) 100°C, 30 seconds and (b) 150°C, 30 seconds RTA treatments by using high temperature XRD system.

## CHAPTER 5 FABRICATION PROCESS OF CIGS SOLAR CELLS

In this chapter description of the CIGS solar cell device structure and typical fabrication process are given in detail. Based on the typical device structure and fabrication process of CIGS based thin-film solar cell (Figure 5-1), the first two steps comprise the deposition of a 1~2  $\mu\text{m}$  Mo back contact on top of a thin chemical barrier ( $\text{SiO}_2$ ) on a glass substrate. This can be accomplished by two-step magnetron sputtering in an in-line PVD system. Next, a CIGS absorber layer with thickness of 1.5~2  $\mu\text{m}$  is deposited by using PVD, sputtering, PMEE, co-evaporation or RTP technique. Followed by deposition of a 500  $\text{\AA}$  thin CdS buffer layer (forming the hetero-junction with CIGS) using chemical bath deposition (CBD). An intrinsic ZnO of 500~1000  $\text{\AA}$  and a conducting ZnO:Al (0.3 to 0.5  $\mu\text{m}$ ) TCO layers are then deposited by the sputtering system. Finally a 500  $\text{\AA}$  Ni and a 3  $\mu\text{m}$  Al- metal contacts are deposited by using E-Beam evaporation technique. For finished device, an Anti-reflection (AR) coating (e.g.,  $\text{MgF}_2$ ) was used on the top of the cell to minimize the reflection loss.

### **Substrate**

The most widely used substrate for the fabrication of CIGS based solar cells is the soda-lime glass (SLG), which allowed champion efficiencies of up to 19.2% AM1.5G (Ramanathan et al., 2003). This low-cost SLG substrate material can be produced in large scale and with reproducible quality mainly for the window industry. The most commonly used back contact is the sputtered Mo- metal layer of approximately 1  $\mu\text{m}$  thickness. The following are the requirements for an excellent CIGS substrate.

- Vacuum compatibility. The substrate should not degas during the various vacuum deposition steps, especially during CIGS absorber layer deposition, when the substrate must be heated.
- Thermal stability. For the deposition of high performance CIGS absorbers, the substrate temperature should reach 500-600°C during part of the deposition process. Substrate temperatures of less than 350°C usually lead to severely degraded absorber layer quality and poor cell performance. Therefore, substrates should withstand the temperature no less than 350°C.
- Proper thermal expansion. The coefficient of thermal expansion (CTE) of the substrate should be compatible with that of CIGS; otherwise CIGS adhesion problems may be occurred. Also cracking of the Mo back contact can be encountered because of its low CTE.
- Chemical inactivity. The substrate should not corrode, neither during processing nor during use. In particular, it should not react with Se during the CIGS deposition or decompose during aqueous solution deposition of buffer layer (CdS). A good substrate should also not release any impurities that can diffuse into the absorber, except when the diffusion is desired.
- Sufficient humidity barrier. The substrate could protect the active solar cells layers during the long-term usage against environmental attack from the back such as the penetration of water vapor.
- Surface smoothness. A smooth substrate surface is essential. First, abrupt changes in the surface such as spikes or cavities may lead to shunts between the front and the back contact. Second, the deposition of impurity diffusion barriers or insulation layers may be easier and more successful on a smooth substrate.
- Cost, energy consumption, availability and weight. An excellent substrate should be cheap, little energy consumption, consists of available and abundant materials, and with light weight.

Because of the above requirements and demands of CIGS substrates, the SLG is the preferred substrate material for the industrial manufacturing of CIGS based solar cells since it fulfils most of these requirements. Recent results from ISET show CIGS solar cells formed on SLG substrates with higher conversion efficiency than those with other alternative substrates (Table 5-1). Additionally, the incorporation of sodium has a beneficial effect on the CIGS film quality. However, the main disadvantages of glass

substrates are their high brittleness and non-flexibility, which limit the applications considerably.

### **Back Contact Layer**

The molybdenum (Mo) layers with a thickness of around 1  $\mu\text{m}$  deposited by d.c.-magnetron sputtering process are used in the bottom contact layers for the CIGS-based solar cells. With the excellent properties of low contact resistance to the CIGS, relative stability at the processing temperatures (400-600  $^{\circ}\text{C}$ ), and resistance to reacting with Cu, In, and Ga, the Mo is the most widely used metal for the back contacts of CIGS-based solar cells.

Followed the deposition of CIGS absorber layer on the Mo-coated glass substrates, an interfacial  $\text{MoSe}_2$  layer between the CIGS absorbers and the Mo layers has been identified. This layer structure of  $\text{MoSe}_2$  was suggested to have a bandgap energy of about 1.4eV with a thickness of around 0.1  $\mu\text{m}$ . Besides that the wide-band-gap  $\text{MoSe}_2$  layer can be served as the back surface field in the CIGS-based solar cells to enhance the carrier collection, the  $\text{MoSe}_2$  layers are considered to improve the adhesion of CIGS films to the Mo contacts to form good ohmic contacts.

### **CIGS Absorber Layer**

The  $\text{Cu}(\text{In,Ga})\text{Se}_2$  compound belongs to the semiconducting I-III-VI<sub>2</sub> materials family that crystallize in the tetragonal chalcopyrite structure. Chalcopyrite is another name for copper iron sulfide ( $\text{CuFeS}_2$ ), a common copper ore, which gave name to these materials. An interesting property of the semiconducting chalcopyrites in general and  $\text{Cu}(\text{In,Ga})\text{Se}_2$  in particular is that bandgap energy,  $E_g$ , can be varied, for instance by varying the amount of Ga. The optimal bandgap for a solar cell with respect to the solar

spectrum is around 1.4 eV [42]. The bandgap of CuInSe<sub>2</sub> (CIS) is 1.04 eV and 1.68 eV for CuGaSe<sub>2</sub> (CGS) while the bandgap of the alloys Cu(In,Ga)Se<sub>2</sub> lies in between. A Ga/(In+Ga) ratio of 30% results in E<sub>g</sub> of around 1.3 eV, which has been shown empirically to give the best device performance. Another way to increase E<sub>g</sub> is by replacing part of the Se for S to form Cu(In,Ga)(Se,S)<sub>2</sub>. It is expected that a wider E<sub>g</sub> would yield a higher V<sub>oc</sub>. At a given efficiency higher voltage and lower current is preferred, since lower current results in smaller resistive losses with  $P = I^2R$ . In a module with several interconnected cells an increased voltage is of interest. Since a higher voltage corresponds to a lower current for the same power, a superior design of wider cells with smaller geometrical losses is preferred.

CIGS thin-films are grown by the sequential evaporation of metals in the presence of Se. The vacuum base pressure is in the 6-10<sup>-7</sup>-torr range. To help the reader better understand the growth of the CIGS thin-films, we describe first the integrated deposition scheme. Figure 5-2 shows a schematic profile of the elemental fluxes and substrate temperature used for the deposition of the CIGS films [43]. The process consists of three stages: (1) the formation of an (In,Ga)<sub>2</sub>Se layer on the soda-lime glass (SLG)/Mo substrate at a substrate temperature of 400°C; followed by (2) the deposition of Cu and Se at a substrate temperature of ~570°C, at which the compound formation and crystallization of Cu (In,Ga)<sub>2</sub>Se takes place such that the composition is slightly Cu-rich; and (3) additional In, Ga and Se is added at the same substrate temperature of 570°C, so that the final composition expected is Cu-poor. The sample is cooled down to approximately 400°C in the presence of Se, after which the system is allowed to cool down naturally to room temperature. CIGS solar cells were usually completed by

chemical-bath deposition (CBD) of approximately 500 Å CdS, followed by RF sputtering of 500 Å of intrinsic ZnO and 2000 Å of Al-doped ZnO. Ni/Al grid contacts were applied with approximately 5% coverage. The substrate was SLG coated with Mo film sputtered using a DC magnetron cathode.

### **Chemical Bath Deposition (CBD) of CdS Buffer Layer**

The technique of CBD involves the controlled precipitation from solution of a compound on a suitable substrate. The CBD technique offers several advantages over the CVD, MBE and spray pyrolysis methods. In the CBD process, the film thickness and deposition rate can be controlled by varying the solution pH, temperature, and reagent concentration, and it is capable to coat large areas in a reproducible and low cost way. In addition, the homogeneity and stoichiometry of the deposited films are partially maintained. The CBD process was first reported by J. E. Reynolds in 1884 for the deposition of PbS films. Since then a wide range of chalcogenide (e.g. CdS, ZnS and MnS) and chalcopyrite materials (e.g. CuInS<sub>2</sub> and CuInSe<sub>2</sub>) have been prepared by the CBD method.

Recently, there has been considerable interest for developing new polycrystalline thin-film semiconductors using various techniques. Among them, the CBD process has found very attractive for being a low temperature and low cost process. The CBD technique is a useful method for the deposition of thin-film semiconductor materials. Many of them form important components within polycrystalline solar cells. Such devices may offer advantages in low cost solar energy conversion. The CBD process has advantages over alternative methods of thin-film deposition: The technique is simple and requires relatively low capital expenditure; films may be deposited at very low temperatures on a wide variety of substrates. The CBD process may be easily adapted to

large area processing at low fabrication cost, and the thickness of the deposited layers may be controlled by varying the length of the deposition time. A major drawback of the CBD process is the inefficiency of the process in terms of the utilization of starting materials and their conversion to thin-films. The competing homogeneous reaction in the solution, which results in massive precipitation in solution and deposition of materials on the CBD reactor walls, limits the extent of the heterogeneous reaction on the substrate surface.

There are several methods for depositing thin-film CdS: vacuum evaporation, chemical vapor deposition, and spray pyrolysis. However, the most convenient method for low cost growth is the CBD process. The CBD technique is a simple solution growth process for creating polycrystalline CdS thin-films. This involves dipping a substrate into a reaction mixture for a time depending on the film thickness required. It is well known that the structures and properties of CdS films are influenced by the recipe used in the growth. Composition, grain size, crystallinity, photosensitivity, defect density, and the covering ability have all related to the bath composition, temperature, and duration of the deposition.

In the deposition of solid thin-films in a chemical bath by the CBD process the nucleation centers are regularly formed by the absorption of metal hydroxo species on the surface of the substrate. The initial layer of the thin-film is formed through the replacement of hydroxo group by the sulphide ions, and subsequently the solid film is grown by the condensation of metal and sulfide ions onto the top of the initial layer. Two competing processes, the heterogeneous process of the solid film deposited on the substrate and the homogeneous process of precipitation in the reaction bath are taking

place simultaneously in the chemical bath during the CBD process. In order to remove the possible precipitation, which may be attached on the surface of the films, the substrates are rinsed with DI water after the deposition and blown dry with nitrogen gas. The CBD process set-up (Figure 5-3) is very simple and makes it very convenient for thin film CdS deposition. In our lab, we use NREL CBD Recipe to deposit the high quality CdS buffer layer.

Materials used:

- $\text{NH}_4\text{OH}$  (28-30%)
- $\text{CdSO}_4(8/3)\text{H}_2\text{O}$  (0.015M) for pure  $\text{CdSO}_4$  (0.015M=1.56345g/500ml water)
- $\text{NH}_2\text{CSNH}_2$  (1.5M)
- HCl (for the cleaning of the reaction vessel)
- DI  $\text{H}_2\text{O}$  (DI: Deionized water)

Prepare of the following solutions:

{1}  $[\text{CdSO}_4(8/3)\text{H}_2\text{O}]$  1.923 g 500 mL DI water

{2}  $[\text{NH}_2\text{CSNH}_2]$  57.09 g 500 mL DI water

Stir the solution for 30 minutes, vacuum filter the solution using a clean 0.2 m tissue culture filter unit.

Hardware:

- Two 1000 mL beakers
- Sample holder
- Hot plate with a magnetic stirrer
- Magnetic stirring rod
- Thermometer
- Filter unit

### Deposition Procedure:

- Set the temperature control system (circulator) at  $T=65\text{ }^{\circ}\text{C}$
- Place the first 1000 mL beaker (referred as the “reactor” in the suite)
- Put the reactor on the magnetic stirrer
- Put a magnetic stirring rod into the beaker.
- Select a slow stirring speed.
- Place the substrates/samples into the sample holder.
- Place the sample holder with samples into the reactor.
- Place the thermometer in the reactor to monitor temperature.
- Mix 366 mL DI  $\text{H}_2\text{O}$ , 62.5 mL  $\text{NH}_4\text{OH}$ , 50 mL of the solution {1} and 25 mL of the solution {2} into the second 1000 ml beaker.
- Add above mixture to the reactor.
- Wait for 13 minutes of deposition time.
- Remove the sample holder and immerse it into the glass beaker filled with DI water.
- Remove the substrates from the sample holder.
- Rinse the substrates with DI water and blow dry with nitrogen.

The bath is covered to help stabilize the temperature and reduce the loss of ammonia. The solution, which is initially clear, becomes pale green, yellow, gold and then bright orange during the deposition. The substrates become coated with a thin layer of smooth, shiny CdS film, which, in turn, is covered by a thick layer of loosely adherent powder for longer duration deposition. This powder can be removed by ultrasonic cleaning.

CdS films are formed through the reaction of adequately dissolved ammonia, cadmium and thiourea precursors. Under certain conditions, these precursors form thin

polycrystalline CdS films on any material surface. The deposited films are dependent on temperature, relative concentrations of precursors, solution PH and stirring.

Several studies reported that an ultra thin inverted n-type layer is created after the CdS buffer layer deposition. It has been observed that this inverted layer is an n-type ordered vacancy compound (OVC) with energy bandgap around 1.3 eV, such as  $\text{CuIn}_3\text{Se}_5$ , and hence the buried homojunction is formed in the CIGS cells.

### **Alternative Cd- Free Buffer Layer**

In the past few years, the CBD process has drawn considerable attention as an excellent method for the deposition of the Cadmium Sulfide (CdS) buffer layer in efficient thin-film solar cells with either chalcopyrites ( $\text{CuInSe}_2$  (CIS) and  $\text{Cu(In,Ga)Se}_2$  (CIGS)) or CdTe absorbers. Very good efficiencies have been obtained using the CBD-CdS buffer layers. Among various buffer layer materials such as CdS,  $(\text{Cd,Zn})\text{S}$ , ZnS,  $\text{Zn(O,S,OH)}_x$ , ZnO, ZnSe,  $\text{In}_x(\text{OH,S})_y$ ,  $\text{In}_2\text{S}_3$ ,  $\text{In(OH)}_3$ ,  $\text{SnO}_2$ ,  $\text{Sn(S,O)}_2$ , ZnSe, or  $\text{ZrO}_2$  deposited by CBD, ALE, MOCVD, or other deposition methods, the best performance CIGS solar cells with a total-area conversion efficiency of 18.8% and other high-efficiency ( $> 17\%$ ) CIGS solar cells were obtained using the CdS buffer layer deposited by the CBD method. Using wider band gap materials to replace the CdS ( $E_g=2.4\text{eV}$ ) buffer layer could improve the quantum efficiency of the CIGS cells at shorter wavelengths, resulting in an increase of the short-circuit current. The  $(\text{Cd,Zn})\text{S}$  buffer layer has a band gap energy greater than 2.4eV and can provide a better lattice match to the CIGS absorber layer. Other alternative buffer layers have also been investigated as possible replacement for the CdS buffer layer to avoid the use of Cd because of its toxicity. Using ZnS ( $E_g=3.6\text{eV}$ ) and  $\text{In(OH)}_x\text{S}_y$  ( $E_g=2.54\text{eV}$ ) buffer layers for CIGS solar cells have achieved high active-area conversion efficiencies of 16.9

and 15.7%, respectively. Thus, both ZnS and  $\text{In}(\text{OH})_x\text{S}_y$  films deposited by CBD process are promising candidates for the Cd- free buffer layers among the reported alternative materials for CIGS cells.

### **Transparent Conducting Oxide (TCO) Layer**

A transparent conductive film is a material that is highly transparent in the range of visible light, and at the same time, electrically conductive. The interest in these transparent conductors can be traced back to the early 20th century when reports of CdO films first appeared. Since then there has been a steadily growing interest in these materials with their unique properties. It is well known that non-stoichiometric and doped films of oxides based on Tin, Indium, Cadmium, Gallium, Copper and Zinc and their blends exhibit high transmittance and conductivity. Products such as flat panel displays, solar cells, optoelectronic and electronic components and thermally insulating architectural glass have one thing in common: they have to combine the opposing material properties transparency and electrical conductivity. Transparent conductive films can be produced by multi- layer coatings based on thin metal films or by a homogeneous coating based on wide band gap semiconductors.

Transparent Conductive Oxides are key components in flat panel displays and solar cells. The main deposition technology used for large area deposition is the Physical Vapor Deposition (PVD) technology. Such “intelligent” films can be produced by using conductive oxides based on n-type TCO's and p-type TCO's in well defined layer stacks, which will lead to new applications in the field of transparent electronics and optoelectronics, like transistors, diodes, active sources and detectors. For many manufacturing companies of TCO films it is the aim to achieve stable film properties for large area coating processes with low film resistance and high transmittance within the

visible spectrum range. A lot of efforts were made to develop technologies to produce TCO coatings by reactive sputter technology. With adding oxygen or nitrogen gas into the coating chamber it is possible to produce oxide or nitride dielectric layers from metal targets. But all of these reactive sputtering coating processes suffer from the fact that a chemical reaction takes place not only at the produced layer, but at the metal target as well. Additionally a homogeneous gas flow and gas distribution in the coating chamber is necessary to achieve high quality TCO coatings. For several applications the substrate geometry is limiting the gas distribution as well. This has led more and more to coating machines with highly sophisticated in-situ process measurements and gas flow control systems to stabilize the reactive sputter process. Mainly because of quality and cost reasons more and more manufacturing companies were using the conductive oxides which are easier to handle than pure metal targets. For the last three decades Indium Tin Oxide (ITO) has been the most popular n-type TCO material used for layer stacks for these applications. It is well known that ITO is an expensive coating material in the thin-film market, and for quite some times a substitute that could provide cost savings while provide similar properties is still missing. This forces the use of ITO, and has kept many companies at the mercy of price fluctuations of the raw material.

In the technological development of the various solar cells as described above, there are several aspects of cross-fertilization and common problems. Examples are glass washing, glass bending and warp age at elevated temperatures, roll-to-roll processing, vacuum deposition; laser scribing, heat treatments, etc. While special attention was drawn to this during the interviews, no common answers were found, except in the area of transparent conductive oxides. For all thin-film PV technologies, optimization of the

transparent conductive oxides for the transparent contacts is of crucial importance. Improvement is needed, since current materials are far from optimal with respect to the light transmittance and conductivity that are desired for PV applications. Development and exploring characterizations techniques are important for the understanding of the material properties and behaviors. All thin-film solar-cell technologies will benefit from these developments. For PV applications a thorough understanding of the optical and electrical properties of the TCO material is important in order to minimize the optical and electrical losses.

However, traditionally indium tin oxide (ITO) has been the TCO of choice but it is expensive because of the low natural abundance of indium. With appropriate doping, transparent ZnO conducting films can be produced. From a purely financial viewpoint doped ZnO TCO films are preferable to ITO as the natural abundance of Zn is 1000 times higher than that of indium. Therefore, ZnO becomes a very promising candidate of TCO layer of thin-film solar cells especially for CIGS-based solar cells. As grown, nominally undoped, ZnO usually demonstrates n-type conductivity because of the presence of either Zn interstitials or O vacancies [44]. The literature is still unclear, however, as to which of these intrinsic defects are the cause of the conductivity. Unfortunately the as-grown films are not suitable for device applications as the resistivity is too high and the re-oxidation of the Zn rich films at ambient temperatures removes the source of the conductivity. To introduce stable n-type conductivity two dopants that are used most are Ga and Al [45–52], although doping with other elements such as B [53], In [54, 55] and Zr [47] has also been investigated. Al doped ZnO and Ga doped ZnO films can be used as electrodes for flat panel displays, low emissivity glass, as thin-film solar cells and as anode material

for organic light emitting diodes [46]. In CIGS solar cell fabrication, magnetron sputtering technique is used to deposit an ultra thin intrinsic ZnO layer followed by a 300 nm Al doped n-type ZnO conducting layers.

### **Metal Contact**

Several runs of E-beam evaporation experiments were made in our microelectronics lab. During the fabrication of CIGS cells, as a result, details of E-beam technique related to the deposition of Ni/Al contacts on solar cells were learned from this practice. Figure 5-4 shows the basic system of the E-Beam machine in the Microelectronics Lab of ECE department at UF. An ultra thin Ni film was deposited on CIGS to prevent the diffusion from Al ohmic contact layer to ZnO layer because of the activity of Al. Since Ni is much harder than Al, it can protect the ZnO layer from being damaged by the needle probe when characterizing the device.

Table 5-1. Conversion efficiencies of CIGS cells grown by non-vacuum processes (by ISET) on different substrates.

Substrate	Conversion efficiency	Air mass index
Soda Lime Glass	13.6%	AM 1.5G
Molybdenum Foil	11.5%	AM 1.5G
Titanium Foil	9.5%	AM 1.5G
Polyimide Film	9.3%	AM 0

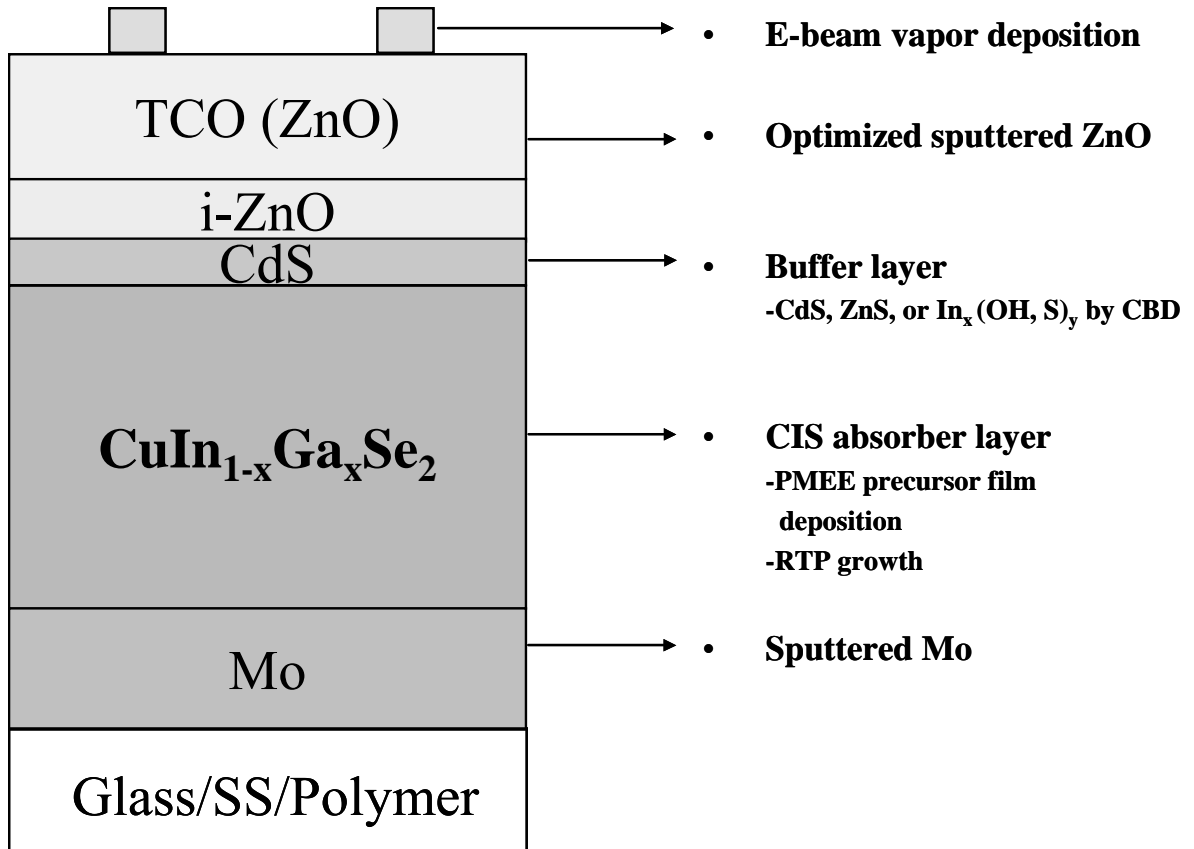


Figure 5-1. Layer structure of CIS/CIGS based solar cells.

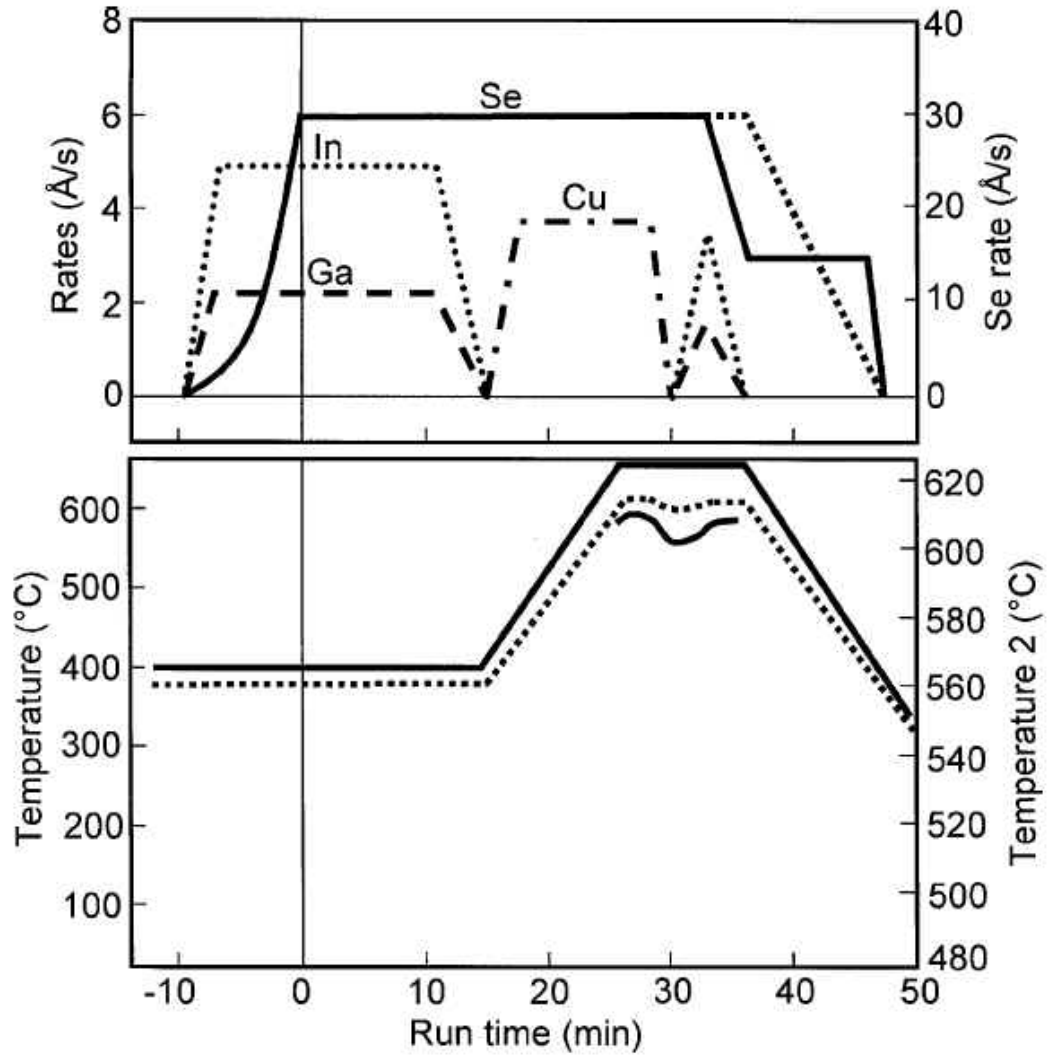


Figure 5-2. Schematic profile of the NREL 'three-stage physical evaporation process for the fabrication of CIGS solar cells'.

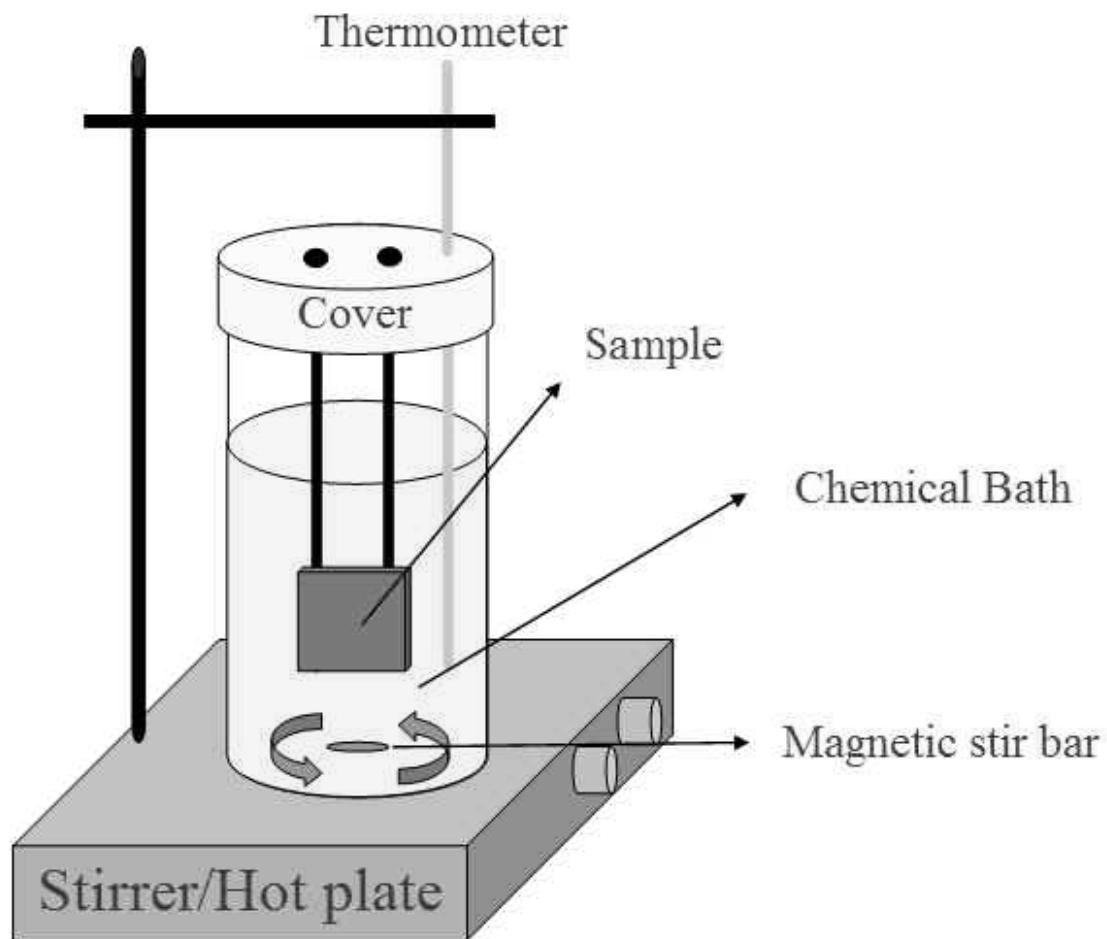
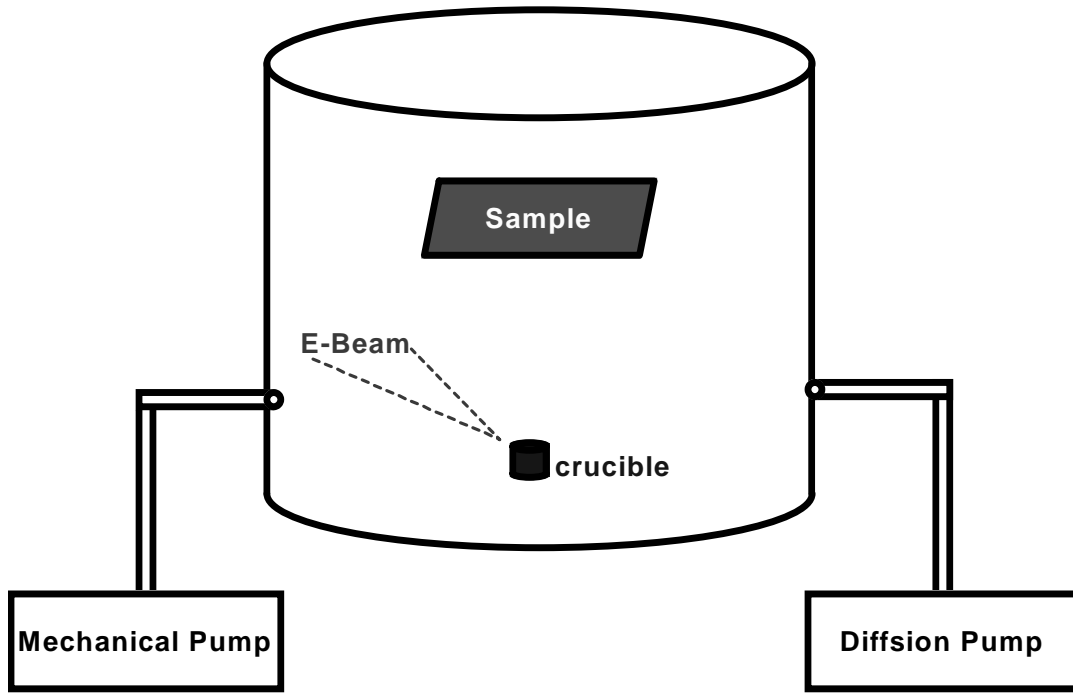


Figure 5-3. Simple CBD experimental set-up.



E-Beam deposition of Ni/Al metal contact

Figure 5-4. The E-Beam evaporation technique for depositing metal contact films on solar cells.

## CHAPTER 6 CHARACTERIZATION AND MEASUREMENT SYSTEMS FOR CIGS SOLAR CELLS

Characterization and measurements of CIGS based thin-film solar cells are important for determining and evaluating the quality of absorber layers, film surface morphology, film compositions, the electrical and optical properties of absorber layers and the overall device performance. In this chapter, the fundamental device physics and cell structure, experimental setups, characterization of CIGS absorber layers, and measurements and analysis of the device performance parameters of CIGS solar cells are presented. .

### **Hall-Effect Measurements**

#### **Introduction**

The Hall Effect was discovered more than 100 years ago when Hall observed a transverse voltage across a conductor subjected to a magnetic field. This technique can be used to determine the material type, carrier concentration and carrier mobility in a semiconductor. The basic principle of Hall effect in a semiconductor is illustrated in Figure 6-1.

The Hall coefficient,  $R_H$ , is defined by Equation 6-1.

$$R_H = \frac{tV_H}{B_z I_x} \quad (6-1)$$

Since the magnetic field,  $B_z$ , will deflect either electrons or holes (n- or p-type) to the bottom of the sample, the sign of  $V_H$  changes depending on the material type, so does the Hall coefficient. All the quantities in Equation 6-1 for  $R_H$  are measured

experimentally, and the electron and hole densities can be determined from the measured Hall coefficients, which are given by Equation 6-2.

$$p, n = \pm \frac{1}{qR_H} \quad (6-2)$$

Where the “+” sign applies for holes and the “-” sign for electrons. The majority carrier mobility can be determined from the measured Hall coefficient and electrical conductivity, which is given by Equation 6-3.

$$\mu_H = \frac{|R_H|}{\rho} = |R_H| \sigma \quad (6-3)$$

Where  $\rho$  and  $\sigma$  is the electrical resistivity and conductivity of the semiconductor, which can be determined by using four-point-resistivity measurements.

### **Measurement Procedure and Apparatus**

CIGS absorbers deposited directly on SLG substrates are used in Hall effect measurements. Ohmic contacts are made by attaching 4 small indium dots placed at the corners of a square CIGS sample annealed at  $\sim 160^\circ\text{C}$  in ambient. Contact quality is verified by the linear I-V characteristics (Figure 6-2).

Standard Hall effect and Van der Pauw resistance measurements [56, 57] were employed to determine the hole concentration and mobility in CIGS films. The Hall voltage was measured using a constant magnetic field of 3000 G, at room temperature. The Hall effect and resistivity measurements on the CIGS samples were made using a computer-controlled MMR Hall effect measurement system, which employs the four-point probe Van der Paul technique for determining the electrical conductivity and the Hall coefficient of the measured sample.

## **Related Studies, Results and Discussion**

The objective of this research task is to develop and optimize the Cd-partial-electrolyte treatments of CIGS films -and to analyze their effects on the performance of CIGS-based solar cells. Hall effect and resistivity measurements were made on CIGS samples supplied by NREL, GSE, ISET, and EPV to determine the carrier densities and Hall mobilities in these samples. In addition, Hall data of CIS/CGS films deposited by UF PMEE growth system are also presented.

### **The Cd-partial-electrolyte treatment on CIGS films**

Similar to the procedure of depositing the CdS buffer layer on CIGS films using CBD, the aqueous solution consisting of  $2.4 \times 10^{-4}$  M CdCl<sub>2</sub>,  $7.43 \times 10^{-4}$  M NH<sub>4</sub>Cl,  $6.61 \times 10^{-4}$  M NH<sub>4</sub>OH at a bath temperature in the range of 80 to 85°C was applied for the Cd partial-electrolyte treated CIGS samples. In order to remove the possible precipitation, which may be deposited on the surface of the films, the CIGS samples were thoroughly rinsed with DI water after the deposition and blown dry with nitrogen stream.

Four 1×1 inch identical CIGS samples, which were cut from a 2×2 inch uniform slab, were applied by using Cd-partial-electrolyte treatment with different soaking time. Hall measurements were made to characterize the effect of Cd-partial-electrolyte treatments on the carrier density and mobility of the samples. The results (Table 6-1) reveal that Cd-partial-electrolyte treatments increase hole density and decrease Hall mobility with increasing Cd-treatment time. No correlation was found between the resistivity and the Cd-dip time. One possible explanation of this effect is that during the Cd-partial-electrolyte treatment, Cd ions occupy the Cu- vacancy sites and create donors with densities in the range of  $10^{17}$ - $10^{18}$  cm<sup>-3</sup>, thus an ultra-thin n- type surface inversion

layer (5-10 nm) is formed [58]. The mixed conduction of electrons in such layer and holes in the p-CIGS absorber layer decreases the measured Hall coefficient and consequently yields higher hole density in the Cd-dip CIGS films.

In addition, Hall effect and resistivity measurements were made on the CIGS samples received from GSE, ISET, EPV and NREL, along with the CIS/CGS samples deposited by our group using PMEE method on different substrates (GaAs/glass). The experimental results are summarized in Table 6-2 and Table 6-3, respectively.

#### **Hall-effect data of CIGS films supplied by NREL TFPPP team**

Four CIGS films (sample A, B, C and D) deposited on glass substrates were tested by our MMR Hall and Van Der Pauw measurement system at a fixed magnetic field of 3000 G and at 300 K. To measure the Hall voltage laterally across the CIGS film, the film must be deposited on the insulating substrate. Thus, the portions of samples A, B, and D used for Hall effect measurements were deposited on bare soda-lime glass (SLG) substrate, rather than on the Mo-coated SLG substrate. Sample C was deposited on the stainless steel substrate, and then peeled from the steel substrate after coating with epoxy. Hall effect was not measured on samples E and F, as these films were not available on insulating substrates.

Table 6-2 shows a summary of the Hall measurement results, including the hole concentration, Hall mobility, and resistivity data. Order of magnitude variations over the sample group are evident in each quantity. Possible complications in interpretation of the Hall effect data include contribution from the mixed conduction types, differences in films grown without Mo versus under standard conditions, and changes to films during subsequent window layer processing.

### Photo- and Dark- J-V Measurements

J-V measurement is a very important diagnostic tool for evaluating the electrical performance of solar cells. The electrical parameters including the open-circuit voltage  $V_{oc}$ , short-circuit current density  $J_{sc}$ , fill factor F.F., conversion efficiency  $\eta$ , series resistance  $R_s$ , shunt resistance  $R_{sh}$ , diode quality factor  $n$ , and reverse saturation current density  $J_0$  of a solar cell can be determined from the measured dark- and photo- J-V curves. These parameters are very important for assessing the performance of CIGS solar cells.

### Solar Cell Parameters

In order to evaluate the performance of a solar cell it is essential to know the key device parameters of solar cells. The following derivation is based on a typical PN junction solar cell theory from [59].

The equivalent circuit for a CIGS solar cell (Figure 6-3) is composed of the photocurrent component represented by a constant current source,  $I_{ph}=I_{sc}$ , a dark current component,  $I_D$ , a shunt resistance,  $R_{sh}$ , and a series resistance,  $R_s$ . If one neglects the effects of shunt resistance (assuming  $R_{sh} \rightarrow \infty$ ), series resistance ( $R_s \sim 0$ ), and the recombination current ( $I_r = 0$ ) in the depletion region. Based on the assumption given above, the photo- I-V characteristics of a p-n junction solar cell under illumination condition can be expressed by Equation 6-4.

$$I = -I_{ph} + I_{01}[\exp(qV / k_B T) - 1] \quad (6-4)$$

Where the total photocurrent density  $I_{ph}$  generated in a p-n junction solar cell under one-sun condition can be obtained by Equation 6-5.

$$J_{ph} = \int_{\lambda_1}^{\lambda_2} J_L(\lambda) d\lambda \quad (6-5)$$

Where  $\lambda_1$  and  $\lambda_2$  are the cutoff wavelengths at the short- and long-wavelength limits of the solar spectrum, respectively. For a typical p-n junction solar cell,  $\lambda_1$  can be set at 0.3  $\mu\text{m}$  (from UV light), and  $\lambda_2$  is determined by the cutoff wavelength or the band gap energy of the semiconductor (i.e.,  $\lambda_2 = \lambda_g = 1.24/E_g$  ( $\mu\text{m}$ )). The reverse saturation current  $I_{o1}$  because of the injection of electrons and holes across the p-n junction is given by Equation 6-6

$$I_{o1} = qn_i^2 A_j \left( \frac{D_p}{L_p N_D} + \frac{D_n}{L_n N_A} \right) \quad (6-6)$$

Where  $A_j$  is the junction area;  $n_i$  is the intrinsic carrier density;  $D_n$  and  $D_p$  denote the electron- and hole- diffusion coefficients;  $L_n$  and  $L_p$  are the electron- and hole- diffusion lengths, respectively. The short-circuit current can be obtained by setting  $V = 0$  in Equation 6-4, which yields

$$I_{sc} = -I_{ph} \quad (6-7)$$

Which shows that the short- circuit current  $I_{sc}$  is equal to the photo-generated current,  $-I_{ph}$ . The open-circuit voltage,  $V_{oc}$ , can be obtained by setting  $I = 0$  in Equation 6-4, and the result yields

$$V_{oc} = V_T \ln \left[ \left( \frac{I_{sc}}{I_{o1}} \right) + 1 \right] \quad (6-8)$$

Where  $V_T = k_B T/q$  is the thermal voltage. It is seen from Equation 6-8 that  $V_{oc}$  depends on the ratio of the short-circuit current and the dark current, and  $V_{oc}$  can be increased by keeping the ratio of  $I_{sc}/I_{o1}$  as large as possible. This can be achieved by reducing the dark current, either by increasing the substrate doping density or increasing the minority carrier lifetimes in the solar cell. Increasing the short-circuit current can also enhance  $V_{oc}$  but it is not as drastic as reducing the dark current in the solar cell. In practice, the  $V_{oc}$  can

be improved by incorporating a p-p<sup>+</sup> back surface field (BSF) structure in the n-p junction solar cell. The BSF structure not only can deflect the minority carriers back into the junction but also reduces the back contact resistance of the cell. As a result,  $V_{oc}$ ,  $J_{sc}$ , fill factor ( $FF$ ), and conversion efficiency can be improved with the BSF structure. Values of  $V_{oc}$  for a silicon p-n junction solar cell may vary between 0.5 V and 0.7 V depending on the cell structure, doping densities, and other device parameters used in the cell's design and fabrication.

If one includes the series resistance  $R_s$  and neglects the shunt resistance effect (i.e.,  $R_{sh} \rightarrow \infty$ ) in the I-V equation, then the output current of the solar cell can be expressed as

$$I = I_D \{ \exp[(V - IR_s) / V_T] - 1 \} - I_{ph} \quad (6-9)$$

And the output power is given by

$$P = IV = I [ V_T \ln \left( \frac{I + I_{ph}}{I_D} + 1 \right) + IR_s ] \quad (6-10)$$

The maximum output power can be calculated using the expression

$$P_m = V_m I_m \quad (6-11)$$

Where

$$I_m = (I_{sc} + I_{01}) \left[ \frac{(V_m / V_T)}{(1 + V_m / V_T)} \right] \quad (6-12)$$

$I_m$  is the current corresponding to the maximum power output, which is obtained by differentiating Equation 6-10 with respect to current  $I$  and setting  $\partial P / \partial I = 0$ . It is noted that  $V_m$  is obtained by solving the equation given below using the iteration procedure.

$$\exp(V_m / V_T) [1 + V_m / V_T] = \exp(V_{oc} / V_T) \quad (6-13)$$

Another important solar cell parameter known as the fill factor (F.F.), which measures the squareness of the photo- $I$ - $V$  curve shown in Figure 6-4, is defined by

$$\text{F.F.} = \frac{V_m I_m}{V_{oc} I_{sc}} = \left( \frac{V_m}{V_{oc}} \right) \left[ 1 - \frac{e^{V_m/V_T} - 1}{e^{V_{oc}/V_T} - 1} \right] \quad (6-14)$$

Depending on the values of diode ideality factor and shunt- and series- resistances, the fill factor for silicon p-n junction solar cells may vary between 0.75 and 0.85, while for a GaAs solar cell it may vary between 0.79 and 0.87.

Finally, the conversion efficiency of a p-n junction solar cell can be calculated by

$$\eta_c = \left( \frac{P_{out}}{P_{in}} \right) \times 100\% \quad (6-15)$$

Where  $P_{in}$  is the input power from the sunlight, and  $P_{out}$  is the output power from the solar cell. The input power from the sunlight under one-sun AM0, AM1, AM1.5G, and AM2 conditions are given by 135.3, 92.5, 100, and 69.1 mW/cm<sup>2</sup>, respectively.

### **Photo- J-V Measurement System**

Our photo- and dark- J-V and quantum efficiency (Q.E.) measurement system are constructed by the previous Ph.D student, Dr. Chia-Hua Huang [60]. The photo- J-V performance of solar cells can be considered as accurate and useful only when the photo- J-V measurements are performed under the Standard Reporting Conditions (SRC) specifying the total radiation level, cell temperature, and reference spectral radiance distribution. The typical SRC for terrestrial solar cells are a total irradiance of 100 mW/cm<sup>2</sup>, a reference spectrum of AM1.5 Global (ASTM Standard E892), and a cell junction temperature of 25°C. The apparatus used for the construction of our J-V measurement system and measurement procedure are based on the standard test method for electrical performance of photovoltaic cells using reference cells under simulated sunlight. The measurement system consists of a halogen lamp as the solar simulator, a temperature-controlled test chuck, a programmable power supply as the variable load,

electronic instruments for measuring the terminal voltage and current of the test cells, and a computer program for the control of the measurement procedure and for the data acquisition. The J-V curve of the test cell is measured from the forward bias to the reverse bias using the voltage mode with a resolution of 1mV.

### **Light source**

The ELH (tungsten-halogen bulb) lamp is utilized as a c-class solar simulator in our photo- J-V measurement system. The reference cell method, which basically uses the reference cell to adjust the illumination level of the solar simulator, is employed in the photo- J-V measurement of CIGS solar cells. The solar simulator intensity is adjusted by changing the distance between the solar simulator and the test plane so that the measured short-circuit current of the reference cell (from NREL) is equal to its calibrated value at the standard measurement intensity of  $100 \text{ mW/cm}^2$ .

### **Temperature control**

Since the open-circuit voltage of the CIGS solar cells decreases with increasing temperature, it is important to maintain the cell junction temperature at a standard value ( $25^\circ\text{C}$ ) during the photo- J-V measurement. In our system, the temperature of the test cell is maintained at  $25 \pm 1^\circ\text{C}$  by using a thermoelectric cooler assembly with a temperature controller during the photo-J-V measurement. Because the CIGS solar cells are deposited on the 2 mm glass substrates, a temperature difference of  $3\text{-}5^\circ\text{C}$  exists between the top and bottom surfaces of the solar cell under a light intensity of  $100 \text{ mW/cm}^2$ . A thermocouple is used to measure the top surface temperature of the test cell during the measurement. Therefore the temperature controller of the cooling system is set at about  $\sim 20^\circ\text{C}$  to keep the reading of the thermocouple and hence the temperature of the top surface of the test cell at  $25 \pm 1^\circ\text{C}$ .

### **Contacts and connections**

The four-terminal contacts (also known as the Kelvin connections) are used for the connection between the test cell and the measurement system. Not only the wiring resistance but also the contact resistance between the probe tips and the contact pads of the solar cell can be neglected for the efficiency measurements by using the four-terminal contact method. In addition, a more accurate efficiency measurement for the solar cells can be achieved by using this method. Four micromanipulators with tungsten probe tips with radii in the range of 0.6 to 25  $\mu\text{m}$  are utilized to adjust the position of the probe tips for contacting the small contact pads of the test cell. The voltage and current probes for both the top and bottom contacts should be placed as close as possible to avoid a high voltage drop between the two probes, and the resistance between the voltage and current probes is hence minimized (less than 5  $\Omega$ ).

The photo and dark- J-V measurement system (Figure 6-5 [60] and 6-6), controlled by a personal computer with the data acquisition and data analysis software *LabVIEW*, is composed of a programmable bipolar power supply served as the variable applied voltage source, an electrometer for measuring the terminal current, and a digital multimeter for measuring the terminal voltage of the test cell. The measuring range for current measurements by the electrometer is from 1 fA to 20 mA. Although the upper limit of the electrometer is only 20 mA, the photo-generated current of the CIGS cell under test is typically smaller than 20 mA because of the small area (usually 0.429cm<sup>2</sup>) of the CIGS cells fabricated in a laboratory scale. With the sensitivity in the low-current measurements, the electrometer with a current resolution of 0.1 fA is perfectly ideal for the dark- J-V measurement.

The PC based control program is written by the previous Ph.D. student, Dr. Chia-Hua Huang in the *LabVIEW* for data acquisition from the readings of electrometer, multimeter, and power supply. The program also controls the measurement procedure by sending commands to the programmable power supply via interface of GPIB for the completion of a full sweep of the J-V curve.

For photo- J-V measurements, the illumination intensity of the solar simulator is first set by using the reference cell method depicted above. The test cell is exposed under this condition and biased at around the maximum power point for about 10 minutes (i.e., light soaking effect). The J-V curve is then swept from the forward bias to the reverse bias using the voltage mode with a resolution of 1 mV. Using the *LabVIEW* data acquisition software (Figure 6-6) the basic parameters such as  $V_{OC}$ ,  $J_{SC}$ , fill factor F.F., output voltage at maximum power point  $V_{MAX}$ , output current density at maximum power point  $J_{MAX}$ , maximum power point  $P_{MAX}$ , and conversion efficiency  $\eta$  of test cells can be directly obtained from the measured photo-J-V curves. The open-circuit voltage  $V_{OC}$  is determined from a linear fit to the J-V curve near zero output current, and similarly  $J_{SC}$  is determined from a linear regression to the J-V points near zero output voltage. The maximum power point  $P_{MAX}$  is obtained from an at least fifth-order polynomial fit to the data points of the output power versus voltage with the constraints in which the  $P_{MAX}$  must be greater than 85% of the measured maximum power and the  $V_{MAX}$  must be greater than 85% of the measured  $V_{MAX}$ .

### **Dark- J-V Measurement**

The experimental procedure of Dark- J-V measurement is similar to the Photo- J-V measurement except there is no incident light illuminating on the test device. From the

measured dark JV curve and data (Figure 6-7), we can further extract and calculate many important parameters of the device such as reverse saturation current density ( $J_0$ ), diode quality factor ( $n$ ) and series resistance ( $R_s$ ).

### **Quantum Efficiency Measurement**

Measurements of the spectral response in terms of the wavelength dependence of the photo-generated current density for a solar cell as the characterization and diagnostic techniques are extremely important for quality control of each layer in cell fabrication, cell design, and understanding the diffusion mechanisms and separation of the individual photocurrent loss mechanisms. The external quantum efficiency, which is defined as the ratio of the generated electron-hole pairs per incident photon with certain wavelength, of the solar cell can be calculated from the measured absolute spectral response curve. A computer-controlled spectral response measurement system using a monochromator for wavelength selection to measure the spectral response (S-R) and quantum efficiency (Q-E) of the CIGS-based solar cells was designed and constructed. The measurement system scanning the spectral range from 400 nm to 1400 nm with 10 nm as an increment step has the capability of applying white light bias and voltage bias to the test cell. During the measurement the entire area of the test cell is covered with a uniform and sufficient illumination-level monochromatic light. A computer program based on the software of *LabVIEW* was used to control the measurement procedure and data acquisition.

### **Quantum Efficiency Measurement Instrumentation**

Two types of measurement systems, i.e., the filter wheel and grating monochromator systems, are commonly used to measure the spectral response of the solar cells. The grating monochromator system has the basic feature of the flexibility to

select wavelength, but has low light intensity, poor beam uniformity, and small beam size. While the filter wheel system has the features of higher light intensity, better beam uniformity, and larger beam size, but has the drawback of limited and fixed wavelengths in spectral response measurements. With the small area of the CIGS-based solar cells fabricated at UF, we have constructed a spectral response measurement system using a grating monochromator to analyze the spectral response and quantum efficiency of our solar cells. The measurement system scanning the spectral range from 400 nm to 1400 nm with 10 nm as an increment step has the capability of applying white light bias and voltage bias to the test cell when the measurement is performed.

### **Monochromator and Monochromatic Light Source**

As illustrated in Figure 6-8 [60], a 30- Watt tungsten-halogen lamp is coupled with the monochromator as a light source to produce a monochromatic light with a narrow bandwidth of about 10 nm in the wavelength range from 350 nm to 2500 nm and with a resulting beam size of around 9mm×14mm on the test plane. With the consideration of possible spatial non-uniformity of the test cell to the spectral response, significant errors arising from the test cell and reference detector with different size or shape under a non-uniform monochromatic light [61], and the potential disadvantages, namely the low light intensity, uneven light distribution, and small beam size, directly inheriting from a typical monochromator measurement system, the geometric location and selection of the optical components including the lenses, mirror, and optical diffuser are specially arranged with caution so that the entire area of the cell on the test plane is covered with a uniform and adequate illumination-level monochromatic light. The entrance slit width of the monochromator is opened to its maximum to increase the throughput of light

intensity at the expense of the resulting image resolution from the output of the monochromator. The exit slit width of the monochromator is opened to around 2.8 mm to keep the bandwidth of the monochromatic light at about or less than 10 nm for the wavelength from 400 nm to 1400 nm. The divergent monochromatic beam from the exit of the monochromator is collimated through the condenser lens, subsequently reflected onto the test plane via the high-reflection broadband flat mirror, and finally homogenized by a high-transmission (>85%) optical diffuser to make the monochromatic light more uniform without substantially sacrificing the light intensity.

Since there is no real-time calibration and the data of the incident power density on the test plane are stored before the photocurrent measurement, the care must be taken for the stability of the light source used for the monochromator. A stable well-regulated power supply is served as the power source for the light source of the tungsten-halogen lamp. Two order sorting filters are used to block the undesired harmonic terms from the monochromator. One with the cut-on wavelength of around 610 nm and the other with the cut-on wavelength of about 830 nm are applied for the ranges of wavelength from 630 nm to 1000 nm and from 1000 nm to 1400 nm, respectively. It is not necessary to use the order sorting filter for the range of wavelength from 400 nm to 630 nm because the silicon detector, which only responds to the wavelength above 360 nm, is used as the reference detector in the measurement system.

### **Monochromatic Light Chopper**

An optical chopper used together with a lock-in amplifier in the spectral response measurement system can discriminate the chopped ac signal from the undesirable noise and strong dc signal from the bias light, and hence increases the signal-to-noise ratio in the spectral response measurement system. However, errors can occur for the

inadequate use of chopped light method when the test cell and reference detector are of different size and/or shape [62]. These errors can be minimized by locating the chopper blade in the narrowest location of the monochromatic beam pathway [62]. Therefore, we put the chopper right next to the exit of the monochromator in the measurement system to reduce the errors. In order to avoid the interference of the harmonics from the power lines of the bias light, a chopping frequency of 150 Hz is used in the measurement.

### **Bias Light Source**

Besides the monochromatic light a bias light is typically used in the spectral response measurement not only to approximate the standard operating conditions but also to compensate to effects, which might be attributed to trapping mechanisms of the test cell, about the non-linearity of the photo-generated current in the cell to the illumination level. An ELH lamp is used as the bias light source in the measurement system. The light intensity of the ELH lamp is adjusted during the spectral response measurement, which is one hundred times greater than that of the monochromatic light, to provide with sufficient illumination level such that the short-circuit current is within 70-100% of the ISC measured from the photo- I-V measurement with respect to the SRC. A screen is placed between the chopper and lens to eliminate the undesired noise, whose magnitude can be comparable to the measured ac signal because of the high illumination-level bias light, resulting from the stray light reflected from the components and the possible direct illumination from the bias light through the chopper onto the test cell.

### **Spectral Detector and Synchronous Detection Instrumentation**

The NIST traceable calibrated silicon and germanium photodetectors together with a lock-in amplifier are employed to measure the incident power density of the frequency-chopped monochromatic light beam on the test plane of the measurement

system. In order to guarantee the measured incident power density is exactly same as the power density received on the solar cell surface, the surface heights of both detectors and the test cell on the testing stage are well adjusted to be equal. A zero-inductance four-terminal resistor of  $2\ \Omega$  is used as the current-voltage converter to convert the ac photocurrent generated from the photodetectors or the tested cell into the photovoltage, which is then fed into the lock-in amplifier. The monochromatic signal through the chopper becomes a trapezoidal waveform. For absolute photocurrent measurement of the detectors, the signal measured from the lock-in amplifier must be multiplied by a waveform correction factor (i.e. multiplicative constant) because the lock-in amplifier typically measure the amplitude of fundamental component of the trapezoidal waveform (root-mean-square signal), which is not exactly the same as the peak amplitude. Since the signals for the reference detectors and test cell are measured with similar electronic instruments, all multiplicative errors drop out and the absolute spectral response of the test cell can then be achieved.

### **Spectral Response Measurement Procedures**

The monochromator, which is controlled by a computer program written in *LabVIEW* software via the interface of GPIB, scans the spectral range from 400 nm to 1400 nm with 10 nm as an incremental step. The incident power density on the test plane is first measured by the photodetectors and the data are stored in the hard disk of the computer. The spectral response measurement is operated at the short-circuit mode by adjusting the variable load in the circuit loop to set the measurement at short-circuit condition with the terminal voltage of the test cell within  $\pm 5\ \text{mV}$ . The light intensity of the light-bias lamp is adjusted such that the short-circuit current is within 70-100% of the

$I_{SC}$  measured from the photo- I-V measurement with respect to the standard reporting conditions ( $100 \text{ mW/cm}^2$ ,  $25^\circ\text{C}$ , and reference spectrum). The ac photocurrent  $I_{\text{test cell}}(\lambda)$  of the test cell is converted into photovoltage with a zero-inductance four-terminal precision resistance and is measured by using a lock-in amplifier. Subsequently the spectral response is calculated from the data stored in the computer previously and the measured photocurrent of the test cell. The external quantum efficiency as a function of wavelength can be converted from the spectral response using the following expression:

$$QE(\lambda) = \frac{h \cdot c \cdot I_{\text{test cell}}(\lambda)}{q \cdot \lambda \cdot \text{power density}_{\text{detector}} (\text{W/cm}^2) \cdot \text{Area}_{\text{test cell}} (\text{cm}^2)} \times 100\% \quad (6-16)$$

Where  $h$ ,  $c$ ,  $q$ , and  $\lambda$  are the Plank constant, speed of light, electronic charge, and the photon wavelength, respectively. Figure 6-9 shows the spectral response and external quantum efficiency of a UF CIS solar cell taken by this measurement system.

### **Deep Level Transient Spectroscopy (DLTS) Measurement**

#### **Features and Principles**

The Deep-Level Transient Spectroscopy (DLTS) technique developed by Lang [63] provides a fast thermal scan of all the defect levels that are electrically active in the junction region of a diode. The main features of DLTS include:

- The saturated peak height is directly proportional to the density of the defect level.
- The temperature at which the peak occurs is related to the ionization energy of the defect level.
- The sign of the peak indicates whether it is because of majority or minority carrier emission.
- The activation energy of the defect level can be determined from an Arrhenius plot of the emission rate versus inverse temperature from several DLTS scans of the trap level with different rate windows.

- The carrier capture cross section can be determined directly from the dependence of DLTS peak height on pulse width.

Therefore, the DLTS technique allows a scan of all defect levels and provides information concerning defect density, energy level, and capture cross section. From the DLTS scans, one can obtain the useful information concerning defects in the depletion region of a p-n junction by observing the capacitance transient associated with the return to thermal equilibrium following an applied non-equilibrium condition. Majority and minority carrier traps can be investigated by a momentary zero bias ( $V_H = V_R$ , where  $V_H$  is the applied pulse height and  $V_R$  is the quiescent reverse bias) and a forward bias condition ( $V_H > V_R$ ), respectively. Before applying the pulse, the diode is under reverse bias condition with a wide depletion region and small capacitance. During the pulse, the depletion width decreases and the carrier traps in the depletion region are filled with the carriers. After the pulse, the depletion region returns to the equilibrium condition but the capacitance reaches its quiescent value slowly because of the trapped carriers.

It is possible to characterize the hole-emission rate ( $e_p$ ) as a function of inverse temperature ( $T^{-1}$ ) in the p-type absorber layer by scanning the capacitance change over a wide range of temperatures under different rate windows in a CIGS n-p junction cell. The hole- emission-rate is related to the hole- capture cross-section and activation energy by

$$e_p = \sigma_p v_{th} N_v \exp\left(-\frac{E_a}{kT}\right) \quad (6-17)$$

Where  $v_{th}$  is the thermal velocity,  $\sigma_p$  is the hole capture cross-section, and  $N_v$  is the effective density of the valence band states [59]. From an Arrhenius plot (*i.e.*,  $\ln(T^2\tau)$ )

vs.  $T^{-1}$ , where  $\tau = 1/e_p$ ), the activation energy ( $E_a$ ) and the capture cross-section ( $\sigma_p$ ) of the hole- trap level can be extracted. If the capture cross-section for the hole trap is because of a thermally activated process, then it can be expressed by  $\sigma_p = \sigma_\infty \exp(-\Delta E_o/kT)$ , where  $\sigma_\infty$  is the hole capture cross- section when the temperature approaches infinity, and  $\Delta E_o$  is the capture cross-section activation energy. The defect density ( $N_T$ ) can be calculated using the expression

$$N_T \approx \frac{2 \Delta C}{C_0} N_A \quad (6-18)$$

Where  $N_A$  is the net hole- density in the absorber layer;  $\Delta C$  is the capacitance change because of the emission of hole carriers from the trap level, which is proportional to the trap density, and  $C_0$  is the junction capacitance measured at the DLTS peak temperature with a quiescent reverse bias voltage ( $V_R$ ). Equation 6-18 is valid for  $N_T < N_A$ . The net hole-density in a p-type CIGS absorber can be determined from the C-V measurements.

The DLTS spectra (Figure 6-10 (a)) measured for a CIGS device from EPV, obtained using a pulse height of  $V_H = 0.3$  V, a reverse bias of  $V_R = -0.1$  V and a saturation pulse width of  $W = 10$  ms. This CIGS cell shows a deep hole- trap at  $T \approx 270$  K. The activation energy calculated from the Arrhenius plot of Figure 6-10 (b) for this hole- trap is  $E_a = E_v + 0.94$  eV. The average hole-density ( $N_a$ ) obtained from the C-V measurement at 270 K was  $3 \times 10^{15}$  cm<sup>-3</sup>. Using the capacitance vs. temperature (C-T) data,  $C_0$  was found equal to 301 pF, and from Equation 6-18 the hole trap density ( $N_T$ ) was found to be  $6.5 \times 10^{13}$  cm<sup>-3</sup> [64].

### Related Results and Discussions

Because of the fast thermal scan of the test cell during DLTS measurement, it is very important to know whether there are some effects on CIGS electrical performance during or after DLTS. Based on this idea, a CIGS solar cell (fabricated by NREL) was measured by photo- and dark- J-V system before and after the DLTS scans. The DLTS scan (Figure 6-11 (a)) measured for this CIGS device, obtained using a pulse height of  $V_H = 0.7$  V, a reverse bias of  $V_R = 0.5$  V and a saturation pulse width of  $W = 10$  ms. This CIGS cell shows a shallow trap at  $T \approx 120$  K. The activation energy calculated from the Arrhenius plot (Figure 6-11 (b)) for this hole- trap is  $E_a = E_c - 0.038$  eV. The average hole-density ( $N_a$ ) obtained from the C-V measurement at 120 K is  $7.53 \times 10^{15}$  cm<sup>-3</sup>. From Equation 6-18 the trap density ( $N_T$ ) was found to be  $1.10 \times 10^{14}$  cm<sup>-3</sup>. (DLTS data and calculation were made by W. K. Kim)

Dark- and photo- J-V measurements were taken before and after the DLTS scan. The results (Table 6-4, Figure 6-12 and 13) show that during the thermal scan (between 80 and 300 K), the J-V curve almost remains unchanged, which suggest that the DLTS scan between 77 and 300 K does not affect the J-V characteristics of the CIGS cell.

Table 6-1. Hall-effect results for the different Cd-partial-electrolyte treatment times on the CIGS samples

Samples	Hole density ( $\text{cm}^{-3}$ )	Hall mobility ( $\text{cm}^2/\text{V}\cdot\text{s}$ )	Resistivity ( $\Omega\text{-cm}$ )
No treatments	$5.3 \times 10^{15}$	8.89	133
Cd-dip (15 min)	$2.9 \times 10^{16}$	0.93	235
Cd-dip (15 min)	$4.3 \times 10^{16}$	1.54	94
Cd-dip (30 min)	$7.1 \times 10^{16}$	0.60	148

Note: The carrier conduction types for all CIGS samples tested are p-type assuming a uniform sample.

Table 6-2. Results from Hall-effect measurements for the CIGS samples

Sample #	Hole-concentration (#/cm <sup>-3</sup> )	Hall-mobility (cm <sup>2</sup> /V-s)	Resistivity ( $\Omega$ -cm)	Film type
A (NREL)	$5.3 \times 10^{15}$	8.9	133	<i>P-type</i>
B (EPV)	$2.6 \times 10^{14}$	20.5	1166	<i>P-type</i>
C (GSE)	$1.5 \times 10^{16}$	9.0	51	<i>P-type</i>
D (ISET)	$8.4 \times 10^{15}$	0.4	2046	<i>P-type</i>
E (SSI)	<i>N/A</i>	<i>N/A</i>	<i>N/A</i>	<i>N/A</i>
F (IEC)	<i>N/A</i>	<i>N/A</i>	<i>N/A</i>	<i>N/A</i>

Table 6-3. Hall measurement results for the CIS/CGS samples deposited on different substrates (GaAs/glass) by PMEE method

Samples	Carrier density ( $\text{cm}^{-3}$ )	Hall mobility ( $\text{cm}^2/\text{V}\cdot\text{s}$ )	Resistivity ( $\Omega\cdot\text{cm}$ )	Type of carriers
355-CGS/GaAs	$2.677 \times 10^{12}$	520.5991	4478.535	<i>Electrons</i>
354-CIS/GaAs	$3.795 \times 10^{10}$	5732.827	28965.06	<i>Electrons</i>
353-CGS/GaAs	$2.500 \times 10^{16}$	10.22044	24.42644	<i>Holes</i>
350-CIS/GaAs	$1.153 \times 10^{17}$	19.54468	1.384847	<i>Holes</i>
355-CGS/glass	$1.546 \times 10^{18}$	0.07958	50.68024	<i>Holes</i>
354-CIS/glass	$3.842 \times 10^{11}$	298.8994	54362.13	<i>Holes</i>
353-CGS/glass	$4.829 \times 10^{18}$	1.105717	1.168984	<i>Holes</i>
350-CIS/glass	$5.086 \times 10^{17}$	4.137745	2.966456	<i>Holes</i>

Table 6-4. Photo- J-V results for EPV CIGS device before and after DLTS scan

	Voc (v)	Jsc (mA/cm <sup>2</sup> )	F.F. (%)	Eff. (%)
Before DLTS	0.517	28.7	56.6246	8.4
After DLTS	0.51725	27.6	57.834	8.257

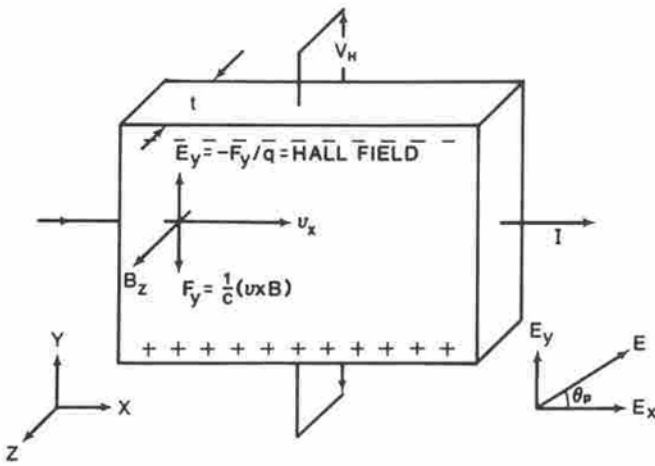


Figure 6-1. Schematic representation of the Hall effect sample.

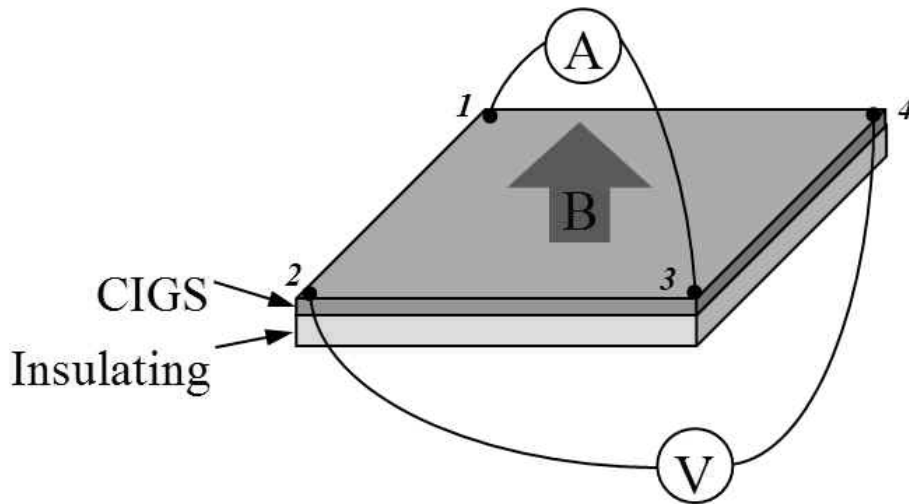


Figure 6-2. Typical four-point van der Pauw and Hall effect measurements.

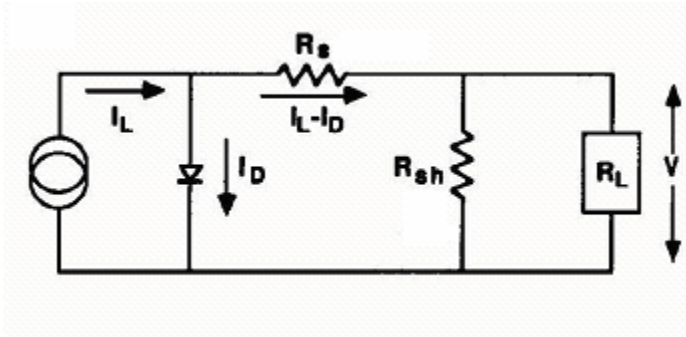


Figure 6-3. The equivalent circuit diagram of a CIGS PN junction solar cell.

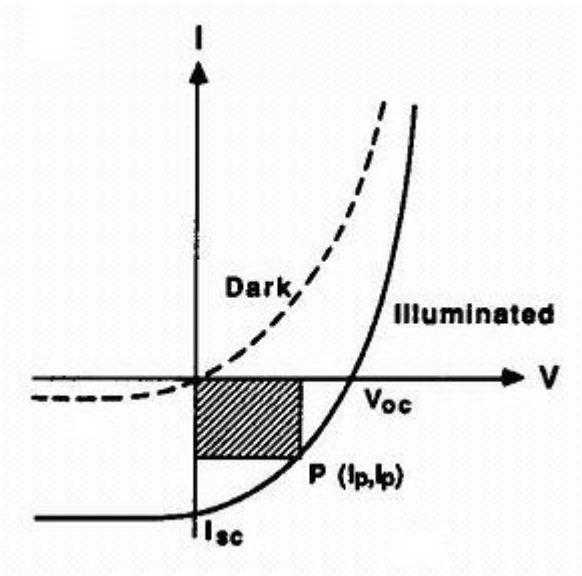


Figure 6-4. The I-V characteristics under dark and illumination conditions of a PN junction solar cell.

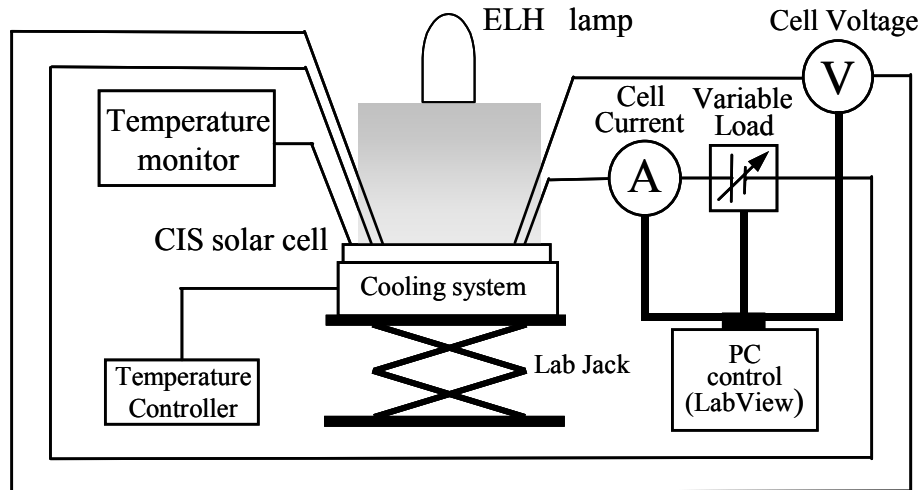


Figure 6-5. Apparatus and block diagram of I-V measurement system for the CIS-based cells.

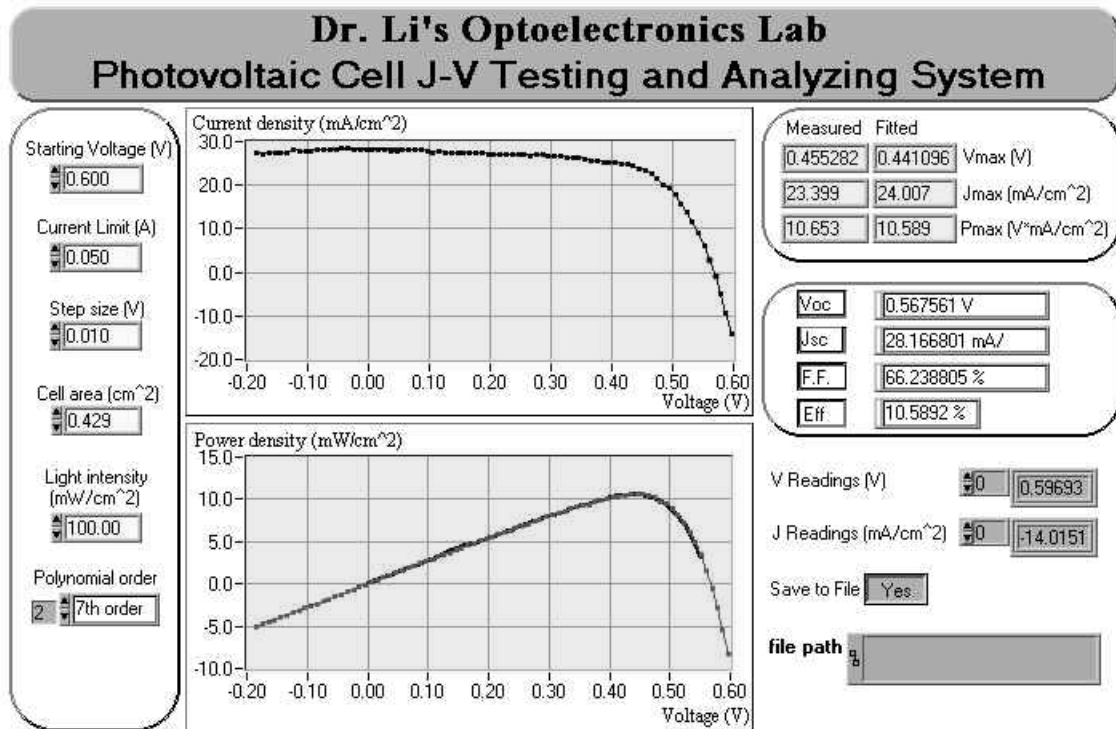


Figure 6-6. The photo- J-V measurement and analysis for solar cells using the *LabVIEW* program. (The tested CIGS solar cell is fabricated by EPV.)

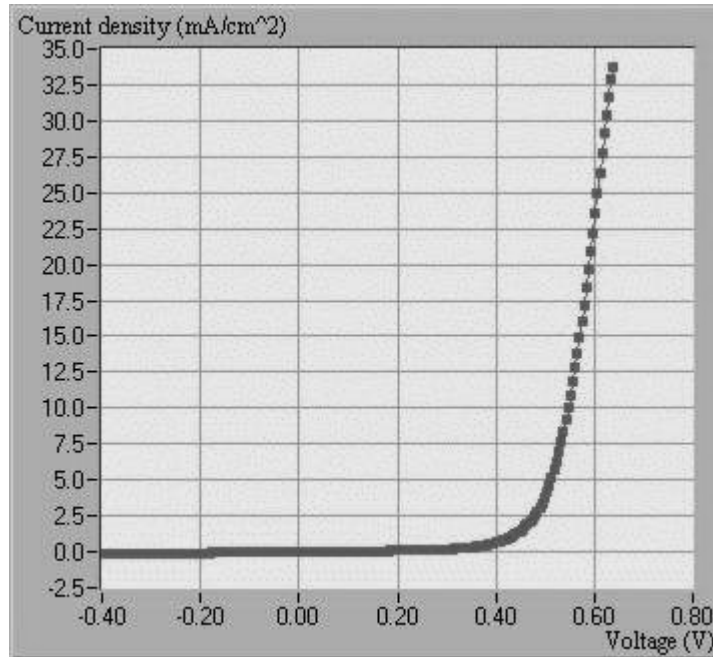


Figure 6-7. The dark-J-V measurement and analysis for solar cells using the *LabVIEW* program. (The tested CIGS solar cell is fabricated by NREL.)

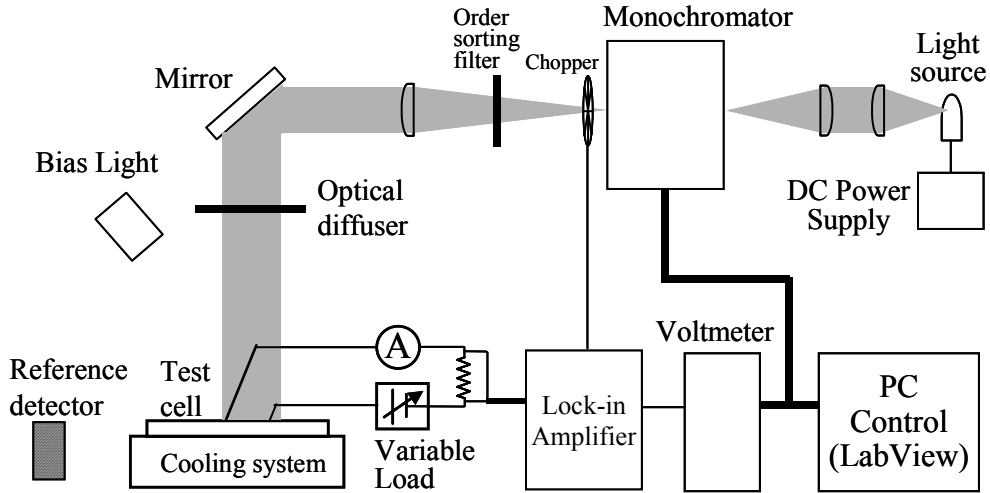


Figure 6-8. The block diagram of a spectral response measurement system for the CIS-based solar cells.

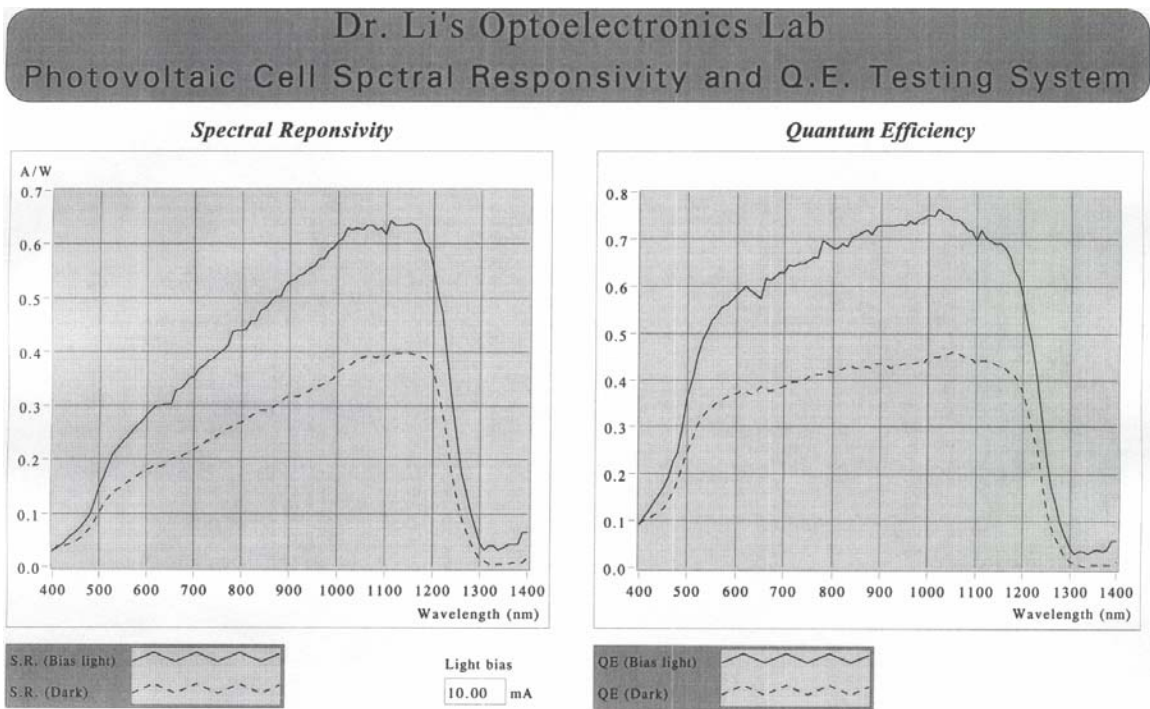


Figure 6-9. The spectral response and quantum efficiency measurements for solar cells using *LabVIEW* program. (The tested CIGS solar cell is fabricated by UF.)

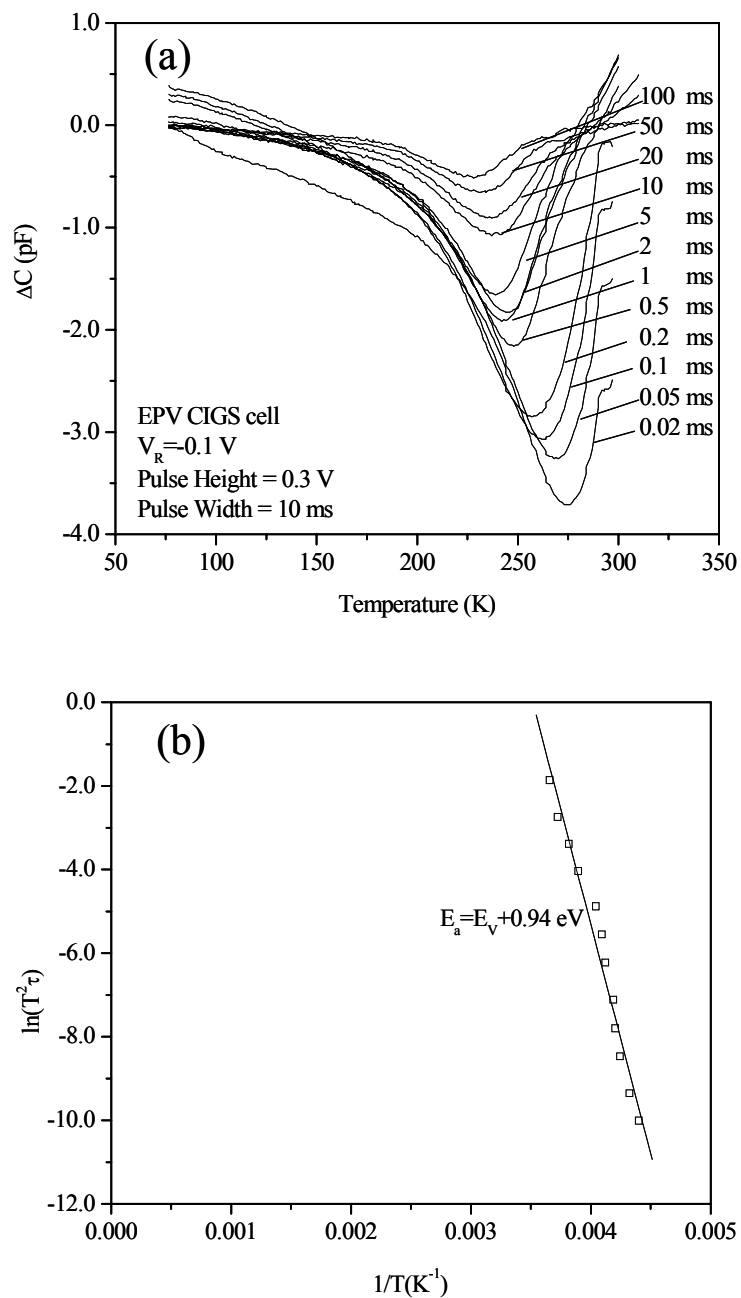


Figure 6-10. The DLTS scans for (a) EPV device at  $V_R = -0.1$  V,  $V_H = 0.3$  V, and  $W = 10$  ms. And (b) An Arrhenius plot obtained from the DLTS scans shown in (a).

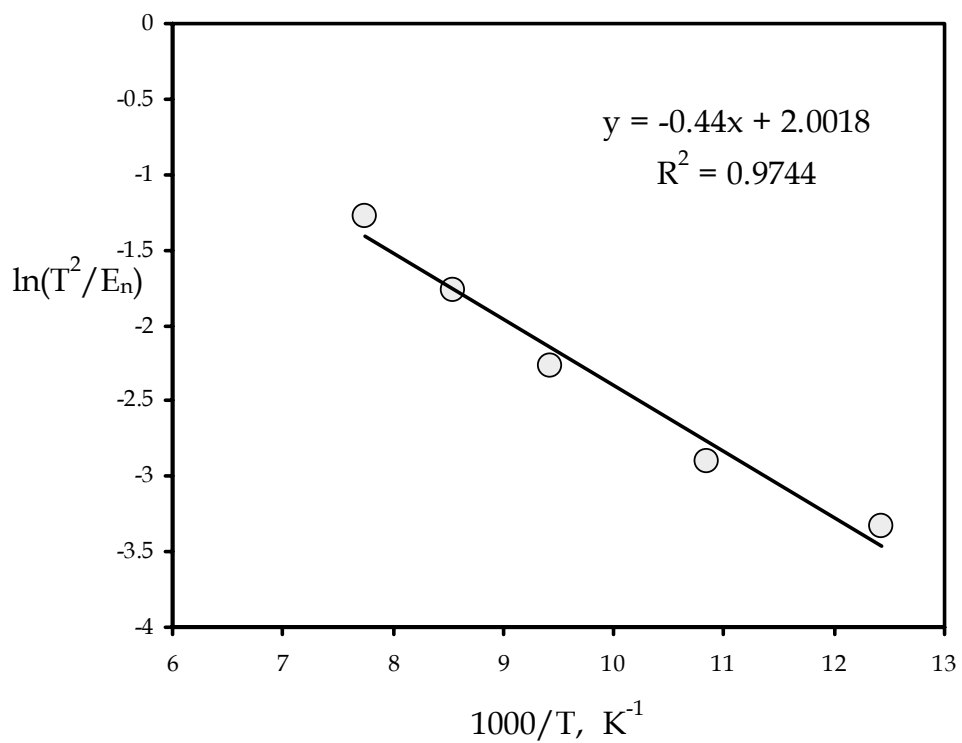
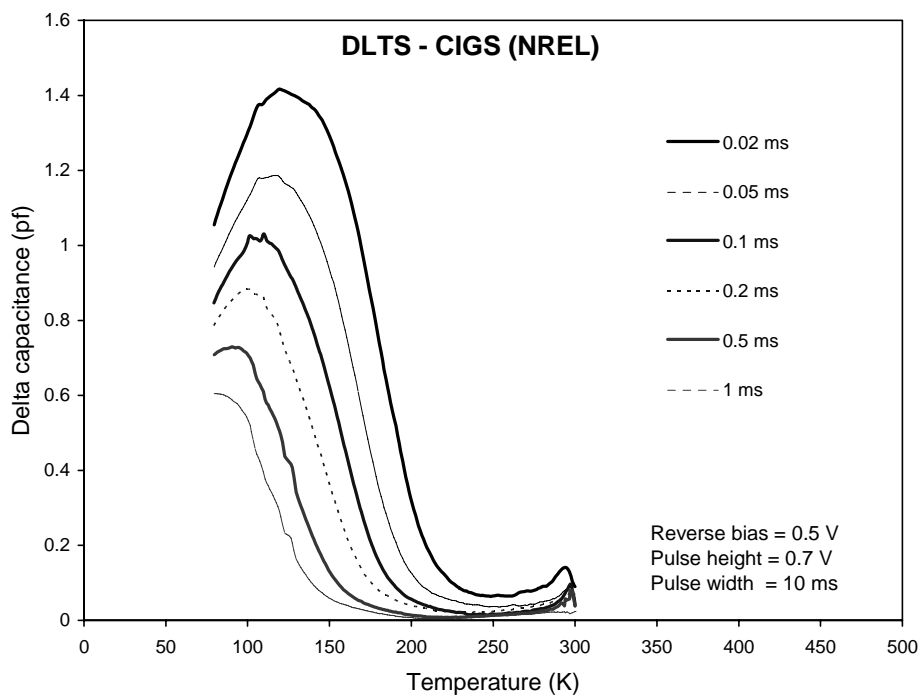


Figure 6-11. The DLTS scans for (a) EPV device at  $V_R = 0.5V$ ,  $V_H = 0.7V$ , and  $W = 10ms$ . And (b) An Arrhenius plot obtained from the DLTS scans shown in (a).

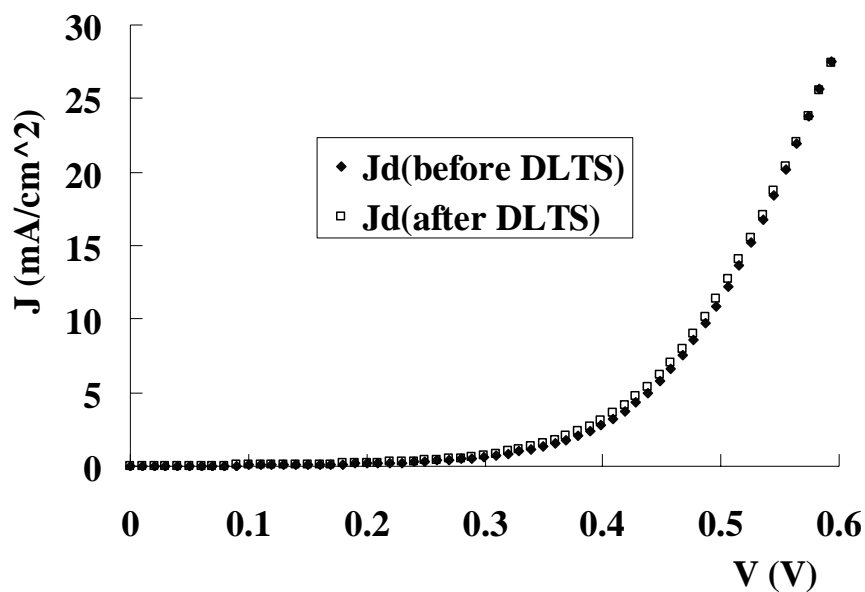


Figure 6-12. Dark- J-V curves of tested EPV CIGS device before and after DLTS measurement.

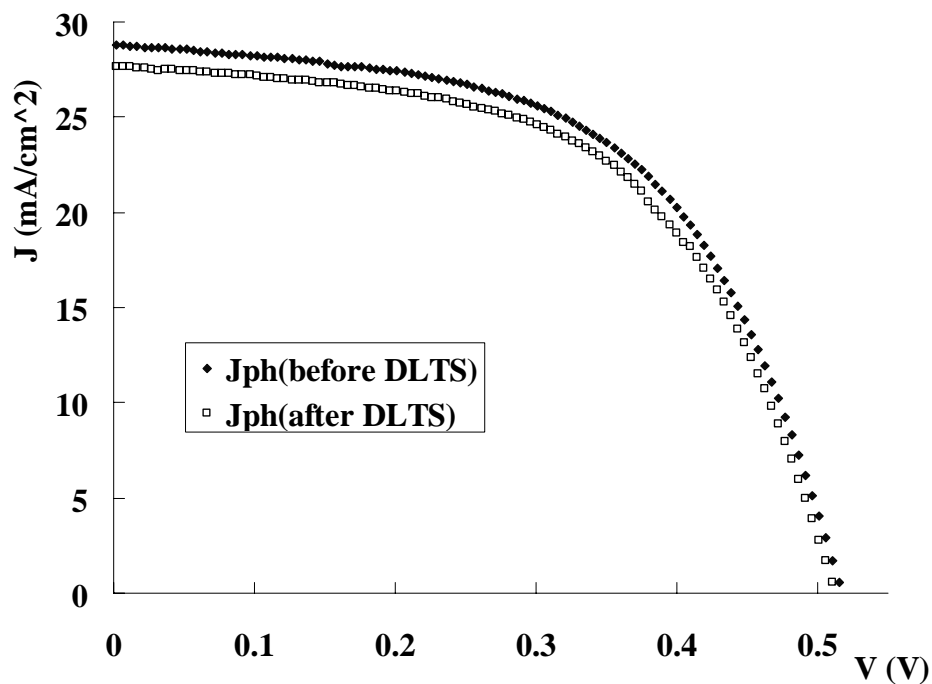


Figure 6-13. Photo- J-V curves of tested EPV CIGS device before and after DLTS measurements.

## CHAPTER 7 DEVICE MODELING AND SIMULATION OF CIGS SOLAR CELLS

In chapter 4, we discussed the RTA effects on CIGS solar cells, and the best result we obtained was from the first set of CIGS samples with progressive RTA treatments. Unfortunately the sample, which contains three CIGS cells, was destroyed after we applied 400°C RTA treatment. Therefore the only experimental data we have on these cells are the values of  $V_{oc}$ ,  $J_{sc}$ , F.F. and  $\eta$  measured before and after each progressive annealing up to 300°C. In order to extract other important parameters of these cells, the device modeling and simulation of these cells were carried out using the AMPS-1D (Analysis of Microelectronic and Photonic Structures) device simulation program [65]. The main objective of this study is to obtain the simulated defect density in the CIGS cells before and after each progressive annealing, and to extract the dark- J-V and Q-E curves, which we could not perform on the damaged cells experimentally.

### **Simulation Model of CIGS Solar Cell Devices**

It has been reported [66] that an In-rich n-type surface layer, which was identified as an ordered vacancy compound (OVC) and tentatively assigned as the stoichiometry  $CuIn_2Se_{3.5}$  or  $CuIn_3Se_5$ , exists between CdS buffer layer and CIGS absorber layer. A junction model was proposed that consists of a chalcopyrite/defect chalcopyrite heterojunction between the p-type bulk CIGS absorber and n-type OVC layers. The electrical characteristics of low hole mobility ( $\mu_p \leq 10 \text{ cm}^2/\text{V-s}$ ), high resistivity (105-106  $\Omega\text{cm}$ ), and low carrier densities ( $10^{11}$ - $10^{12} \text{ cm}^{-3}$ ) were proposed for the defect

chalcopyrite  $\text{Cu}(\text{In}_{1-x}\text{Ga}_x)_3\text{Se}_5$  materials for  $1 > x > 0$  [67]. Furthermore, the conductivity type changes from n- to p-type when the Ga content exceeds 30% [67].

The CIGS solar cell structure used in this simulation consists of a 155 nm ZnO ( $E_g = 3.3$  eV) TCO layer, a 51 nm CdS (2.4 eV) buffer layer; an ultra thin high-recombination interface layer (1.5 eV) with a high density of effective recombination centers is placed at the metallurgical junction between the CIGS surface layer and CdS buffer layer; an inverted surface layer (or OVC) with a thickness of 60nm, net carrier density  $n = 3 \times 10^{12} \text{ cm}^{-3}$ , band-gap energy,  $E_g = 1.3$  eV, is inserted between the CdS and CIGS layers, and an interfacial layer; and finally the CIGS absorber layer with band-gap energy  $E_g = 1.2$  eV ( $\text{CuIn}_{0.68}\text{Ga}_{0.32}\text{Se}$ ). The total thickness of the absorber layer is assumed equal to  $2 \mu\text{m}$  for all simulation cases in this study. The computer simulation tool AMPS-1D is employed by specifying the semiconductor parameters in each defined layer of the cell structure as input parameters in the simulation. In view of a limited knowledge of the semiconductor parameters in each layer and uncertainties in the interface and junction properties arising from possible interdiffusion and reaction during the cell processing, the division of the layers for the cell structure is limited to a simplified device structure as depicted above. The schematic energy band diagram under equilibrium condition for a typical CIGS/CdS/ZnO solar cell with a uniform band-gap is illustrated in Figure 7-1 [60]. Based on the Hall-effect results depicted in the previous chapters, some device parameters such as carrier mobility, carrier concentration were specified by using the experimental data. To proceed with the simulation, other unknown material parameters are reasonably employed according to some previous literatures.

The objective of this study is to analyze the trend in the performance of CIGS cells versus the defect density of the CIGS absorber layer, and to fit the experimental photo-J-V data by adjusting the defect density of the CIGS absorber layer and varying other parameters in a small range, finally backward extract the parameters and cells performance which we could not obtain from the damaged device experimentally.

### **Simulation Results of CIGS Solar Cells**

In this study, the defect density of CIGS absorber is varied from  $1 \times 10^{14} \text{ cm}^{-3}$  to  $1 \times 10^{19} \text{ cm}^{-3}$ , all other parameters are unchanged. The results (Table 7-1 and Figure 7-2) reveal that the cell performance is nearly unchanged for defect density below  $2 \times 10^{16} \text{ cm}^{-3}$ . Above this value, Voc, Jsc and conversion efficiency start dropping along with the increase of defect density, which suggests that to gain an optimal device performance, the defect density should be less than  $2 \times 10^{16} \text{ cm}^{-3}$ . It is also found that the defect density does not affect the fill factor in the simulations.

In chapter 4, we have discussed the effect of progressive RTA treatment on CIGS solar cells. Unfortunately the whole device was destroyed after we tried the  $400^\circ\text{C}$  RTA treatment. The only experimental data available for simulation is the photo- J-V parameters. In this chapter, an excellent fit of the experimental J-V data was obtained by our simulation. In the progressive RTA study, the most significant performance improvement occurs on cell#1, and other cells only showed a slight increase in the photo-J-V parameters (Table 4-1). Therefore, the simulation was focused on fitting the progressive RTA data in cell#1. In the simulations, some parameters (such as carrier mobilities and carrier concentrations) of CIGS absorber layer are set and varied based on the Hall-effect data listed in Table 4-3. By mainly adjusting the defect density along with varying other parameters such as carrier concentration of ZnO TCO layer and CdS buffer

layer in a small range, a good agreement between the experimental data and simulation results of cell#1 before and after progressive RTA was obtained (Table 7-2). The simulation results show that defect density of CIGS layer decreased from  $4 \times 10^{17}$  to  $1 \times 10^{16} \text{ cm}^{-3}$  after 3 consecutive progressive RTA treatments, which suggest that progressive RTA might be an effective treatment to reduce the defect density of CIGS solar cells. Figure 7-3 shows the photo- J-V curve of cell#1 before and after each progressive RTA treatment from the simulation results. To continue extract other important parameters, data of the dark current and spectral response were obtained from the simulation. From the dark- J-V curves (Figure 7-4), in the low bias region ( $V_a < 0.6 \text{ V}$ ) there is no difference of dark- J-V curves between data before and after each annealing. When the applied voltage is between 0.6 and 0.8 V, the dark- J-V curves after 200°C and 300°C were found to be slightly higher than data before RTA, and the dark- J-V after 100°C was similar as the curve before RTA. In the high bias region with applied voltage greater than 0.88 V, the dark- J-V curves after each progressive RTA were found to be apparently lower than data before RTA. These results suggest that RTA under certain annealing conditions can possibly reduce the defect density and hence decrease the recombination current through the device. The recovered Q-E curves (Figure 7-5) show explicitly higher photocurrent density after each progressive RTA than data before RTA. It is also noticeable that improvements in each progressive RTA treatment occur only for photon wavelengths longer than 650 nm, which suggests that the RTA treatment has positive effects on the CIGS absorber layer. It is not clear if RTA has any direct effect on the ZnO TCO layer and CdS and buffer layer. It should be noted that from the

simulation results we did not see any photocurrent improvement in the shorter wavelength region.

### **Conclusions**

In this chapter, simulation study of defect density versus CIGS device performance was conducted. Results show that cell performance start dropping with the increase of defect density from  $2 \times 10^{16} \text{ cm}^{-3}$ , and there is no strong relation between defect density and F.F. in the simulation. A well fitting of experimental progressive RTA data was also obtained by simulation, the results show that progressive RTA treatment can reduce the defect density in CIGS absorber layer and hence improve the photo- J-V, dark- J-V performance and spectral response of the device. Future effort will continue detailed study on effects of defect density on CIGS cells performance, and will correlate the simulation data and the experimental data from our previous annealing study.

Table 7-1. Performance parameters of the CIGS ( $E_g=1.2$  eV) solar cells versus the defect density in the CIGS absorber layer.

Defect density ( $\text{cm}^{-3}$ )	Jsc ( $\text{mA}/\text{cm}^2$ )	Eff. (%)	F.F.	Voc (V)
$1 \times 10^{14}$	30.434	14.699	0.734	0.658
$2 \times 10^{14}$	30.433	14.699	0.734	0.658
$5 \times 10^{14}$	30.431	14.698	0.734	0.658
$1 \times 10^{15}$	30.427	14.695	0.734	0.658
$2 \times 10^{15}$	30.420	14.691	0.734	0.658
$5 \times 10^{15}$	30.399	14.678	0.734	0.657
$1 \times 10^{16}$	30.366	14.657	0.734	0.657
$2 \times 10^{16}$	30.303	14.617	0.734	0.657
$5 \times 10^{16}$	30.148	14.518	0.734	0.656
$1 \times 10^{17}$	29.958	14.393	0.734	0.655
$2 \times 10^{17}$	29.718	14.226	0.733	0.653
$5 \times 10^{17}$	29.396	13.970	0.733	0.648
$1 \times 10^{18}$	29.205	13.755	0.733	0.643
$2 \times 10^{18}$	29.076	13.583	0.734	0.636
$5 \times 10^{18}$	28.977	13.314	0.736	0.624
$1 \times 10^{19}$	28.937	13.073	0.737	0.613

Table 7-2. Photo- J-V data of cell#1 before and after progressive RTA treatment (From experiment and AMPS 1D simulation results)

	Before	100°C	200°C	300°C
Voc (V)*	0.628 / 0.6282	0.633 / 0.6331	0.652 / 0.6525	0.627 / 0.6318
Jsc (mA/cm <sup>2</sup> )*	31.66 / 31.64	34.30 / 34.30	34.85 / 34.796	35.39 / 35.392
F.F. (%)*	47.88 / 46.8	56.81 / 56.8	68.43 / 68.2	71.05 / 71.5
Eff. (%)*	9.520 / 9.647	12.32 / 12.276	15.55 / 15.409	15.77 / 15.763
Defect density **	$4 \times 10^{17} \text{ cm}^{-3}$	$1 \times 10^{17} \text{ cm}^{-3}$	$3 \times 10^{16} \text{ cm}^{-3}$	$1 \times 10^{16} \text{ cm}^{-3}$

\* Data obtained from experiment / simulation

\*\* Data obtained from simulation only

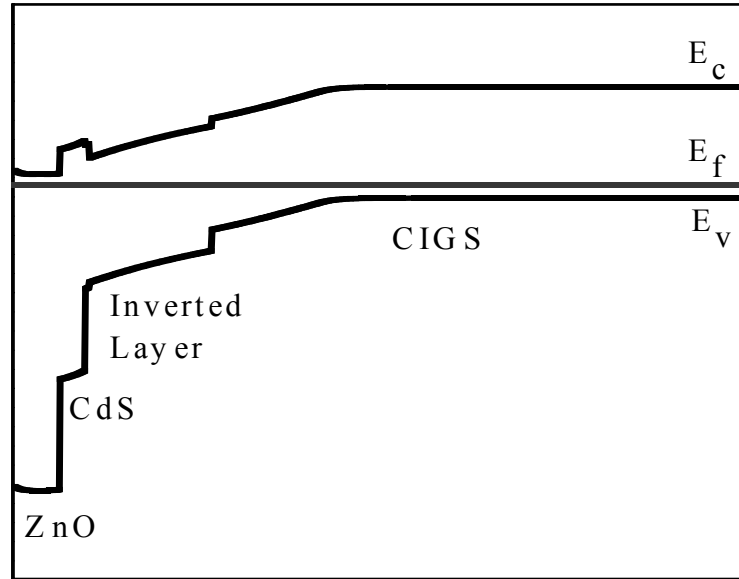


Figure 7-1. The schematic energy band diagram of a typical ZnO/CdS/CIGS solar cell under equilibrium condition.

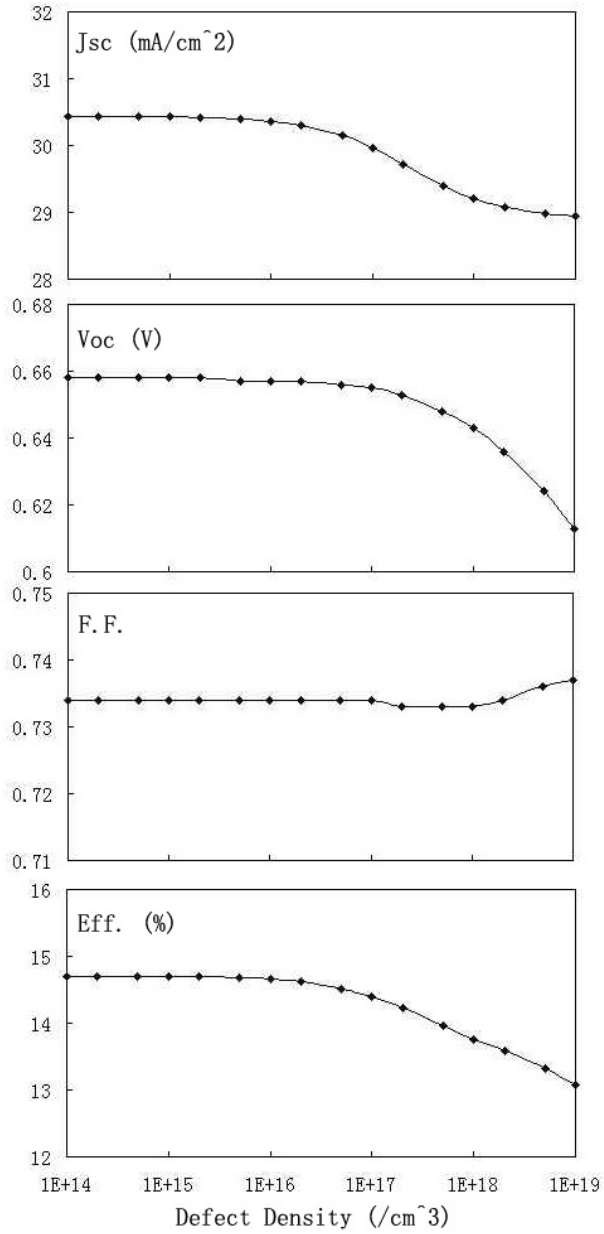


Figure 7-2. Performance parameters of CIGS ( $E_g=1.2\text{eV}$ ) solar cells versus the defect density of CIGS absorber layer.

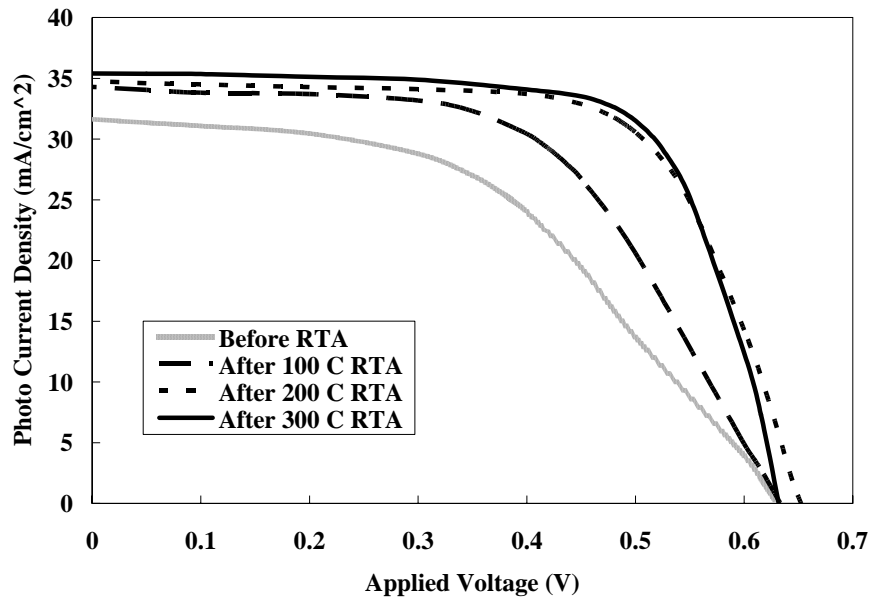


Figure 7-3. Photo- J-V curves of cell#1 before and after progressive RTA treatment (From AMPS 1D simulation results).

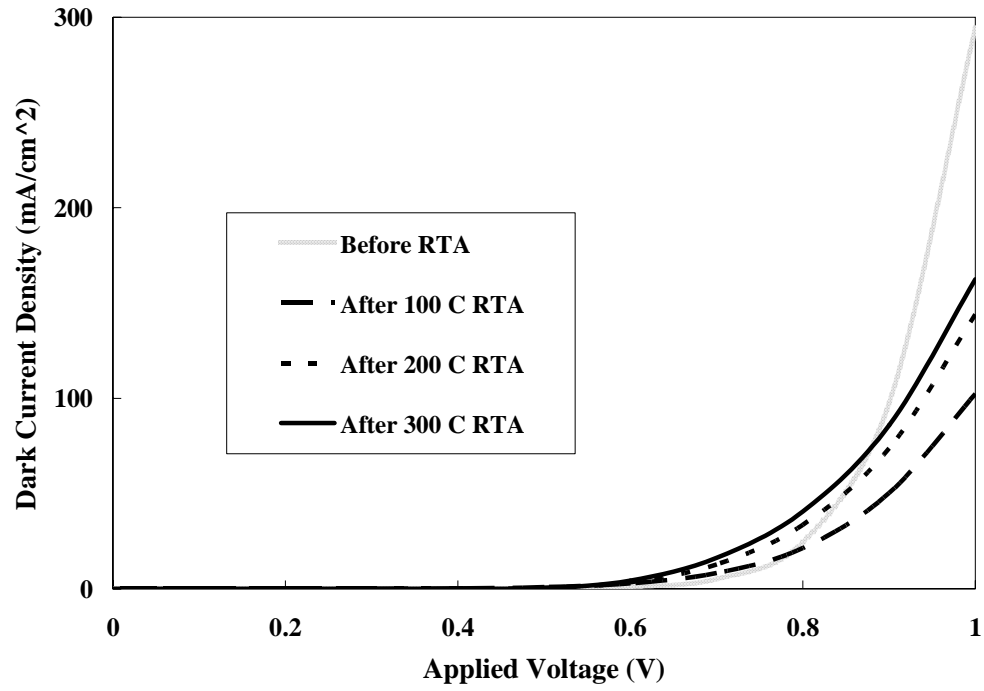


Figure 7-4. Dark- J-V curves of cell#1 before and after progressive RTA treatment (From AMPS 1D simulation results).

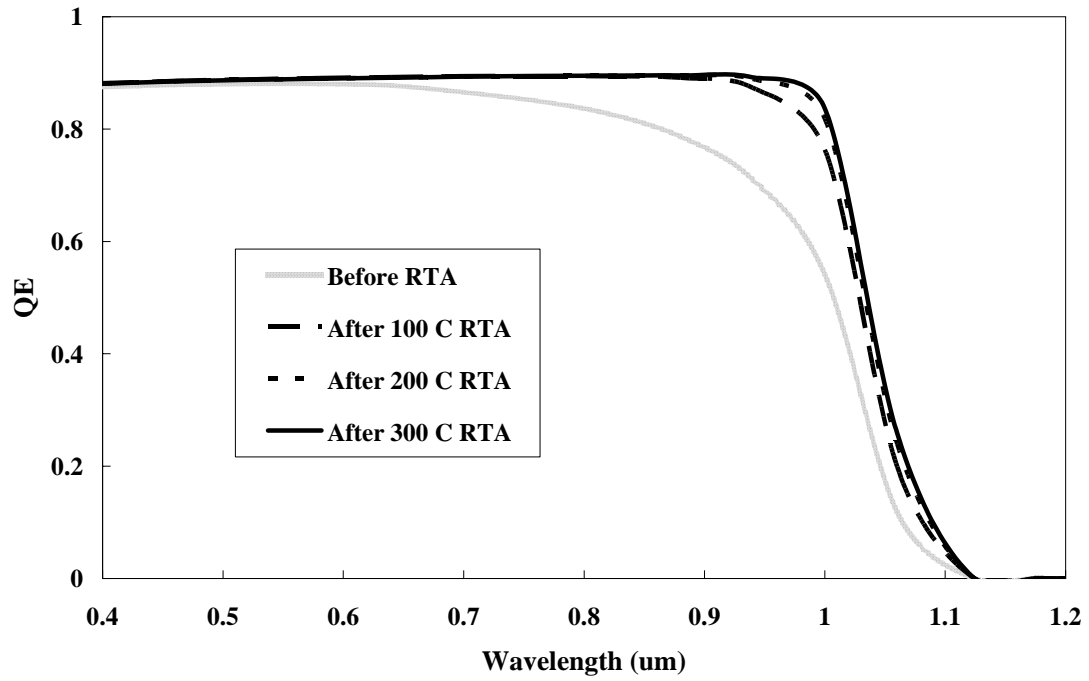


Figure 7-5. Quantum efficiency of cell#1 before and after progressive RTA treatment (From AMPS 1D simulation results).

## CHAPTER 8 RADIATION EFFECTS ON CIGS FILM AND SOLAR CELLS

One of the most promising applications of thin film solar cells is to work in the outer space. Therefore it is very important to investigate the radiation tolerance of CIGS solar cell material. In this chapter, our research focuses on advancing the understanding of radiation effects on  $\text{CuInGaSe}_2$  films and devices.

### **Introduction**

Two main areas of interest focus on the displacement effects and enhanced low dose rate sensitivity (ELDRS) in devices with only a few atomic layers controlling the basic device physics. Displacement damage at ohmic contact interfaces may be more sensitive to degradation mechanisms caused by ionizing radiation than device junctions. Similarly, the fundamental mechanisms underlying ELDRS may be revealed and controlled at these reduced dimensions.

The usually accepted view is that displacement damage is proportional to the non-ionizing energy loss (NIEL defined in units of  $\text{keVcm}^2/\text{g}$ ) or with higher energies by the displacement cross-section ( $D$  in  $\text{MeVmb}$ ). It is unclear if the NIEL hypothesis (more general than non-impurity divacancies) can be used to relate damage because of different particles and energies in reduced scale photovoltaic devices. UF has excellent capabilities for in-situ electrical and elevated temperature irradiations. This study on the radiation induced damage in  $\text{CuInGaSe}_2$  solar cells utilizes irradiations performed unbiased at room temperature. This method is an acceptable simplified experimental procedure for conducting such a study.

**ELDRS Effects**

The ELDRS effect is normally associated with linear devices having junction isolated bipolar transistors (and is not a part of this work). Detailed characterization of point defects, defect clusters, interstitials and electrical active traps offers a valuable insight leading to a better understanding of the basic degradation mechanism. Future opportunities are envisioned with ultra-thin boundaries between materials of widely differing atomic number (copper interconnects, high impedance bonds, complex metallized layers, etc.). These may be sensitive to dose-enhancement under electron or bremsstrahlung irradiation.

**Total Dose Effects**

Total dose effects in semiconductor devices depend on the creation of electron-hole pairs within dielectric layers (oxides, nitrides etc.) and subsequent generation of traps at or near the interface with the semiconductor or of trapped charge in the dielectric. This can produce a variety of device effects such as flat-band and threshold voltage shifts and surface leakage currents.

There is an extensive literature on total dose effects. One of the most recent and detailed reviews has been given by Dressendorfer in his 1998 NSREC Short Course Notes [68].

Although the concept of total ionizing dose is a useful first order approximation for quantifying effects there are dependencies on a number of other parameters. Notably, the linear energy transfer (energy deposited per unit path length) of the radiation and the applied electric field both influence the rate of recombination of electron-hole pairs, while the dose-rate influences the relative importance of hole traps and interface states. These are extensively discussed in [68]. Strictly dose should be defined in relationship to

the material affected. This is commonly the silicon dioxide rather than silicon. Giving average doses in a device can lead to significant errors because of dose enhancement effects at boundaries.

The basic mechanisms of total dose effects continue to be a matter of research but it is now well established that hydrogen (i.e., proton) plays an important role [69]. In recent years considerable effort has been directed to processing optimizations to 'harden' the dielectric materials (usually silicon dioxide). With the trend towards thinner oxides, attention has shifted to the removal of 'parasitic' leakage paths in the thicker field oxides. This can often be achieved 'by design' so that, provided a circuit is designed using cells from a radiation tolerant library, performance can be guaranteed regardless of the particular foundry used. However the device scaling which results in thinner oxides also leads to microdosimetry effects where the total dose deposited by single energetic ions can cause permanent effects such as stuck bits in memories [70] or permanent damage to CMOS readout circuits for imagers [71].

In ultra-thin oxides new phenomena such as radiation induced leakage current (RILC) are becoming apparent - because of mechanisms such as trap assisted tunneling. Also the trend to nitrided oxides (to suppress hot carrier effects) has implications for radiation tolerance [72].

### **Displacement Damage**

Energetic particles such as neutrons, protons, electrons,  $\alpha$ -particles and heavy ions can create damage in semiconductor materials by displacing atoms in the crystal lattice. Secondary electrons produced by high-energy photons will also produce displacement effects. The result is that stable defect states are created within the bandgap that can give

rise to any of the five effects (Figure 8-1), depending on the temperature, carrier concentration and the location at which the defect resides.

- Generation of electron-hole pairs (leading to thermal dark current in detectors)
- Recombination of electron-hole pairs (leading to reduction of minority carrier lifetime and effects in LEDs and laser diodes)
- Trapping of carriers, leading to loss in charge transfer efficiency in CCDs (minority carrier trapping) or carrier removal (majority carrier trapping)
- Compensation of donors or acceptors, also leading to carrier removal in some devices (for example the resistance in a lightly doped collector in a bipolar transistor can increase)
- Tunneling of carriers, leading to increased current in reverse biased junctions - particularly for small bandgap materials and high electric fields

Displacement damage is proportional to the non-ionizing energy loss, NIEL (usually defined in units of  $\text{keVcm}^2/\text{g}$ , though in high energy physics the displacement damage cross section (D) in  $\text{MeVmb}$  is usually used). The NIEL hypothesis can be used to relate damage because of different particles and energies - this greatly reduces the amount of testing needed (usually only one particle and energy, e.g. 10MeV proton, is used). The NIEL scaling hypothesis leads to the concept of displacement damage equivalent dose (=NIEL x particle fluence) [73]. This can be measured in  $\text{keV/g}$  or in (non-ionizing) rads.

Displacement damage does not depend significantly on irradiation bias or temperature, hence irradiations can be performed unbiased at room temperature - this simplifies experimental procedures. These assumptions appear to be adequate for many cases. However when the exact nature of the defect is important then damage may not always scale with NIEL. Such an exception has been discussed by Dressendorfer [68] (in that case the difference between diffusion length damage in n- and p-type silicon solar

cells). Another case has recently emerged in the field of high energy physics where neutron and proton effects in oxygen doped silicon microstrip detectors have been found to differ. The reasons for this probably lie in the differences in damage clustering (and subsequent defect kinetics) between different particle types and energies.

It is now well established that the amount of formation of defect clusters depends on the particle type. Electron irradiation gives primary knock-on atoms (PKAs) with low recoil energies and hence leads to almost exclusive production of point defects; whereas neutrons give a flat PKA spectrum and a much greater proportion of cluster formation. For protons the situation is in between. In some cases the amount of clustering may not matter, only the total number of defects. However the clustering can be expected to affect the defect kinetics. Recent work by Watts suggests that when impurity related defects (e.g. the E-centre) are involved then NIEL scaling may not always be strictly valid. The implication for space instrumentation is that tests at a single proton energy may not allow an accurate prediction in all cases. Fortunately there are still many cases where the NIEL hypothesis is valid, in particular where non-impurity related defects, such as divacancies are involved. Recently Srour [74] has suggested a universal damage factor for the displacement-damage-induced dark current in silicon devices. This suggests a common defect such as the divacancy is involved, and it is seen that NIEL scaling is effective.

Other factors, which can affect the generation of defects, are the irradiation temperature and post-irradiation annealing. Usually it is assumed that neither irradiation temperature nor bias has an important effect and that annealing at room temperature takes place in only the first few weeks after irradiation. However, this has not been studied in

detail for situations (such as CCDs at low temperature) where the details of the defect kinetics may be important.

Although the largest body of displacement damage results applies to silicon devices, effects in other semiconductors are becoming increasingly important, particularly for photonics devices involving materials such as GaAs, InP and SiGe. Prediction of the NIEL for advanced materials is therefore an important topic, especially as some devices (such as optocouplers, amphoterically doped and single-heterojunction LEDs) are especially vulnerable in orbits subjected to intense proton fluxes. A simple technique for predicting NIEL using the SRIM code has been discussed recently [75]. However this does not include nuclear reactions, which are important at high energies. Note that discrepancies between the measured and predicted high energy NIEL for GaAs devices have been actively discussed in recent years and the issue is not yet fully resolved.

As for silicon devices, it is well known that imaging devices, such as CCDs and CMOS active pixel sensors, show dark current spikes because of displacement damage. These are individual pixels with higher than average dark current. The dark current non-uniformity then depends not only on the average NIEL but also on its variance (as recently reviewed by Robbins [76]). In fact there are cases where a detailed Monte Carlo simulation of the damage cascades is necessary - e.g. when interactions of high-energy protons within small depletion volumes have to be considered.

Displacement damage in linear devices (such as operational amplifiers) has recently been discovered to be a potentially important phenomenon, making prediction of displacement effects important.

## High-K Dielectrics

Another area of new technology is the use of high-K dielectrics (i.e. materials with a high dielectric constant) and copper interconnections.

Total ionizing dose can also influence materials properties. For example transparent materials, such as cover glasses, can become opaque via the population of color centers, while plastic materials can become embrittled. Radiation-induced conductivity is an important phenomenon in mitigating charging of dielectric materials. In general, the important issues for total dose effects include the following parts.

- Dependence on bias during irradiation (irradiation whilst the device is biased is usually the worst case).
- Annealing effects (trapped charge reduces after irradiation, while interface traps tend to build-up).
- Dependence on dose rate (mainly because of annealing effects)
- Dependence on package and burn-in (especially for some types of plastic package)
- Variability from batch to batch and device to device (especially for commercial-off-the-shelf devices)
- In linear devices with junction isolated bipolar transistors there is a pronounced "enhanced low dose rate sensitivity" (ELDRS) effect where the damage is greater at low dose rates.
- Of relevance to potential work under this project is the problem of dose-enhancement under electron or bremsstrahlung irradiation where there are boundaries between materials of widely differing atomic number. These can occur in packaging and shielding as well as on the die (e.g. copper interconnects, high-Z bump bonds, metallized layers, Au-Si die attachments). Enhancement factors can approach a factor two.

### Experimental Details and Discussion

The gamma rays from cobalt-63 (1.17 & 1.33MeV) are above the pair production threshold energy. This is shown in the gamma absorption cross-section graph (Figure 8-2). The predominant interactions of photon with the lattice are shown in the photon

interaction probabilities (Figure 8-3). While the gamma rays are not capable of displacement damage directly, the hot electrons they create do have the ability to do this. The electron in most materials requires less than 30 eV to join in the conduction process if within a diffusion length of the space charge region in p-n junctions. Increased leakage currents, decreased gains and trapped charges in oxides are some of the common results of radiation damage. However in this study, our intent is to analyze the radiation tolerances of CIGS materials by characterizing films surface morphology and devices performance before and after irradiation. By mounting four CIGS films/devices with difference distance from the radiation source, the radiation dose is determined by use of a radio chromatic film and measuring its change in optical density. Total dose is extrapolated using time and information from a calibration exposure of  $\sim 1$  Mrad (Si).

In this study, 4 identical CIGS films and 4 CIGS devices were irradiated with 4 different dose rates. There is one extra CIGS sample (absorber only) served as the control sample for the surface comparison of the irradiated samples. Table 8-1 lists the dose rate and total dose of the tested samples and devices. Photo- J-V measurements were taken for the 4 irradiated devices before and after the radiation treatment. There is an explicit surface color change and fade of the metal contact on each device after irradiation. Unfortunately all the irradiated devices showed a linear J-V curve after radiation even new metal contacts were deposited. For the irradiated CIGS samples (absorber layer only), the surface color also changed dramatically and the color changed area becomes larger as the total dose of sample received goes higher, as one can see from the photograph (Figure 8-4), the dark area increased along with the increase of the total dose. XRD measurements were taken in order to analyze the change of the film composition

and crystallinity by radiation. From the XRD results (Figure 8-5) of 4 irradiated CIGS samples and the control sample, there is no new peak observed among the irradiated samples in comparison to that of the control sample in the XRD plots, indicating that the film composition remains unchanged after radiation. By close looking at each CIGS peak, we found a slight decrease of peak heights (XRD counts, from #5 down to #1) as we increase the total dose of radiation on the samples, indicating that the crystallinity of CIGS sample becomes poor once the radiation dose goes higher.

Because of the strong J-V performance drop in the previous experiment, a new set of radiation experiment was carried out on 2 CIGS devices (from GSE and SSI) with much lower total dose. Two cells on each device were measured by photo- J-V system before and after irradiation. From the radiation condition and Photo- J-V results/curves (Table 8-2, Figure 8-6, to 8-9) of each cell before and after radiation, for the 2 tested cells of GSE CIGS device (#1) with total received dose of 2.12 Mrads (Si), we found a explicit increase of  $V_{oc}$ , F.F. and  $\eta$  after radiation, while a decrease of  $J_{sc}$  was also observed. For the 2 tested cells of SSI CIGS device (#2) irradiated with total received dose of 6.5 Mrads (Si), only  $V_{oc}$  was improved after radiation, all other parameters:  $J_{sc}$ , F.F. and  $\eta$  has strong decrease after radiation, indicating that CIGS solar cells performance could possibly be improved by Gamma-ray radiation under low dose condition (2.12 Mrads) and 6.5 Mrads or higher radiation dose could probably damage the solar cell and hence cause the performance drop. These results suggest that the estimated threshold of the total radiation dose in this radiation tolerance study should be some point between 2.12 and 6.5 Mrads to remain the device performance un-dropped.

Our future effort will focus on detailed study of effects of low dose Gamma-ray radiation on CIGS solar cells, as well as to find the accurate radiation dose threshold in our future radiation tolerance study on CIGS materials.

Table 8-1. Dose rate and total dose of the tested CIGS samples and devices

Sample/device #	Dose rate (Krad(Si)/hr)	Total dose (Mrads(Si))
1	82.0	61
2	65.8	49
3	61.7	46
4	44.2	33
5 (control sample)	N/A	N/A

Table 8-2. Dose conditions and Photo- J-V results of CIGS devices before and after radiation

Device #	#1 (cell#1)	#1 (cell#2)	#2 (cell#1)	#2 (cell#2)
Dose (Mrads)	2.12	2.12	6.5	6.5
Voc (V)*	0.501 / 0.538	0.505 / 0.538	0.495 / 0.566	0.498 / 0.562
Jsc (mA/cm <sup>2</sup> )*	28.89 / 27.83	29.12 / 25.89	34.51 / 27.60	33.36 / 20.25
F.F. (%)*	47.12 / 63.55	46.33 / 63.03	45.46 / 44.30	46.15 / 43.37
Eff. (%)*	6.823 / 9.639	6.818 / 8.778	7.767 / 6.918	7.671 / 6.215

\* Data taken before / after radiation

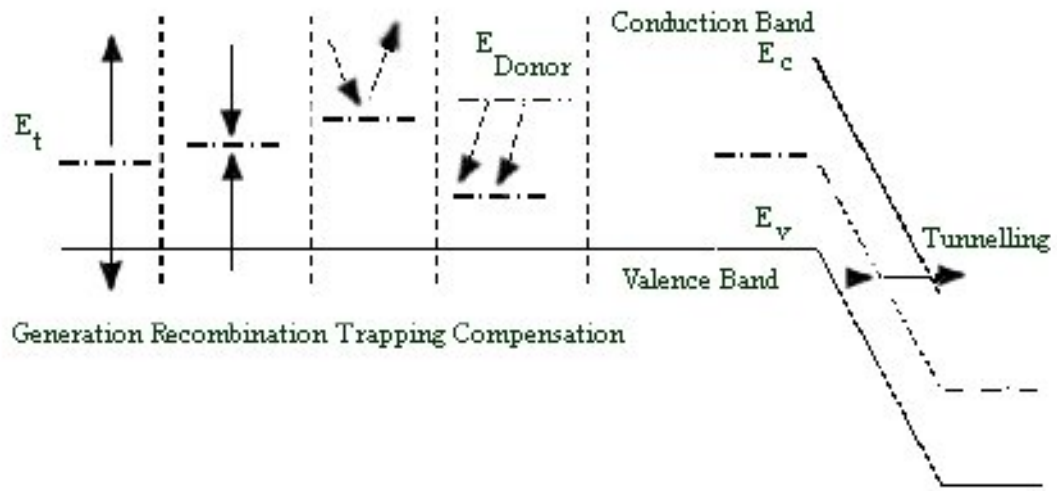


Figure 8-1. Five basic effects of a defect energy level ( $E_t$ ) on the electrical performance of a device.

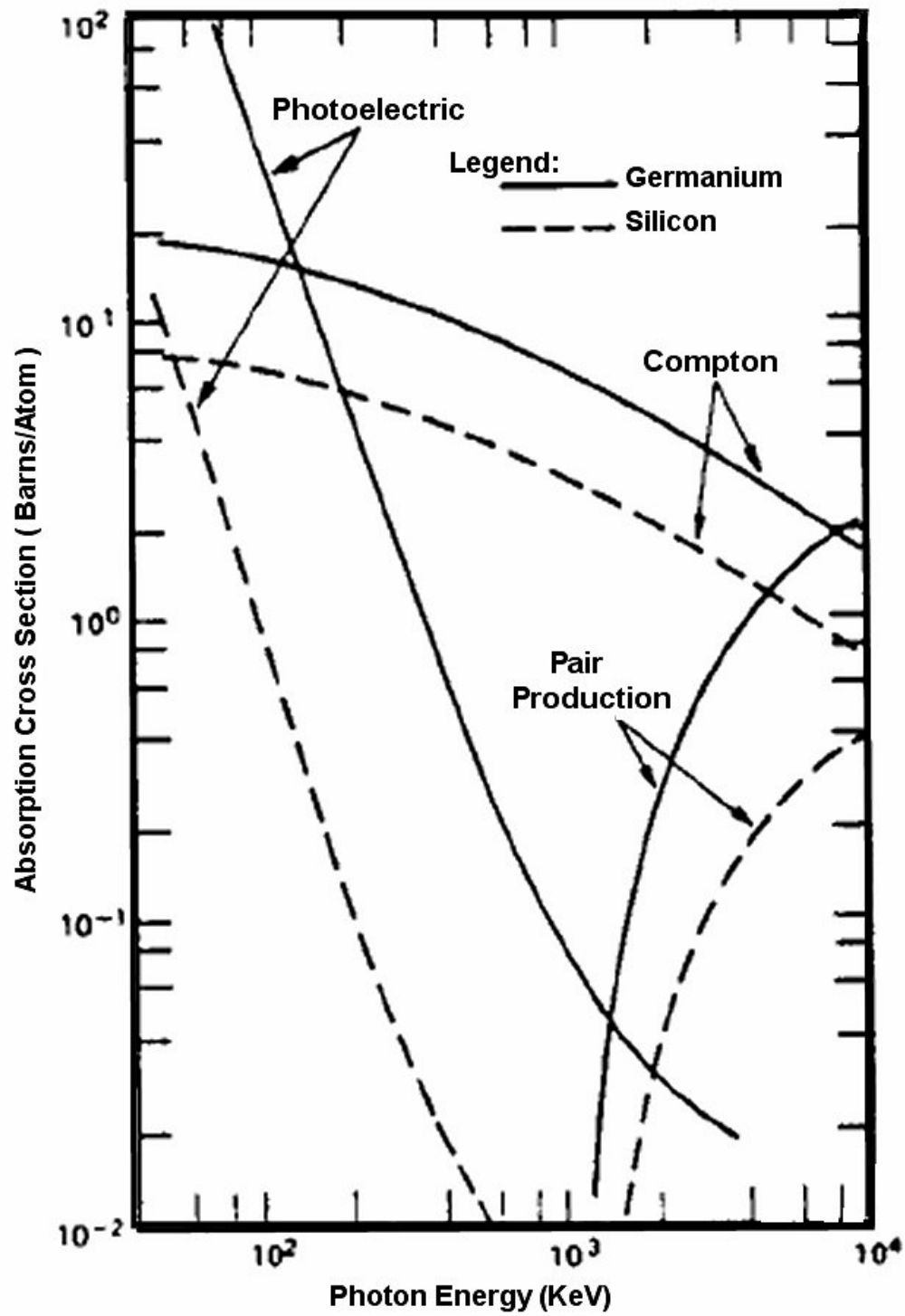


Figure 8-2. Gamma absorption cross-section versus photon energy.

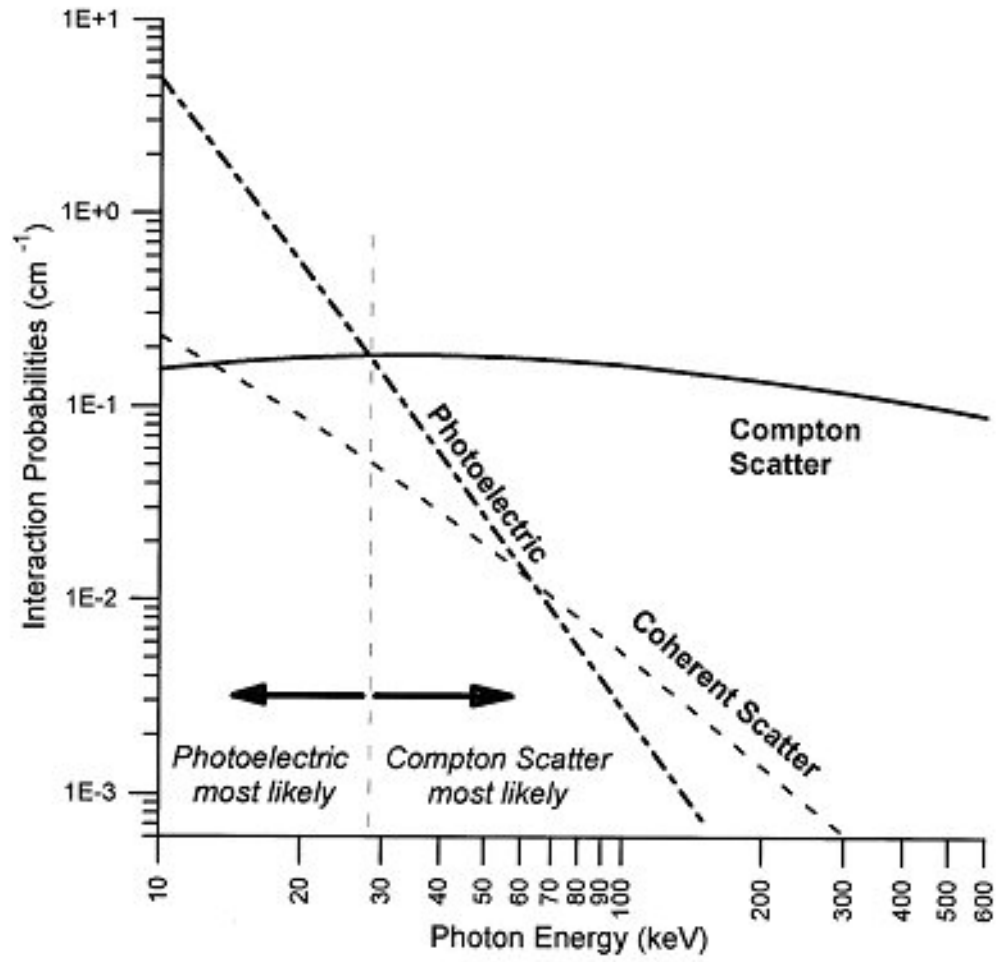


Figure 8-3. Photon interaction probabilities versus photon energy.

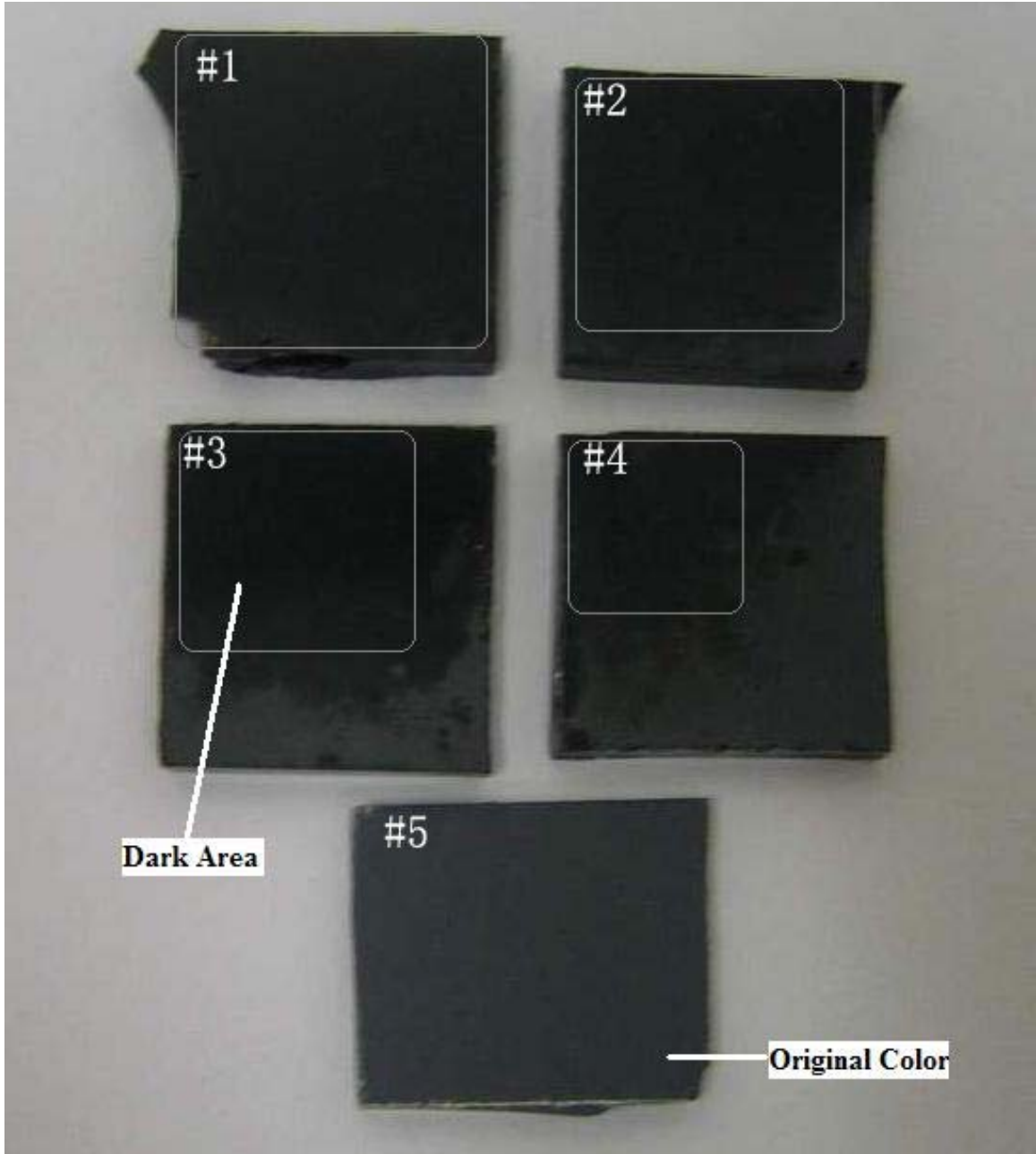


Figure 8-4. Photograph of irradiated CIGS films and the control film.

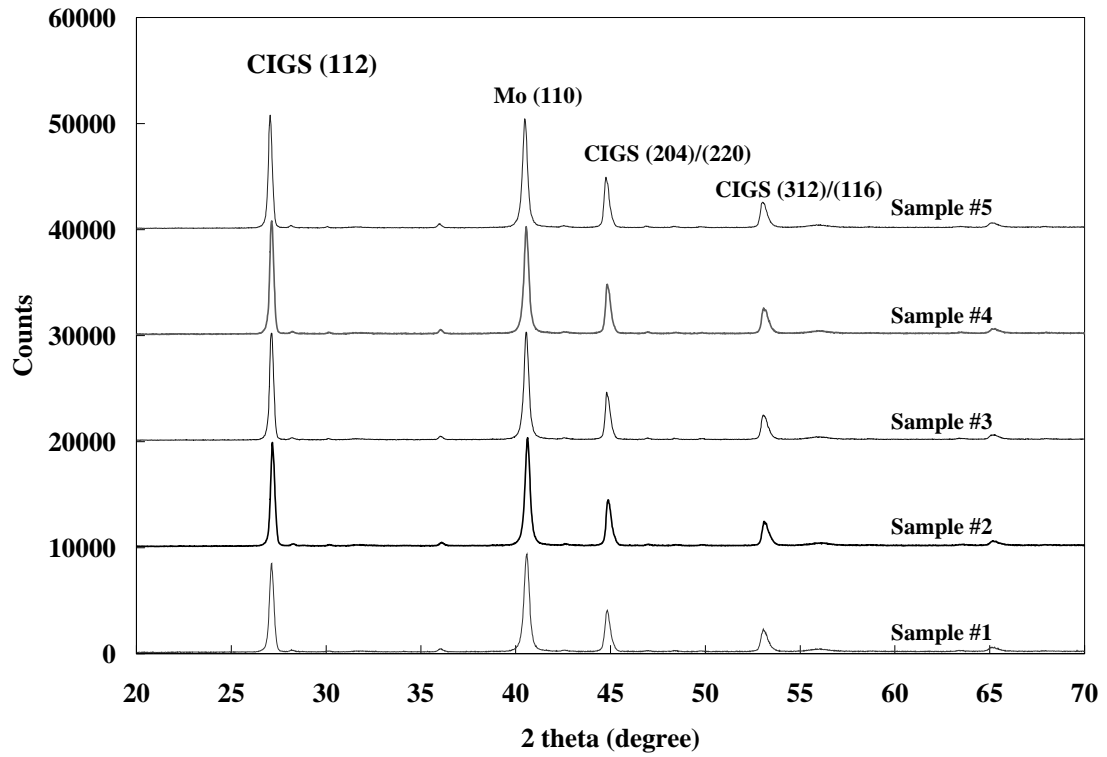


Figure 8-5. The XRD results of irradiated CIGS samples (#1-4) and the control sample (#5).

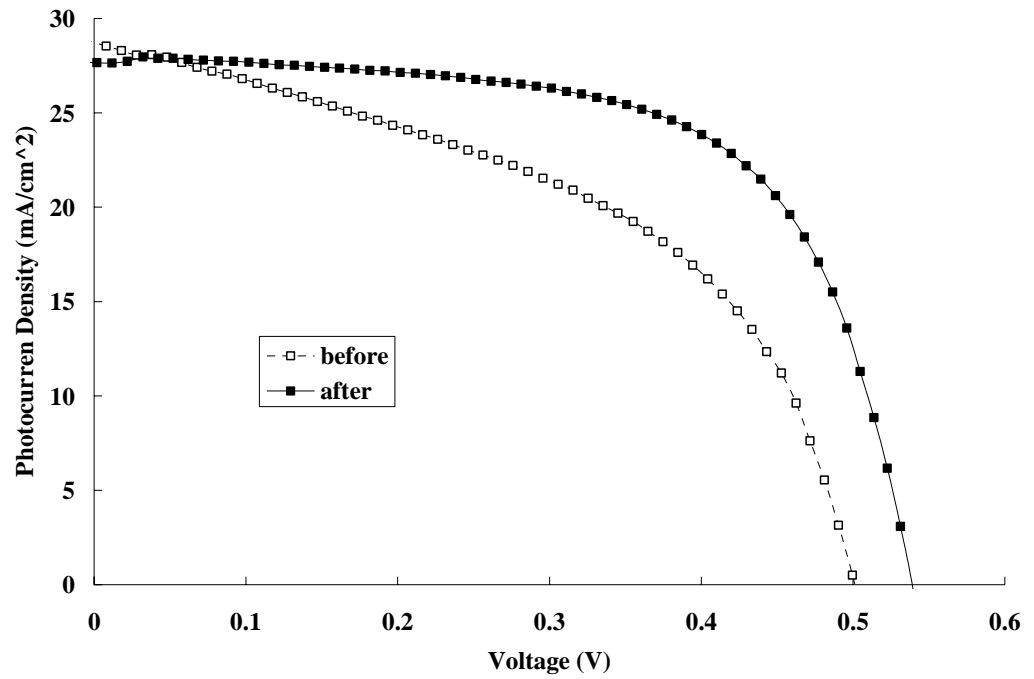


Figure 8-6. Photo- J-V results of CIGS device #1 (cell#1) before and after total dose of 2.12 Mrads (Si) radiation (Device from GSE).

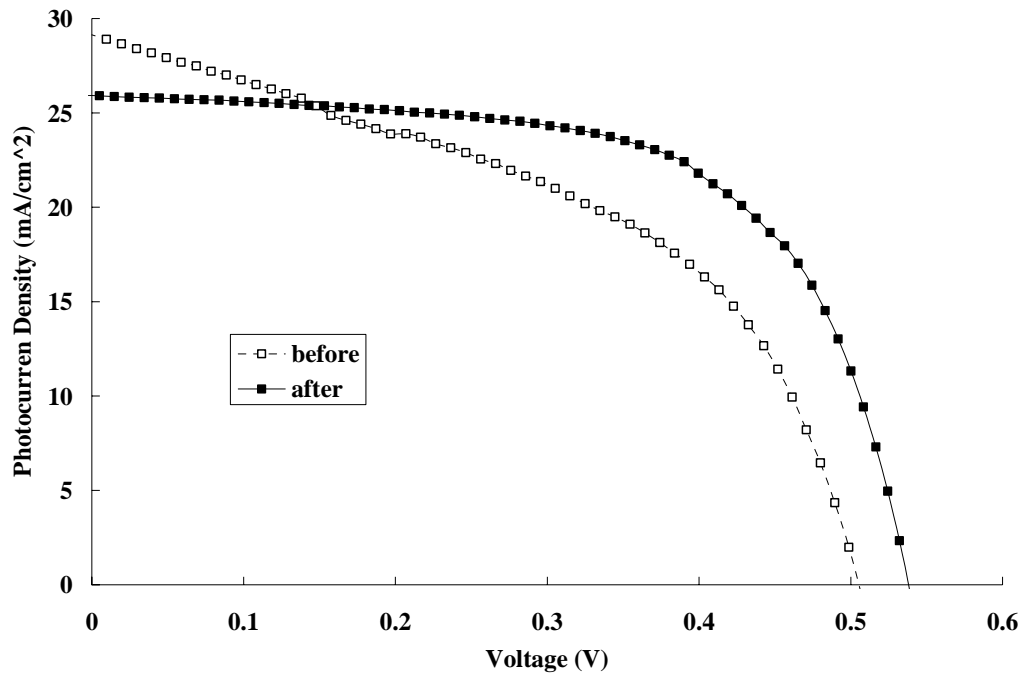


Figure 8-7. Photo- J-V results of CIGS device #1 (cell#2) before and after total dose of 2.12 Mrads (Si) radiation (Device from GSE).

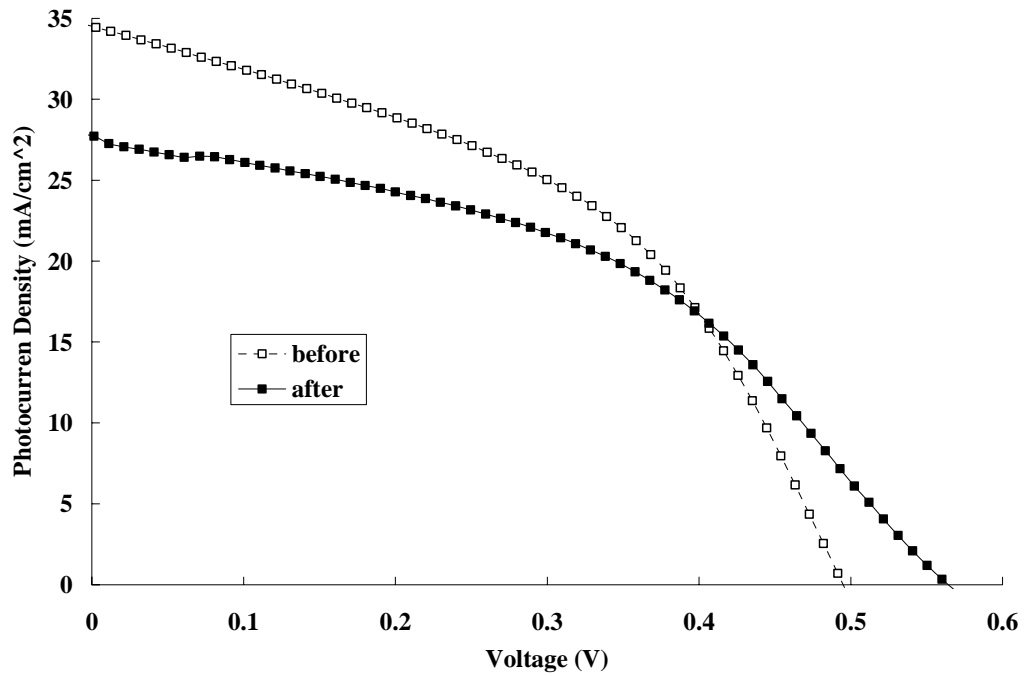


Figure 8-8. Photo- J-V results of CIGS device #2 (cell#1) before and after total dose of 6.5 Mrads (Si) radiation (Device from SSI).

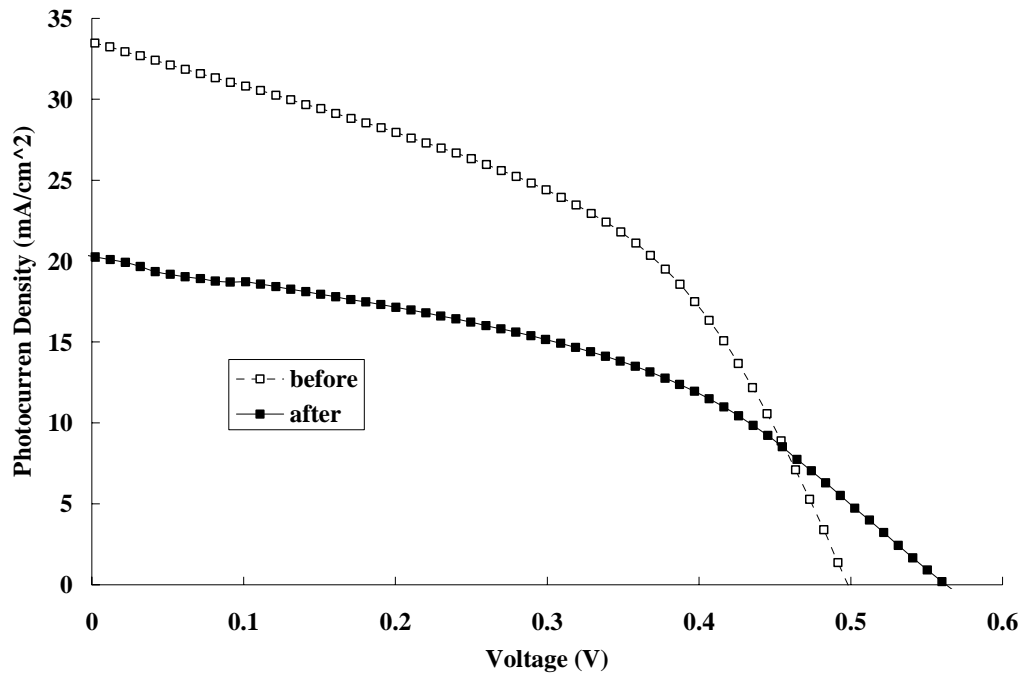


Figure 8-9. Photo- J-V results of CIGS device #2 (cell#2) before and after total dose of 6.5 Mrads (Si) radiation (Device from SSI).

## CHAPTER 9 SUMMARY AND FUTURE WORK

### **Summary**

The effects of Pulsed Laser Annealing (PLA) treatment on the film properties and the performance of CIGS solar cells have been studied under various annealing conditions. This technique has been used to modify near-surface defects and related junction properties in Cu(In,Ga)Se<sub>2</sub> (CIGS) solar cells. CIGS films deposited on Mo/glass substrates were annealed using two different laser systems at selected laser energy densities and pulse number. The narrow of XRD peak, the new shoulders of GIXD and the increase of SEM surface feature size suggest near surface structure changes in the CIGS films. The Dual-Beam Optical Modulation (DBOM) and Hall-effect measurements reveal that PLA treatment increases the effective carrier lifetime and mobility as well as the sheet resistance of the CIGS absorber.

In addition, several annealed CdS/CIGS films processed by PLA were fabricated into solar cells and characterized by photo- and dark- J-V and quantum efficiency (Q-E) measurements. The results show a significant improvement in the overall cell performance, diode quality and spectral response when compared to pre-annealed cells. Deep- level transient spectroscopy (DLTS) results show a reduction of the density of shallow defect trap after low power PLA treatments. The energy density of the laser beam and the pulse number were found to play a key role in modifying the optical and electrical properties of the CIGS films and hence the cell performance. A near optimal PLA condition was obtained in this study.

A comprehensive study of the effect of Rapid Thermal Annealing (RTA) on the film properties and the performance of CIGS solar cells has also been carried out in this work. CIGS samples and devices have been characterized by XRD, GIXD, SEM, Hall-effect, photo- and dark- J-V and Q-E measurements on CIGS samples before and after RTA treatments under various ramp up and down rates, peak temperature, holding time, and different ambient conditions. Device modeling and simulation were performed to study the progressive RTA effect on defect density and other important parameters of CIGS solar cells. The results show that progressive RTA treatment could significantly improve the overall uniformity and performance of large area CIGS solar cells. Under low RTA temperature, the surface composition and morphology remain unchanged. The RTA effect on CIGS devices shows partial improvements of cell's performance and overall increase of quantum efficiency. The estimated optimal annealing temperatures should be between 200 and 300°C with 1- minute or less holding time.

Device simulation using AMPS-1D program has also been carried in this work for a typical CIGS cell with different defect densities. A well fitting between simulation results and progressive RTA results has been obtained. The results show that the device performance and spectral response can be positively improved by reducing the defect density of CIGS absorber layer.

An explorative study of the Gamma-Ray radiation tolerance of CIGS films and solar cells were conducted to investigate the total dose effects with different displacements on the film property and device performance by varying the sample displacements and exposure times. XRD and Photo- J-V results before and after each

radiation show that Gamma-Ray radiation is able to affect the crystallinity of CIGS samples and the device performance under certain dose condition.

### **Future Work**

Based on the promising results from this work, future efforts should focus on PLA study using different types of Excimer laser systems that offer various laser beam sizes, different energy densities and wavelengths with uniform surface energy density, variable pulse widths and scan rates to access a wider range of PLA treatment conditions. In particular, it is suggested that a variable pulse width and wavelength laser can be used to allow the control of anneal depth. Given its application to other industrial materials, laser annealing has the potential to be an effective method to improve solar cell performance in an industrial setting. Comparison of RTA and conventional furnace annealing should also be studied in the near future. A detailed simulation of effects of defect density on CIGS cells performance and the correlation between the simulation data and the experimental PLA and RTA data will be studied. Effects of low dose Gamma-ray radiation on CIGS solar cells, as well as the accurate radiation dose threshold will be investigated in the future radiation tolerance study on CIGS materials.

## LIST OF REFERENCES

1. M. A. Green, K. Emery, D. L. King, S. Igari, and W. Warta, *Progress in Photovoltaics: Research and Applications 2004*, vol. 12, pp. 365-372, 2004.
2. GG. Bentini, M. Bianconi, L. Corraera, R. Nipoti, C. Summonte, C. Cohen, and J. Siejka, *European Materials Research Society Conference Proceedings*, vol. XV, p. 251, 1987.
3. G.K. Giust, T.W. Sigmon, P.G. Carey, B. Weiss, and G.A. Davis, *IEEE Electron Device Letters*, vol. 19, pp. 343-344, 1998
4. G.K. Giust, and T.W. Sigmon, P.G. Carey, B. Weiss, and G.A. Davis, *IEEE Transactions on Electron Devices*, vol. 47, pp. 207-213, 2000
5. GG. Bentini, M. Bianconi, and C. Summonte, *Applied Physics A*, vol. 45(4), pp. 317-324, 1988.
6. X. Zhang, T. Zhang, M. Wong, and Y. Zohar, *Journal of Microelectromechanical Systems*, vol. 7(4), pp. 356-364, 1998
7. S.E. Rosenberg, P.Y. Wong, and I.N. Miaoulis, *IEEE Transactions on Semiconductor Manufacturing*, vol. 9, pp. 249-256, 1996.
8. W. Chen, Z. Li, and H.W. Kraner, *IEEE Transactions on Nuclear Science*, vol. 39, pp. 558-562, 1992.
9. A. Slaoui, F. Foulon, and P. Siffert, *Journal of Applied Physics*, vol. 67, p. 6197, 1990.
10. A. Rohatgi, P. Doshi, S. Kamra. 14th European PVSECE Conference. Proceedings, p. 660, 1997.
11. T. Jackson and M. Oliver, *Energy Policy*, vol. 28, p. 983, 2000.
12. D.A. Johnston, M.H. Carletto, K.T. R. Reddy, I. Forbes and R.W. Miles, *Thin Solid Films*, vol. 403-404, pp. 102-106, 2002
13. M. A. Green, *Energy Policy*, vol. 28, p. 989, 2000.
14. B. A. Andersson and S. Jacobsson, *Energy Policy*, vol. 28, p. 1037, 2000.

15. W. Fuhs and R. Klenk, 2nd World Conference on Photovoltaic Solar Energy Conversion Conference Proceedings, Vienna, Austria, 1998, pp. 381-386.
16. W. H. Bloss, F. Pfisterer, M. Schubert, and T. Walter, Progress in Photovoltaics: Research and Applications, vol. 3, p. 3, 1995.
17. K. Zweibel, International Journal of Solar Energy, vol. 12, p. 285, 1992.
18. J. R. Tuttle, M.A. Contreras, A.M. Gabor, K.R. Ramanathan, A.L. Tennant, D.S. Albin, J. Keane, and R. Noufi, Progress in Photovoltaics: Research and Applications, vol. 3, p. 383, 1995.
19. D. Bonnet and M. Harr, Proceedings of 2nd World Conference on Photovoltaic Solar Energy Conversion, Vienna, Austria, 1998, pp. 397-402.
20. S. Guha, J. Yang, A. Banerjee, K. Hoffman, S. Sugiyama, and J. Call, Proc. IEEE Photovoltaic Specialists Conference, pp. 607-610, 1997.
21. A. Banerjee, X. Xu, J. Yang and S. Guha, Applied Physics Letter, vol. 67, pp. 2975-2977, 1995.
22. J. Yang, X. Xu, A. Banerjee, and S. Guha, Proceedings of IEEE Photovoltaic Specialists Conference, pp. 1041-1044, 1996.
23. J. Yang, A. Banerjee, T. Glatfelter, S. Sugiyama, and S. Guha, Proceedings of IEEE Photovoltaic Specialists Conference, pp. 563- 568, 1997.
24. B. Rech and H. Wagner, Applied Physics. A 69, pp. 155- 167, 1999.
25. D. Bonnet, International Journal of Solar Energy, vol. 12, p. 1, 1992.
26. J. Skarp, Y. Koskinen, S. Lindfors, A. Rautiainen, and T. Suntola, Proceedings of 10th European Photovoltaic Solar Energy Conference, Lisbon, Portugal, pp. 567-569, 1991.
27. R.A. Sasala, X.X. Liu, and J.R. Sites, International Journal of Solar Energy, vol. 12, p. 17, 1992.
28. V.M. Arutyunyan and M.L. Dimaksyan, Applied Solar Energy, vol. 32, p. 1, 1996.
29. A. Rockett and R.W. Birkmire, Journal of Applied Physics, vol. 70, pp. R81-R97, 1991.
30. J.S. Luo, W.T. Lin, C.Y. Chang, and W.C. Tsai, Journal of Applied Physics, vol. 82, p. 3621, 1997.
31. D.R. Chen, J.S. Luo, W.T. Lin, C.Y. Chang, and P.S. Shih, Applied Physics Letters, vol. 73, p. 1355, 1998.

32. X.M. Lu, J.S. Zhu, W.S. Hu, Z.G. Liu, and Y.N. Wang, *Applied Physics Letters*, vol. 66, p. 2481, 1995.
33. S.S. Li, B.J. Stanbery, C.H. Huang, C.H. Chang, Y.S. Chang, and T.J. Anderson, 25th IEEE Photovoltaic Specialists Conference, Washington D.C., U.S.A., May 13-17, 1996, pp. 821-824.
34. C.H. Huang, Sheng S. Li, B.J. Stanbery, C.H. Chang, and T.J. Anderson, 26th IEEE Photovoltaic Specialists Conference, Anaheim, U.S.A., Sep 29-Oct 3, 1997, pp. 407-410.
35. A. Fahrenbruch, R. Bube, Academic Press, New York, 1983.
36. S.M. Sze, Wiley, New York, 1985.
37. T. Yanagisawa, T. Kojima, T. Koyanagi, K. Takahisa, and D. Nakamura, *Electronic Letters*, vol. 36, pp. 1659-1660, 2000.
38. M.K. El-Adawi and I.A. Al-Nuaim, *Vacuum*, vol. 64, pp. 33-36, 2002.
39. D. Willett and S. Kuriyagawa, Proceedings of 23th IEEE Photovoltaic Solar Energy Conference, Louisville, KY, USA, 1993, pp. 495-500.
40. T. Meyer, M. Schmidt, R. Harney, F. Engelhardt, O. Seifert, J. Parisi, M. Schmitt, and U. Rau, Proceedings of 26th IEEE Photovoltaic Solar Energy Conference, Anaheim, CA, USA, 1998, pp. 371-374.
41. A.E. Delahoy, A. Ruppert, and M.A. Contreras, *Thin Solid Films*, vol. 140, pp. 361-362, 2000.
42. M.A. Green, *Solar cells Operating Principles, Technology and System Applications*, University of New South Wales, Kensington, (1992).
43. B.M. Keyes, P. Dippo, W. Metzger, J. Abushama, and R. Noufi, the 29th IEEE Photovoltaic Specialist Conference, New Orleans, LA, 2002
44. A.F. Kohan, G. Ceder, D. Morgan, and C.G. Van de Walle, *Physical Review*, vol. B 16, p. 15019, 2000.
45. A.V. Singh, R.M. Mehra, N. Buthrath, A. Wakahara, and A. Yoshida, *Journal of Applied Physics*, vol. 90, p. 5661, 2001.
46. H. Kim, J.S. Horwitz, W.H. Kim, A.J. Makinen, Z.H. Kafafi, and D.B. Chrisey, *Thin Solid Films*, vol. 420-421 pp. 539-543, 2002.
47. T. Minami, K. Oohashi, and S. Takata, *Thin Solid Films*, vol. 193-194, p. 721, 1990.

48. M. Chen, Z.L. Pei, X. Wang, C. Sun, and L.S. Wen, *Journal of Materials Research*, vol. 16, p. 2118, 2001.
49. Y. Qu, T.A. Gessert, K. Ramanathan, R.G. Dhere, R. Noufi, and T.J. Coutts, *Journal of Vacuum Science and Technology*, vol. A 11, p. 996, 1993.
50. M. Hiramatsu, K. Imaeda, N. Horio, and M. Nawata, *Journal of Vacuum Science and Technology*, vol. A 16, p. 669, 1998.
51. G.A. Hirata, J. McKittrick, T. Cheeks, J.M. Siqueiros, J.A. Diaz, O. Contreras and O.A. Lopez, *Thin Solid Films*, vol. 288, p. 29, 1996.
52. K.T.R. Reddy, T.B.S. Reddy, I. Forbes, and R.W. Miles, *Surface and Coating Technology*, vol. 151, p. 110, 2002.
53. A. Yamada, B. Sang, and M. Konagai, *Applied Surface Science*, vol. 112, p. 216, 1997.
54. K. Tominaga, N. Umezu, I. Mori, T. Ushiro, and I. Nakabayashi, *Journal of Vacuum Science Technology*, vol. A 16, p. 1213, 1997.
55. B.J. Lokhande and M.D. Uplane, *Applied Surface Science*, vol. 167, p. 243, 2000.
56. L.J. Van Der Pauw, *Phillips Technical Review* 20, pg 220.
57. L.J. Van Der Pauw, *Phillips Research Reports* 13, no.1, pg 1.
58. K. Ramanathan, R. Noufi, J. Granata, J. Webb, and J. Kean, *Solar Energy Materials and Solar Cells*, vol. 55, 1998, pp. 15-22.
59. S. S. Li, *Semiconductor Physical Electronics*, Plenum Press, New York, 1993
60. C. Huang, *Alternative Buffer layers, Device Modeling and Characterization of Copper-Indium-Diselenide-Based Thin-Film Solar Cells*, Ph.D. dissertation, University of Florida, Gainesville, FL, 2002.
61. A. Schönecker and K. Bücher, *Conference Record of 22nd IEEE Photovoltaic Specialists Conference*, pp. 203-208 1991.
62. G. Sala, J. Olivan, and J.C. Zamorano, *Proceedings of the 11th E.C. Photovoltaic Solar Energy Conference*, pp. 341-343, 1992.
63. D. V. Lang, *Journal of Applied Physics*, vol. 45(7), pp. 3014, 1974.
64. L.L. Kerr, S.S. Li, T.J. Anderson, and O.D. Crisalle, *National Center for Photovoltaics and Solar Program Review Meeting*, NREL/CD-520-33586 (2003).
65. H. Zhu, A.K. Kalkan, J. Hou, and S.J. Fonash, *American Institute of Physics Conference Proceedings*, no. 462, pp. 309-314, 1999.

66. D. Schmid, D. M. Ruckh, F. Grunwald, and H.W. Schock, *Journal of Applied Physics*, vol. 73, no. 6, pp. 2902-2909, 1992.
67. M.A. Contreras, H. Wiesner, D. Niles, K. Ramanathan, R. Matson, J. Tuttle, J. Keane, and R. Noufi, *Conference Record of the 25th IEEE Photovoltaic Specialists Conference*, pp. 809-812, 1996.
68. P.V. Dressendorfer, 1998 IEEE Nuclear and Space Radiation Effects Conference, Short Course Notes, Ch. III, Newport Beach, CA, USA, 1998.
69. S.T. Pantelides, S.N. Rashkeev, R. Buczko, D.M. Fleetwood and R.D. Schrimpf, *IEEE Transactions on Nuclear Science*, vol 47, pp 2262-2268, 2000.
70. C. Poivey, T. Carriere, J. Beaucour and T.R. Oldham, *IEEE Transactions on Nuclear Science*, vol 41, pp 2235-2239, 1994.
71. J.C. Pickel, *IEEE Transactions on Nuclear Science*, vol 43, pp 912-917, 1996.
72. C. Claeys and E. Simoen, European Space Research and Technology Centre contract report P35284-IM-RP-0013, March 30 2000.
73. C.J. Dale, P.W. Marshall, G.P. Summers and E.A. Wolicki, *Applied Physics Letters*, vol 54, pp 451-453, 1989.
74. J.R. Srour, *IEEE Transactions on Nuclear Science*, vol 47, pp 2451-2459, 2000.
75. S.R. Messenger, E.A. Burke, G.P. Summers, M.A. Xapsos, R.J. Walters, E.M. Jackson and B.D. Weaver, *IEEE Transactions on Nuclear Science*, vol 46, pp 1595-1602, 1999.
76. M.S. Robbins, *IEEE Transactions on Nuclear Science*, vol 47, pp 2473-2479, 2000.

## BIOGRAPHICAL SKETCH

Xuege Wang was born in Beijing, China. He received a Bachelor of Science degree from the department of Electrical Engineering at the Beijing University of Aeronautics and Astronautics, China, in 1999. Since 2000, he has been a research assistant in the Optoelectronics Laboratory at the University of Florida, under Dr. Sheng S. Li's guidance. In December 2002, he was awarded a Master of Science degree in ECE from the University of Florida. After his graduation, he continued to work toward his Ph.D. degree. His research interests include characterization and fabrication of CIGS-based thin-film solar cells for low-cost terrestrial power generation.